Photorefractive properties of ferroelectric materials for optical phase conjugation, two-beam coupling, and holographic storage

Thesis by

Koichi Sayano

In Partial Fulfillment of the Requirements

for the Degree of

Doctor of Philosophy

California Institute of Technology

Pasadena, California

1990

(Submitted May 31, 1990)

Acknowledgements

First of all, I would like to thank my thesis advisor, Prof. Amnon Yariv, for his guidance, many helpful suggestions, and feedback for the past five years. In addition, his Quantum Electronics Group helped foster a general atmosphere of creativity and strong motivation to seek out and understand the physics behind the many interesting problems in this area.

I would also like to acknowledge some others in the group for very productive collaborative efforts: Dr. Aharon (Ronnie) Agranat, for the work in the area of potassium tantalate niobate (KTN) growth, characterization, and optical effects in cubic materials, and also for giving me numerous hints and ideas in regards to experimental work in general; Dr. George Rakuljic, for some of my initial work on strontium barium niobate (SBN); Dr. Norman Sze-Keung Kwong, who first introduced me to phase conjugation and photorefractive nonlinear optics; Dr. Joel Paslaski, whom I had the pleasure of working with during my first summer in graduate school in the area of picosecond optical pulse generation and detection; Dr. Yasuo Tomita, for work in phase conjugation applications, and in particular the one-way image transmission work in Sec. 7.3.2.; and Victor Leyva, whom I worked with in the KTN materials study, and who also grew most of the KTN crystals used in my experimental work. In addition, I would like to recognize the contributions of Dr. Ratnakar Neurgaonkar at Rockwell Science Center whom I worked with in the SBN materials research and who supplied the SBN crystals for this work.

Others in the group and at Caltech also provided considerable help in my thesis research. Desmond Armstrong provided help in constructing instruments

and purchasing equipment and supplies; Ali Ghaffari in maintaining some of the equipment used; Jana Mercado in providing clerical support and helping get the everyday matters done; Vicki Arriola for drawing many of the illustrations for publication, often on very short notice; and Larry Begay for machine shop support and building some of the equipment for my experiments.

Professor Tom Apostol was my first contact with Caltech and encouraged me to apply as an undergraduate for the Class of '85. Profs. Peter Wannier and James Mercerau were my undergraduate advisors and assisted me in applying for graduate school. I had the pleasure of fruitful discussions on a variety of topics (not just limited to optics) with Profs. William Bridges and Kerry Vahala. Dr. Tom McDonough introduced me to the Caltech/JPL Toastmasters which helped me develop my speaking skills during the past three and a half years I have been a member of the club.

I would also like to thank President Thomas Everhart, Vice President for Student Affairs Gary Lorden, Assistant Vice President Jeanne Noda, Dean of Graduate Studies Arden Albee, the Caltech Alumni Association and its staff, and my fellow officers and directors of the Graduate Student Council who helped me throughout the past year I served as GSC Chairman and helped make it a very productive term.

I would like to acknowledge financial support from the U.S. Air Force Weapons Laboratory Graduate Fellowship program, the Defense Advanced Research Projects Agency, U.S. Army Research Office, and the U.S. Air Force Office of Scientific Research.

Finally, I would like to thank my parents and family for their support during my years here at Caltech.

Abstract

The results of a systematic investigation of doped strontium barium niobate and potassium tantalate niobate for photorefractive beam coupling and optical holographic storage are presented in this thesis. Methods that were successfully employed to increase the magnitude of the photorefractive effect and speed up the response of these materials are also presented. Applications in the area of optical phase conjugation, distortion correction, limiting, and thresholding are also discussed.

In the first part, the equations governing the photorefractive effect through band transport are introduced. The solutions giving the internal space charge field in photorefractive materials are presented for the one carrier, one species model that approximates the process in strontium barium niobate and most other materials. The coupled equations describing the two-beam coupling effect are also derived.

Next, the results of experiments using as-grown potassium tantalate niobate for holographic diffraction and strontium barium niobate for two-beam coupling are presented. With KTN, the effect of Nb concentration on the phase transition, temperature dependence of diffraction efficiency and dark storage time, and the effects of the bias electric field are discussed. With SBN, the effect of dopant type, temperature dependence of the photorefractive effect, the effects of dark conductivity in Cr-doped SBN:60, and wavelength dependence are presented.

The third part describes methods and results of increasing the magnitude of the photorefractive effect in SBN. Optimization of the grating period, oxidation and reduction heat treatments, temperature control, and applied fields are

discussed. Significant increases in the two-beam coupling constant were observed in Cr-doped SBN:60 with applied fields of up to 10 kV/cm. An order of magnitude reduction of the response time in Rh-doped SBN:60 has been achieved with an applied field of 10 kV/cm.

The final part discusses applications of these materials, particularly in the areas of phase conjugation, distortion correction, and optical signal processing. A total internal reflection phase conjugate mirror using SBN instead of $BaTiO_3$, a one-way image transmission scheme that can send a signal through a distorting medium, thresholding using a semilinear phase conjugate mirror with grating motion, and a field controlled and enhanced optical limiter are presented.

Table of Contents

CHAPTER ONE

Introduction to Photorefractive Materials and their Applications

1.1. Photorefractive materials for optical information storage

Photorefractive materials have become the medium of choice for a wide range of image processing, optical storage, and phase conjugation applications. In general, the term "photorefractive material" can be taken to mean any material with light-dependent changes in the refractive index, but the current usage of the term is more restrictive in refering specifically to those materials where the index variation is the result of an internal electric field resulting from migration and trapping of photoexcited electrons. These materials have played an important role as the basis for developing new architectures for optical memories, optical computing, image processing, and sensing applications.

The first observation of this phenomenon was by A. Ashkin, et al. in $LiNbO_3$, where the effect was seen to be an adverse condition, or "optical damage," that degraded its usefulness in optical applications because of distortions arising from the index inhomogenieties.[1] Later, this property was shown by F.S. Chen, et al. to have potentially useful applications as the storage medium for volume holograms.[2] The index variations introduced were found to be erasable by heating the crystal to approximately 470 K, so the term "photorefractive," instead of the "optical damage" more characteristic of deleterious effects, was adopted in describing this phenomenon. Other materials that have been found to be photorefractive include $KNbO_3$,[3] $KTa_{1-x}Nb_xO_3$ (KTN),[4] $Bi_{12}SiO_{20}$,[5] $BaTiO_3$,[6] and $Sr_xBa_{1-x}Nb_2O_6$ (SBN:x).[7]

Currently, although various types of photorefractive materials are available, the slow response of many of these materials is the limiting factor for many applications. Therefore, recent work in photorefractive materials has concentrated on improving the properties of these materials, that is, speeding up the response without sacrificing the magnitude of the effect, and in bringing new types of materials into use for applications in the areas of optical information storage, optical information processing, and a new class of image processing devices using the principle of optical phase conjugation. KTN has been of particular interest because of its potential for storage of large amounts of optical information with high diffraction efficiencies, and has recently been successfully grown with suitable optical characteristics and quality for optical information storage.[8] Other photorefractive materials such as ferroelectric $BaTiO_3$[6] and SBN[9] have also been successfully grown with high optical quality and large nonlinear effects. $BaTiO_3$ has been available commercially for the past several years in a variety of geometries cut in various orientations that range from approximately 5 to 10 mm on each side and with optical quality suitable for a variety of optical measurements and applications. SBN has also been available recently on the commercial market from a number of suppliers, although it has already been grown and studied for several years for research purposes.

The requisite goals of photorefractive materials research has been to achieve the maximum possible effect, and also speeding up the response time. To obtain the large photorefractive effects necessary to improve the efficiency of these devices using these materials, large nonlinearities and the maximum possible space-charge fields inside the materials are necessary. In addition, fast response time materials are desirable to enable real-time operation of devices using these materials. Also an important underlying requirement is high optical quality to minimize distortions,

scattering losses, and other unwanted effects. The principal aim of this work has been to develop materials that satisfy these criteria and attempt to provide specific improvements in their optical characteristics such as increasing the coupling constant and reducing response time through a variety of methods for improved devices utilizing these materials.

1.2. Applications using nonlinearities of photorefractive materials

One of the first applications of photorefractive materials has been the use of $LiNbO_3$ as the storage medium in volume holography.[2] The basic photorefractive mechanism responsible for this effect is shown in Fig. 1-1. The light interference pattern that is written in the crystal by the signal and reference beams excites electrons from ionizable donors into the conduction band, where they drift and diffuse and are eventually retrapped, collecting locally in regions of low intensity. In this way, a charge distribution that mimics the original light interference pattern is formed, resulting in a periodic space-charge electric field. This space-charge field interacts through the electro-optic coefficient of the material to form an index variation grating, which holds the holographic information contained in the two writing beams.

In ferroelectric materials undergoing the process just described, the Δn resulting from the linear electro-optic effect operating on the space-charge field is phase shifted by $\pi/2$ from the light interference pattern, resulting in coupling of the two beams interacting in the crystal. This makes possible energy transfer from one of the beams writing the hologram to the other in real time (see Fig. 1-2 for the experimental notation). In ferroelectric materials such as $BaTiO_3$ and SBN with a large first order linear electro-optic effect, large beam coupling effects can be obtained, resulting in significant beam amplification. The figure of merit for

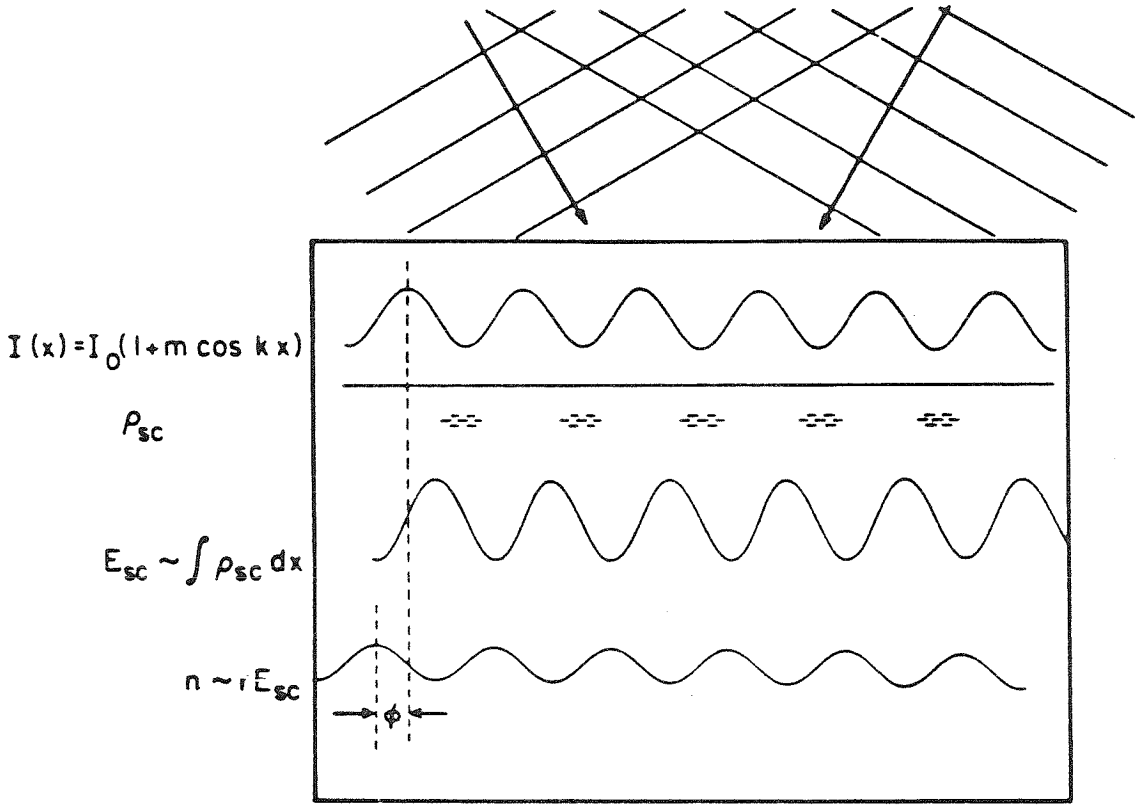

Fig. 1-1: Basic photorefractive mechanism, where the light interference pattern excites electrons from the donor sites to the conduction band where they drift and diffuse until retrapped in regions of low intensity. The electro-optic effect acts on the space charge field to produce the index modulation.

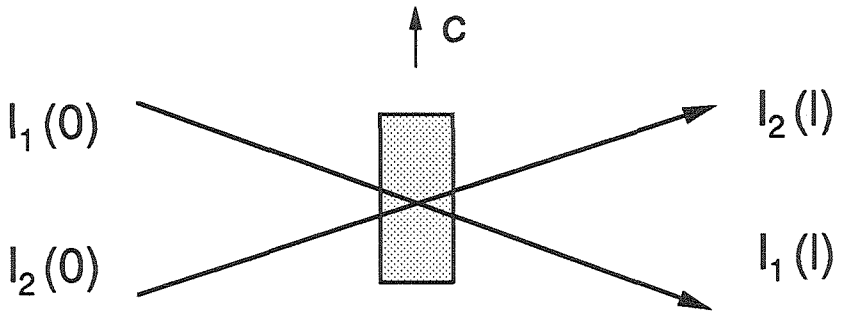

Fig. 1-2: Photorefractive two-beam coupling resulting in beam amplification of I_2 and depletion of energy from I_1.

the degree of energy coupling is described by the two-beam coupling constant, or gain coefficient, which is given by[10]

$$\Gamma = \frac{1}{\ell} \ln \left[\frac{I_{2,i}(\ell)}{I_{1,i}(\ell)} \frac{I_{1,i}(0)}{I_{2,i}(0)} \right], \tag{1.1}$$

where ℓ is the effective length of the interaction region and the subscript i denotes the intensities just inside the surface of the material. Since the ratios of the intensities is what enters into the equation, if the reflection and transmission coefficients of the two beams are assumed to be equal, then the measurements of I_1 and I_2 outside the material can be used.

By choosing the proper orientation of the nonlinear crystal, this property can be used to amplify a weak beam I_2 by feeding energy from a stronger pump beam I_1. In this way, optical amplifiers with gains of more than 4,000 have been constructed using $BaTiO_3$ as the nonlinear medium for two-beam coupling.[11] A variation of this scheme has been used by A.E.T. Chiou and P. Yeh for beam cleanup, where a strong, distorted beam couples its energy into a weaker, clean beam.[12] The result was an amplified beam that retains the undistorted form of the weak probe beam, but contains most of the power of the strong one. Another application of photorefractive two-beam coupling is in using two-beam coupling to couple the energy from different lasers, as demonstrated by J. Feinberg and G.D. Bacher.[13] In addition, other applications taking advantage of the nonzero response time for the two-beam coupling in photorefractive materials to reach a steady state have been shown. One such result is devices like a novelty filter which can detect and isolate parts of a signal image that are time-varying.[14]

For the case of a variable gain coefficient, the two-beam coupling configuration can be made to act as a switch. At the low setting, only a small amount of beam coupling occurs, so there is little amplification of the signal. For very large gain

coefficients, the signal will be amplified by a large factor, and the threshold level can be controlled by various means including partial erasure and control of the photorefractive parameters. A variation of this approach, where the polarization of a $BaTiO_3$ crystal was changed electrically to switch the optical signal, has been successfully demonstrated by R.A. Motes, et al.[15]

The preceding applications all utilized the amplification property of the two-beam coupling effect in photorefractive materials. There is also the converse of these applications, that is, taking advantage of the resulting deamplification of the pump beam. This has a useful application in attenuators for coherent radiation, that is optical limiters.[16] In its most basic configuration, the radiation is simply passed through the crystal, where scattered light acts as the "signal" beam and is amplified by depleting energy from the incident beam, effectively deflecting the energy in the original beam. The phenomenon of beam energy depletion by two-beam coupling amplification of scattered light is called the "fanning" effect because of the broad fan of light deflected from the original beam path. In ordinary beam amplification applications, however, fanning is seen as an undesired effect that robs power from the system.

The real-time beam amplification property of photorefractive materials has also made possible, in addition to the devices already described, new applications in optical modulation,[17] wavefront converters,[18] and photorefractively pumped oscillators and resonators.[19] It has also made possible a new class of phase conjugate mirrors capable of generating phase conjugate waves with incident intensities on the order of milliwatts per cm^2.[20]

1.3. Optical phase conjugation

Optical phase conjugation is the process of wavefront reversal by generating

the spatial complex conjugate of the original wave amplitude.[21] Suppose there is a propagating electric field that can be described by

$$\mathbf{E}(\mathbf{r},t) = \mathbf{A}(\mathbf{r})e^{i(k\cdot r-\omega t)}. \tag{1.2a}$$

Then the phase conjugate of $\mathbf{E}$ is given by

$$\mathbf{E}_{\text{conj}}(\mathbf{r},t) = \mathbf{A}^*(\mathbf{r})e^{-i(k\cdot r+\omega t)}. \tag{1.2b}$$

Note that the phase conjugate represents a wave travelling in the opposite direction from the original wave while retracing its original wavefronts. The difference in behavior between an ordinary mirror and a phase conjugate mirror is shown in Fig. 1-3. The phase conjugate process can also be viewed as time reversal since the reflection exactly retraces the original beam direction.

This property of phase conjugate mirrors enables them to be used in correcting phase distortions. Consider the situation in Fig. 1-4, where the beam passes through a phase distortion. By reflecting the distorted signal back through the distorter with a phase conjugate mirror, the wavefront aberrations of the incident beam retrace themselves, so after passing back through the distorter in the reverse direction, the reflected signal minus the distortion emerges. A similar application has been to construct a laser resonator bounded by a phase conjugate mirror at one end that continues to operate even in the presence of a severe distortion within the cavity because of this property.[22]

Phase conjugation has been achieved through a variety of methods, including stimulated Brillouin and Raman scattering,[23,24] and three- and four-wave mixing.[25] Four-wave mixing has become the method of choice for low power phase conjugation, with photorefractive materials being among the most popular nonlinear media for wave mixing (Fig. 1-5).

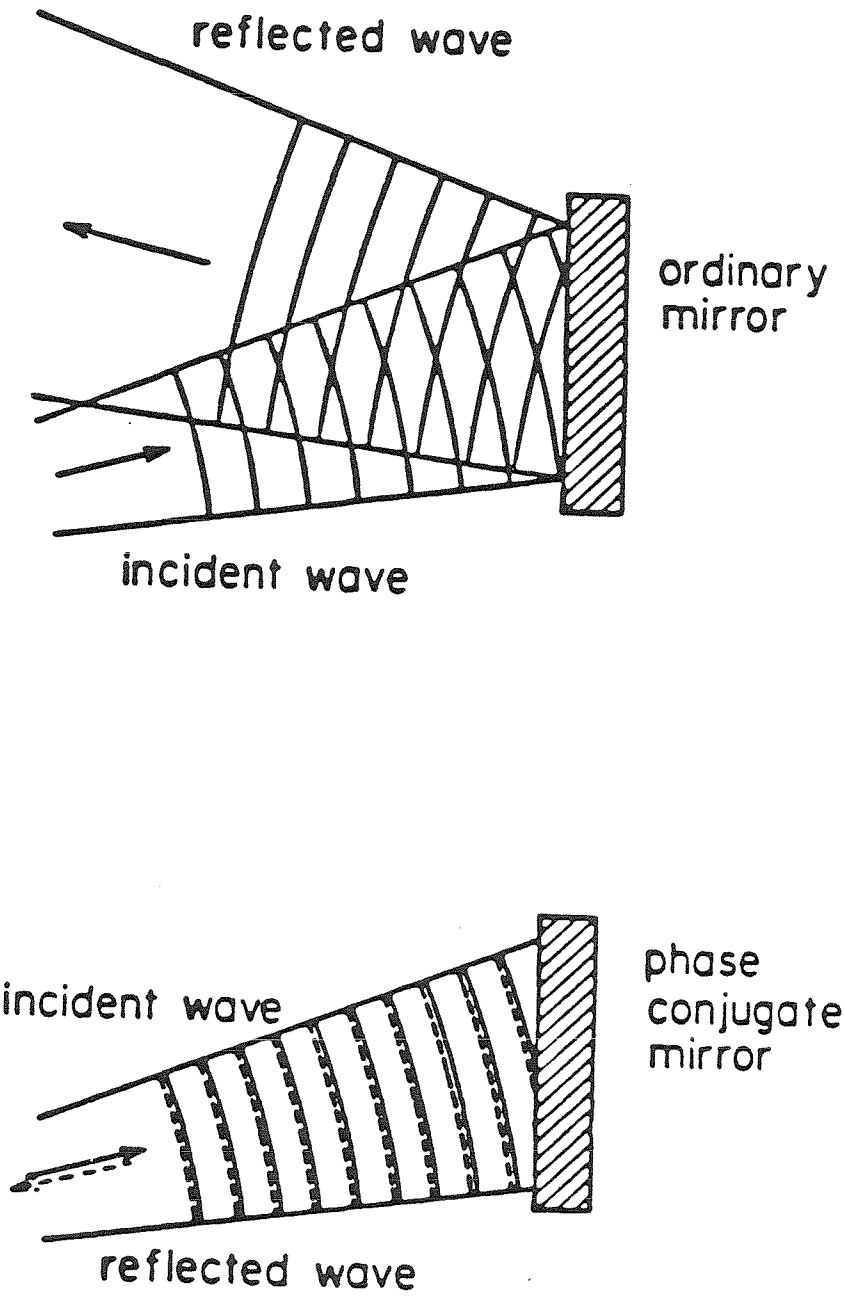

Fig. 1-3: The difference between reflections from a regular mirror (top), where the distorted wavefronts are merely reversed, and a phase conjugate mirror (bottom), where the incident wavefronts are retraced.

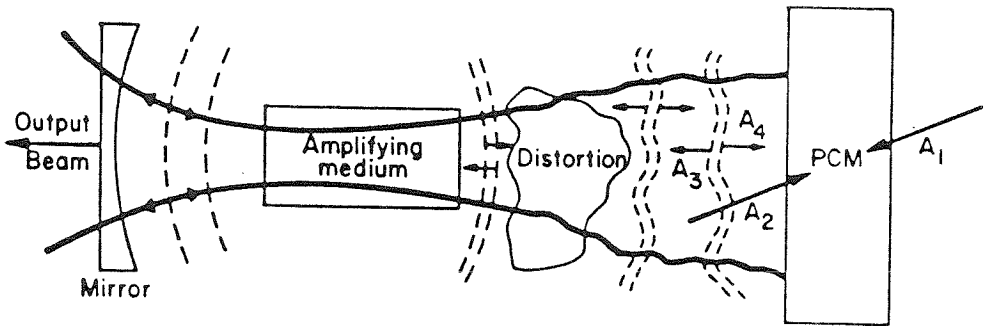

Fig. 1-4: Illustration of the distortion correction property of phase conjugate mirrors, where the phase conjugate reflection back through the distortion is the original undistorted beam.

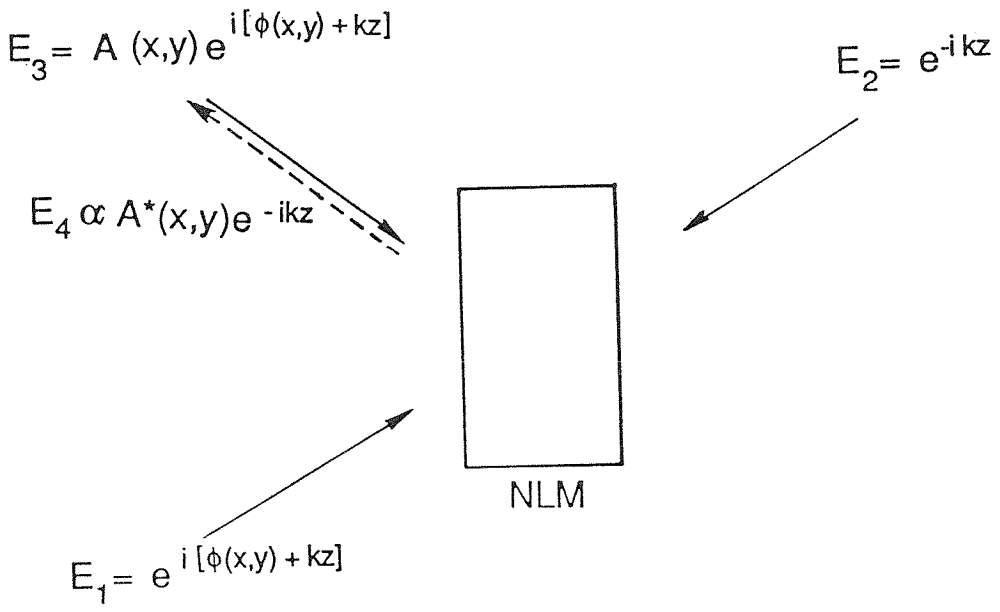

Fig. 1-5: Four-wave mixing configuration of phase conjugation, where waves 1 and 2 are the counterpropagating pump beams, 3 is the incident signal beam, and 4 is the phase conjugate.

From the original four-wave mixing method of phase conjugation, a variety of self-pumped phase conjugate mirrors, which do not require the separate pump beams shown in Fig. 1-5, have been developed. These include the linear and semilinear mirror,[19,26] ring phase conjugate mirror,[27] double phase conjugate mirror,[28] and phase conjugate mirror using internal reflection.[29]

The linear mirror (Fig. 1-6a) uses light deflected from the incident beam through the fanning effect to pump the auxillary cavity, which provides the two pump beams used in the four-wave mixing configuration. The semilinear mirror (Fig. 1-6b) evolved from the linear mirror. Originally, it was discovered that once the linear mirror starts phase conjugating, one of the mirrors could be removed and the mirror would continue operating; later a converging mirror was used to reflect the scattered light back into the crystal to form the grating in a self-starting configuration.

The phase conjugate mirror using internal reflection (Fig. 1-6c) represents an important simplification over the phase conjugate mirrors previously described. Experiments have shown that if the nonlinear gain of the crystal is high enough, the cavity mirrors can be eliminated, with the device relying on the fanning effect from high two-beam coupling gain to generate and maintain the pump beam inside the crystal, and relying on the total internal reflection of the crystal acting as the oscillator cavity. This configuration is completely self-contained, requiring no external parts. It is also self-aligning, accepting a wide range of input angles and simplifying setup of devices utilizing this type of phase conjugate mirror. Experiments have shown that this configuration is also self-starting. The necessary condition is a crystal with sufficient photorefractive gain to be able to spontaneously start generating a phase conjugate output. Because of these advantages, this method is commonly used in experiments requiring phase conjugate mirrors.

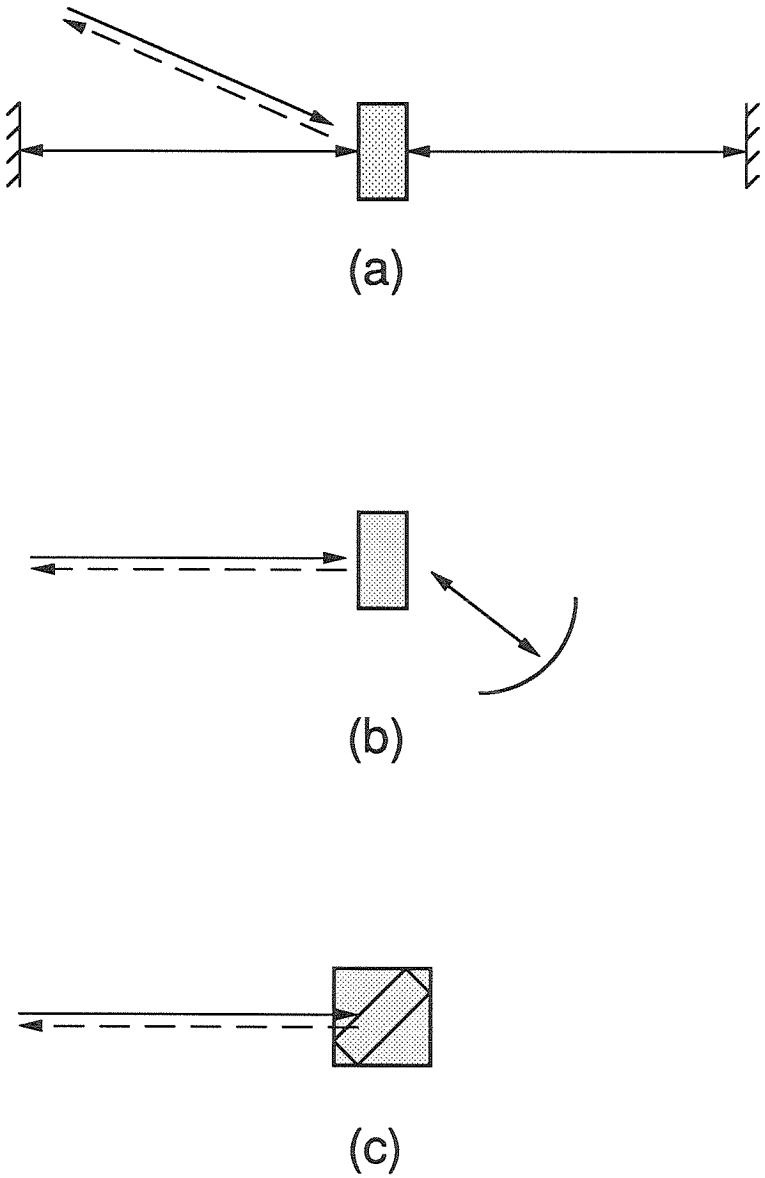

Fig. 1-6: Passive phase conjugate mirrors which do not require external pump beams: (a) Linear mirror, (b) Semilinear mirror, and (c) Total internal reflection phase conjugate mirror.

Phase conjugation has made possible a variety of new devices and applications in optical image processing and optical computing elements. Some examples are: distortion correction, [24] one-way image transmission through a distortion,[30] thresholding of optical signals,[31] optical associative memories,[32] optical convolution and correlation operations,[33] and mathematical operations on images, including real-time image subtraction and differentiation.[34]

1.4. Outline of the thesis

In Chapter 2, the band transport photorefractive model is introduced and discussed, with the solution being given for the one carrier, one species case that describes most photorefractive materials at visible wavelengths. The formation of the index grating through both the linear and quadratic electro-optic effects is also discussed. The beam coupling equations are presented and solved for the two-beam coupling case, with the result being the relation for the coupling constant Γ defined in Eqn. (1.1). Finally, a general discussion on the effects of dark conductivity and external fields on the photorefractive properties just described is presented.

Chapter 3 discusses the preparation and relevant material properties of the materials studied, which include KTN and SBN. The compositions of the various SBN crystals used in the experiments are outlined. The definitions and methods used to measure the figures of merit of diffraction efficiency, gain coefficient, time constant, and photorefractive sensitivity are also introduced.

The photorefractive properties of KTN from the the optical information storage point of view are presented in Chapter 4. Diffraction efficiency and decay time constant measurements were made in Cr and Fe doped KTN samples which were grown with the aim of raising their Curie temperatures to near room temperature. Other samples were first reduced in order to increase the number of available pho-

toionizable donors. Results as a function of temperature and applied bias fields are discussed.

Chapter 5 is a presentation of the optical properties of as-grown SBN:60 and SBN:75. The two-beam coupling constant, steady state index change, photorefractive sensitivity, and response time are presented for SBN:60:Ce, SBN:60:Cr, SBN:60:Rh, and SBN:75:Cr, showing the decreased response time for the case of Cr-doping. The dependence of these parameters on dopant type and concentration, wavelength, and dark conductivity are presented in this chapter. The role of dark conductivity in the temperature dependence of the photorefractive gain in Cr-doped SBN:60 is also discussed.

Chapter 6 describes some methods that attempted to improve the properties of SBN through changes in the experimental conditions, material parameters, temperature, and applied fields. Experimental results showing improvement in gain and response times through these methods, which included optimization of the grating period, oxidation and reduction heat treatment, temperature control, and application of external DC fields are presented.

Finally, applications of photorefractive materials in the areas of distortion correction, phase conjugation, thresholding, and coherent beam attenuation that were developed in the course of this work are presented in Chapter 7. These include self-pumped total internal reflection optical phase conjugation in Ce-doped SBN:75 and SBN:60, one-way image transmission through a distortion using four-wave mixing, thresholding using a semilinear phase conjugate mirror, and electric field-controlled optical limiting.

1.5. References for Chapter 1

1. A. Ashkin, G.D. Boyd, J.M. Dziedzic, R.G. Smith, A.A. Ballman, J.J. Levinstein, and K. Nassau, "Optically induced refractive index inhomogeneities in $LiNbO_3$ and $LiTaO_3$," *Appl. Phys. Lett.* **9**, 72-74 (1966).

2. F.S. Chen, J.T. LaMacchia, and D.B. Fraser, "Holographic storage in lithium niobate," *Appl. Phys. Lett.* **13**, 223-225 (1968); F.S. Chen, "Optically induced change of refractive indices in $LiNbO_3$ and $LiTaO_3$," *J. Appl. Phys.* **40**, 3389-3396 (1969).

3. P. Günter and F. Micheron, "Photorefractive effects and photocurrents in $KNbO_3$:Fe," *Ferroelectrics* **18**, 27-38 (1978).

4. F.S. Chen, "A laser-induced inhomogeneity of refractive indices in KTN," *J. Appl. Phys.* **38**, 3418-3420 (1967); D. von der Linde, A. Glass, and K. Rodgers, "High sensitivity optical recording in KTN by two-photon absorption," *Appl. Phys. Lett.* **26**, 22-24 (1975).

5. J.P. Huignard, J.P. Herriau, G. Rivet, and P. Günter, "Phase conjugation and spatial-frequency dependence of wavefront reflectivity in $Bi_{12}SiO_{20}$ crystals," *Opt. Lett.* **5**, 102-104 (1980); A. Marrakchi, J.P. Huignard, and P. Günter, "Diffraction efficiency and energy transfer in two-wave mixing experiments with $Bi_{12}SiO_{20}$ crystals," *Appl. Phys.* **24**, 131-138 (1981).

6. J. Feinberg, D. Heiman, A.R. Tanguay, and R.W. Hellwarth, "Photorefractive effects and light-induced charge migration in barium titanate," *J. Appl. Phys.* **51**, 1297-1305 (1980).

7. J.B. Thaxter and M. Kestigian, "Unique properties of SBN and their use in a layered optical memory," *Appl. Opt.* **13**, 913-924 (1974).

8. A. Agranat, K. Sayano, and A. Yariv, "Photorefractive diffraction gratings

in KTN:Cr,Fe in the paraelectric phase using the quadratic electro-optic effect," paper PD-1, OSA Topical Meeting on Photorefractive Materials, Effects, and Devices, Los Angeles, CA (1987).

9. R.R. Neurgaonkar, W.K. Cory, J.R. Oliver, M.D. Ewbank, and W.F. Hall, "Development and modification of photorefractive properties in the tungsten bronze family crystals," *Opt. Eng.* **26**, 392-405 (1987).

10. G.A. Rakuljic, A. Yariv, and R.R. Neurgaonkar, "Photorefractive properties of undoped, Ce-doped, and Fe-doped single crystal $Sr_{0.6}Ba_{0.4}Nb_2O_6$," *Opt. Eng.* **25**, 1212-1216 (1986).

11. F. Laeri, T. Tschudi, and J. Albers, "Coherent cw image amplifier and oscillator using two-wave interaction in a $BaTiO_3$ crystal," *Opt. Commun.* **47**, 387-390 (1983).

12. A.E.T. Chiou and P. Yeh, "Beam cleanup using photorefractive two-wave mixing," *Opt. Lett.* **10**, 621-623 (1985).

13. J. Feinberg and G.D. Bacher, "Phase-locking lasers with phase conjugation," *Appl. Phys. Lett.* **48**, 570-572 (1986).

14. S.K. Kwong, Y. Tomita, and A. Yariv, "Optical tracking filter using transient energy coupling effect," *J. Opt. Soc. Am. B* **5**, 1788-1791 (1988).

15. R.A. Motes, R.W. Gallegos, J.J. Kim, and G.A. Brost, "Photorefractive optical switch," paper 1220-20, SPIE OE-LASE Conference on Nonlinear Optics, Los Angeles, to be published in *Proc. SPIE* **1220** (1990).

16. M. Cronin-Golomb and A. Yariv, "Optical limiters using photorefractive nonlinearities," *J. Appl. Phys.* **57**, 4906-4910 (1985).

17. D. Rak, I. Ledoux, and J.P. Huignard, "Two-wave mixing and energy transfer in $BaTiO_3$ application to laser beamsteering," *Opt. Commun.* **49**, 302-306 (1984).

18. S.K. Kwong and A. Yariv, "One-way, real-time wavefront converters," *Appl. Phys. Lett.* **48**, 564-566 (1986).

19. J.O. White, M. Cronin-Golomb, B. Fischer, and A. Yariv, "Coherent oscillation by self-induced gratings in the photorefractive crystal $BaTiO_3$," *Appl. Phys. Lett.* **40**, 450-452 (1982); S.K. Kwong, M. Cronin-Golomb, and A. Yariv, "Oscillation with photorefractive gain," *IEEE J. Quantum Electron.* **QE-22**, 1508-1523 (1986).

20. A. Yariv and D.M. Pepper, "Amplified reflection, phase conjugation, and oscillation in degenerate four-wave mixing," *Opt. Lett.* **1**, 16-18 (1977).

21. B.Ya. Zel'dovich, N.F. Pilipetsky, and V.V. Shkunov, *Principles of Phase Conjugation*, (New York: Springer-Verlag, 1985).

22. M. Cronin-Golomb, B. Fischer, J. Nilsen, J.O. White, and A. Yariv, "Laser with dynamic holographic intracavity distortion correction capability," *Appl. Phys. Lett.* **41**, 219-220 (1982).

23. B.Ya. Zel'dovich, V.I. Popovichev, V.V. Ragul'skii, and F.S. Fasisullov, "Connection between the wave fronts of the reflected and exciting light in stimulated Mandel'shtam-Brillouin scattering," *Sov. Phys. JETP Lett.* **15**, 109-113 (1972).

24. V. Wang and C.R. Giuliano, "Correction of phase aberrations via stimulated Brillouin scattering," *Opt. Lett.* **2**, 4-6 (1978).

25. A. Yariv, *Appl. Phys. Lett.* **28**, 88 (1976); A. Yariv, "Compensation for atmospheric degradation of optical beam transmission by nonlinear optical mixing," *Opt. Commun.* **21**, 49-50 (1977).

26. M. Cronin-Golomb, B. Fischer, J.O. White, and A. Yariv, "Passive (self-pumped) phase conjugate mirror: Theoretical and experimental investigation," *Appl. Phys. Lett.* **41**, 689-691 (1982).

27. M. Cronin-Golomb, B. Fischer, J.O. White, and A. Yariv, "Passive phase conjugate mirror based on self-induced oscillation in an optical ring cavity," *Appl. Phys. Lett.* **42**, 919-921 (1982).

28. S. Weiss, S. Sternklar, and B. Fischer, "Double phase-conjugate mirror: analysis, demonstration, and applications," *Opt. Lett.* **12**, 114-116 (1987).

29. J. Feinberg, "Self-pumped, continuous-wave phase conjugator using internal reflection," *Opt. Lett.* **7**, 486-488 (1982).

30. K. Sayano, Y. Tomita, and A. Yariv, "One-way image transmission through distorting media using orthogonally polarized beams and phase conjugation," unpublished.

31. K. Sayano, G.A. Rakuljic, and A. Yariv, "Thresholding semilinear phase-conjugate mirror," *Opt. Lett.* **13**, 143-145 (1988).

32. A. Yariv, S.K. Kwong, and K. Kyuma, "Demonstration of an all-optical associative holographic memory," *Appl. Phys. Lett.* **48**, 1114-1116 (1986).

33. J.O. White and A. Yariv, "Real-time image processing via four-wave mixing in a photorefractive medium," *Appl. Phys. Lett.* **37**, 5-7 (1980).

34. S.K. Kwong, G.A. Rakuljic, and A. Yariv, "Real-time image subtraction and 'exclusive or' operation using a self-pumped phase conjugate mirror," *Appl. Phys. Lett.* **48**, 201-203 (1986); S.K. Kwong, G.A. Rakuljic, V. Leyva, and A. Yariv, "Real-time image processing using a self-pumped phase conjugate mirror," *Proc. SPIE* **613**, 36-42 (1986).

CHAPTER TWO

Photorefractive Effect in Nonlinear Crystals

2.1. Introduction

The basic function of a photorefractive crystal in phase conjugation, image processing, and related applications is to record dynamic, i.e., real time, holographic gratings. The basic geometry of the typical configuration is shown in Fig. 2-1, where two beams, I_1 and I_2, propagating at angles θ_1 and θ_2 from the normal of the crystal surface, interact in the crystal and form the light interference pattern to be recorded. This information is then stored in the crystal as a phase grating hologram, which also builds up in real time.

The generally accepted and most comprehensive model for the processes occurring in photorefractive materials illuminated by an intensity interference pattern was developed in the band transport model by N.V. Kukhtarev, et al.[1–3] Another model, the "hopping model," was recently proposed by J. Feinberg, et al.[4] The basic principle of both is that charge carriers, either electrons or holes or both, are separated from their donor sites, and their spatial dependence follows that of the spatial light intensity. In the band transport model, this is accomplished by charge motion of the photoexcited carriers in the conduction band through drift and diffusion; the hopping model, on the other hand, describes the charges as hopping from one trapping center to another with some statistical probability proportional to the local intensity. In either case, the separated charge carriers then set up a periodic space-charge electric field, which in turn forms an index variation through the electro-optic effect of the crystal that records the information contained in the interference pattern.

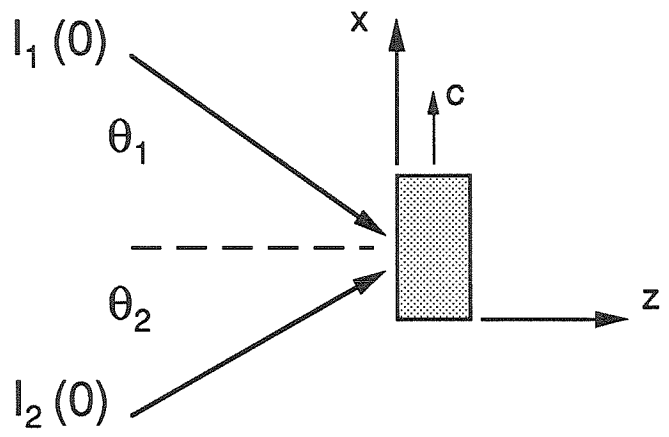

Fig. 2-1: Experimental geometry for wave mixing in photorefractive crystals, where waves 1 and 2 have incidence angles from the normal of θ_1 and θ_2, respectively.

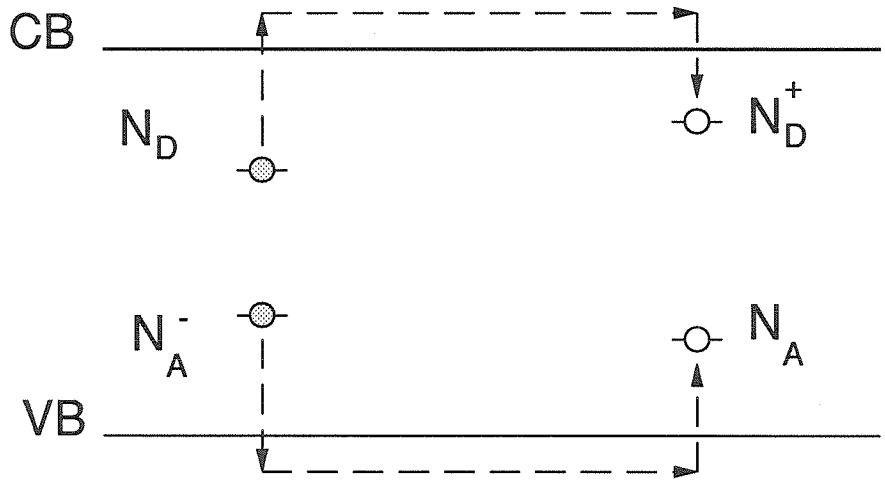

Fig. 2-2: Band transport process, where electrons are photoexcited from donor sites D into the conduction band, where they drift and diffuse until retrapped in sites D^+. A similar process may be present for holes as well.

2.2 Formation of the space-charge field, band transport model

The space charge field is one of the main quantities responsible for the magnitude of the photorefractive effect in these materials. Intuitively, this can be seen since the larger the space charge field from a larger number of separated charges, the larger the resulting index variation from the electro-optic effect under otherwise identical conditions. Various models have been proposed to describe the process, but the band transport model of Kukhtarev has been the most widely used. The solution for the one carrier, one species case gives a fairly good approximation to the photorefractive process in most cases, e.g., SBN illuminated by visible or longer wavelength radiation.

2.2.1 Transport equations

Fig. 2-2 illustrates the band transport process in photorefractive materials, where the crystal contains photoexcitable donors D which release electrons into the conduction band, where they drift and diffuse until they are retrapped by D^+. This process continues until the electrons tend to collect in regions of low intensity, since the trapped electrons are subject to repeated photoexcitation and transport in the conduction band. If hole transport is significant in the material under consideration, then a similar process occurs with holes from A being excited into the valence band and being retrapped by N_A^-.

In the band transport model, which has been widely used to describe the processes occuring in photorefractive materials, the electron and hole transport processes are assumed to be independent of each other. This will be the case if the two species are themselves dominated by either hole or electron transport, but not both. Electrons are excited from the donors into the conduction band at a rate $(\beta_e + \frac{s_e I}{\hbar\omega})(N_D - N_D^+)$ and recombine at a rate $\gamma_e n N_D^+$, with a similar

process for holes being excited into the valence band at $(\beta_h + \frac{s_h I}{\hbar\omega})(N_A - N_A^-)$ and recombining at $\gamma_h p N_A^-$. This process is described by the following equations in MKS units:[2]

The continuity equation,

$$\frac{\partial}{\partial t}(n - N_D^+ + p - N_A^-) - \frac{1}{e}\nabla \cdot \mathbf{J} = 0 \ , \tag{2.1a}$$

the rate equations,

$$\begin{aligned} \frac{\partial N_D^+}{\partial t} &= \left(\beta_e + \frac{s_e I}{\hbar\omega}\right)(N_D - N_D^+) - \gamma_e n N_D^+ \\ \frac{\partial N_A^-}{\partial t} &= \left(\beta_h + \frac{s_h I}{\hbar\omega}\right)(N_A - N_A^-) - \gamma_h p N_A^- \ , \end{aligned} \tag{2.1b}$$

the current equation,

$$\mathbf{J} = e(\mu_e n + \mu_h p)\mathbf{E} + k_B T(\mu_e \nabla n - \mu_h \nabla p) \ , \tag{2.1c}$$

Poisson's equation,

$$\nabla \cdot \mathbf{E} = -\frac{e}{\epsilon}(n + N_{A,C}^- + N_A^- - p - N_{D,C}^+ - N_D^+) \ , \tag{2.1d}$$

and the charge conservation equation,

$$n_0 + N_{A,C}^- - N_{D0}^+ = p_0 + N_{D,C}^+ - N_{A0}^+ \ . \tag{2.1e}$$

In the preceding equations, the definitions of the various parameters and quantities used are given by:

$\mathbf{J}$ = Current density

$\mathbf{E}$ = Space charge electric field

N_D = Number density of electron donors

N_D^+ = Number density of electron traps

N_{D0}^+ = Number density of ionized donors under uniform illumination

N_A = Number density of hole acceptors

N_A^- = Number density of hole donors

N_{A0}^- = Number density of ionized hole donors under uniform illumination

$N_{A,C}^-$= Number density of non-photoactive, compensatory acceptors corresponding to N_D^+

$N_{D,C}^+$= Number density of non-photoactive, compensatory donors corresponding to N_A^-

n = Number density of electrons

p = Number density of holes

γ_e = Electron two-body recombination rate

γ_h = Hole two-body recombination rate

s_e = Photoionization cross section for electrons

s_h = Photoionization cross section for holes

β_e = Thermal excitation rate of electrons

β_h = Thermal excitation rate of holes

ϵ = Dielectric constant

k_B = Boltzmann's constant

T = Temperature

$\hbar\omega$ = Photonic energy of the incident light

e = Magnitude of the electron charge.

The intensity interference pattern from the two beams writing the grating in the material is given by

$$I(x) = I_0\left(1 + m\exp[i(Kx - \omega t)] + c.c.\right), \tag{2.2}$$

where m is the modulation index and $K = 2\pi/\lambda_g$ is the wavenumber of the grating period. For a small modulation index, i.e., $m \ll 1$, the spatial dependence of n, p, N_D^+, N_A^-, E, and I on Kx can be approximated by the linearized Fourier expansion. For large modulation depth, higher order terms in the expansion would become significant.[5]

2.2.2 Solution for one species, one carrier case

The simplest case of the band transport equations is where there is only one type of donor and one type of charge carrier, namely electrons. Studies have shown that most materials, including SBN, can be approximated by this case. For this situation, we set all the parameters corresponding to holes equal to zero, so that $N_A = N_A^- = N_{A0}^- = N_{D,C}^+ = p = \gamma_h = s_h = \beta_h = 0$, and the set of equations reduces to:

$$\frac{\partial}{\partial t}(n - N_D^+) - \mu_e\left(n\nabla\cdot\mathbf{E} + \mathbf{E}\cdot\nabla n + \frac{k_B T}{e}\nabla^2 n\right) = 0 \tag{2.3a}$$

$$\frac{\partial N_D^+}{\partial t} = \left(\beta_e + \frac{s_e I}{\hbar\omega}\right)(N_D - N_D^+) - \gamma_e n N_D^+ \tag{2.3b}$$

$$\nabla\cdot\mathbf{E} + \frac{e}{\epsilon}(n + N_{A,C}^- - N_D^+) = 0\,. \tag{2.3c}$$

For the case where the grating wavevector in Fig. 2-1 is along the x-axis of the coordinate system (which will be satisfied in the symmetric case where $\theta_1 = \theta_2$), and where the modulation index $m \ll 1$, the Fourier expansion of N_D^+, n, and $\mathbf{E}$, where the first order expansion will be used as the trial solutions in Eqns. (2.3a) - (2.3c) are given by

$$N_D^+ = N_{D0}^+ + \frac{1}{2}\sum_{r=1}^{\infty} N_{D,r}^+ e^{irKx} \approx N_{D0}^+ + \frac{1}{2}N_{D1}^+ e^{iKx} + c.c. \tag{2.4a}$$

$$n = n_0 + \frac{1}{2}\sum_{r=1}^{\infty} n_r e^{irKx} \approx n_0 + \frac{1}{2}n_1 e^{iKx} + c.c. \tag{2.4b}$$

$$E = E_0 + \frac{1}{2}\sum_{r=1}^{\infty} E_r e^{irKx} \approx E_0 + \frac{1}{2}E_1 e^{iKx} + c.c. \tag{2.4c}$$

where the Fourier coefficients $F_{-r} = F_r^*$ and F_0 is the constant zeroth order term in the expansion.

Substituting Eqns. (2.4a) - (2.4c) into Eqns. (2.3a) - (2.3c), the result is a second order, ordinary differential equation in E_1, the linear term in the expansion

of the space charge field:

$$\frac{d^2E_1}{dt^2} + 2a\frac{dE_1}{dt} + bE_1 = F \ , \tag{2.5}$$

where

$$a = \frac{1}{2}\left[\beta_e + \frac{sI_0}{\hbar\omega} + \frac{e\mu n_0}{\epsilon} + \gamma_e\left(N_{D0}^+ + n_0\right) - i\mu K\left(E_0 + i\frac{k_BTK}{e}\right)\right] \tag{2.6a}$$

$$b = \frac{e\mu n_0}{\epsilon}\left[\beta_e + \frac{sI_0}{\hbar\omega} + \gamma_e\left(N_{D0}^+ + n_0\right)\right] - i\mu K\left(\beta_e + \frac{s_eI_0}{\hbar\omega} + \gamma_e n_0\right)\left(E_0 + i\frac{k_BTK}{e}\right) \tag{2.6b}$$

$$F = -\frac{m}{1 + \beta_e\frac{\hbar\omega}{sI_0}}\frac{e\mu n_0}{\epsilon}\gamma_e N_{D0}^+\left(E_0 + i\frac{k_BTK}{e}\right) \ . \tag{2.6c}$$

The solution for this equation is well-known, being given by

$$E_1 = ce^{-(a-\sqrt{a^2-b})t} - \left(c + \frac{F}{b}\right)e^{-(a+\sqrt{a^2-b})t} + \frac{F}{b} \tag{2.7}$$

where c is a constant, a, b, and F are as defined in Eqns. (2.6a) - (2.6c), and the boundary condition $E_1(0) = 0$ is imposed. Note that the steady-state solution for E_1 is given by F/b.

In most materials, it can be assumed that the recombination time $1/(\gamma_e N_D^+)$ is much faster than the time constant for space charge grating formation. If this were to be the case, $\frac{d^2E_1}{dt^2} \ll 2a\frac{dE_1}{dt}$, and Eqn. (2.5) can be simplified to the first order equation,

$$\frac{dE_1}{dt} + \frac{b}{2a}E_1 = \frac{F}{2a} \ . \tag{2.8}$$

In addition, for most materials, we can take advantage of the following inequalities in Eqns. (2.6a) - (2.6c):[6]

$$\gamma_e N_{D0}^+ \gg \beta_e + \frac{s_eI_0}{\hbar\omega} \tag{2.9a}$$

$$N_{D0}^+ \gg n_0 \tag{2.9b}$$

Also, since $n_0 + N^-_{A,C} - N^+_{D0} = 0$ from Eqn. (2.3c), the donor density N^+_{D0} can be approximated by

$$N^+_{D0} \approx N^-_{A,C} \,. \tag{2.9c}$$

By using the approximations in Eqns. (2.9a) - (2.9c), and the equation for the zeroth order Fourier component from Eqn. (2.3b) that

$$n_0 = \left(\beta_e + \frac{s_e I_0}{\hbar\omega}\right)\left(\frac{N_D - N^+_{D0}}{\gamma_e N^+_{D0}}\right), \tag{2.10}$$

the steady state solution for E_1 is given by

$$E_{1,ss} = \left[\frac{imE_N}{1 + \beta_e\hbar\omega/(s_e I_0)}\right]\frac{E_0 + iE_d}{E_0 + i(E_N + E_d)} \,. \tag{2.11}$$

In Eqn. (2.11), the diffusion field E_d and the maximum space charge field E_N are given by

$$\begin{aligned} E_d &= \frac{k_B T K}{e} \quad \text{and} \\ E_N &= \frac{eN^-_{A,C}}{\epsilon K}\left(1 - \frac{N^-_{A,C}}{N_D}\right). \end{aligned} \tag{2.12}$$

It is also interesting to note that an order of magnitude calculation of E_N can be made by considering a charge density of $N^-_{A,C}$ separated in an infinite area capacitor with spacing λ_g and dielectric constant ϵ. The resulting field across the plates is within a factor of 2π of $E_N \approx eN^+_0/(\epsilon K)$, which is expected since the capacitor represents the extreme case of the space charge distribution having a periodic delta function distribution in the crystal, that is, with all the mobile charges from the volume bounded by the intensity peaks being concentrated at the boundary surfaces located at the peaks.

To obtain the time-dependent solution for E_1, Eqn. (2.8) can be solved for the transient solution, whose result is

$$E_1 = E_{1,\mathrm{ss}}\left(1 - e^{-t/\tau}\right), \tag{2.13}$$

where

$$\tau = t_0 \left[\frac{E_0 + i(E_\mu + E_d)}{E_0 + (E_N + E_d)} \right], \tag{2.14}$$

for the boundary conditions $E_1(t \to \infty) = E_{1,\mathrm{ss}}$ and $E_1(0) = 0$, which correspond to the grating buildup case. For grating erasure, the boundary conditions become $E_1(0) = E_{1,\mathrm{ss}}$ and $E_1(t \to \infty) = 0$, so the time-dependent solution for E_1 will be given by

$$E_1(t) = E_{1,ss} e^{-t/\tau} . \tag{2.15}$$

In Eqn. (2.14), the characteristic time t_0 and drift field E_μ that determine the response time τ are defined as

$$t_0 = \frac{\hbar\omega N_{A,C}^-}{s_e I_0 \left(1 + \beta\hbar\omega/(s_e I_0)\right) N_D} \tag{2.16a}$$

$$E_\mu = \frac{\gamma_e N_{A,C}^-}{\mu_e K} , \tag{2.16b}$$

where t_0 is the fundamental limit of the time required to separate $N_{A,C}^-$ charges per volume based on the energy per unit time per unit volume deposited in the crystal from the writing beams.[7]

2.3 Formation of the index grating

Certain materials with non-centrosymmetric crystal structures may exhibit birefringence as a function of a space charge electric field through the linear and quadratic electro-optic effects.[8] The linear electro-optic effect, where $\Delta n \propto E$, has been found to be dominant in a variety of ferroelectric materials, including $BaTiO_3$, $Sr_xBa_{1-x}Nb_2O_6$ (SBN), and $Ba_{2-x}Sr_xK_{1-y}Na_yNb_5O_{15}$ (BSKNN),[9] while the quadratic electro-optic effect, where $\Delta n \propto E_j E_k$, has been found to be the leading order term in paraelectric $KTa_{1-x}Nb_xO_3$, where the linear electro-optic effect is small.[10]

2.3.1 Linear electro-optic effect

In general, the electro-optic effect arises from changes in the optical impermeability tensor η_{ij} as a result of an electric field:[11]

$$\Delta\eta_{ij} \equiv \eta_{ij}(\mathbf{E}) - \eta_{ij}(0) = \sum_{j,k} r_{ijk}E_k + \sum_{j,k,l} s_{ijkl}E_kE_l \,, \tag{2.17}$$

where $\eta_{ij}(\mathbf{E}) = \epsilon_0(\epsilon^{-1})_{ij}$. Because of permutation symmetries, the standard contracted indices of electro-optics can be used to simplify the notation. For tetragonal, 4mm symmetry crystals, such as $BaTiO_3$, SBN, and BSKNN, the linear term is dominant; cubic materials have the quadratic term as the leading term in Eqn. (2.17).

In the scalar representation, the susceptibility relates to the photorefractive index modulation n_1, which is half the peak to peak variation of the refractive index, by the relation

$$\begin{aligned} n_1 &= -\frac{2\pi}{n_0}\Delta\chi \\ &\approx \frac{n_0^3}{2} r_{\text{eff}} E_{\text{sc}} \,. \end{aligned} \tag{2.19}$$

In Eqn. (2.19), n_0 is the effective index of refraction of the bulk crystal, which is approximately n_e for small beam intersect angles. Since in a tetragonal symmetry crystal, the electro-optic tensor elements are zero except for r_{13}, r_{51}, $r_{23} = r_{13}$, and $r_{42} = r_{51}$, the effective electro-optic constant in Eqn. (2.19) for the case where the grating wavevector is aligned in the direction of the c axis of the crystal is given by[12]

$$r_{\text{eff}} = r_{33}\cos^2\theta_i - r_{13}\sin^2\theta_i + \left(\frac{n_e - n_o}{n_e}\right)(r_{33} + r_{13})\sin^2 2\theta_i \tag{2.20}$$

where θ_i is the half angle of intersection of the beams inside the crystal. Note that the approximations $n_e \approx n_o \approx n_0$, θ_i small, and $r_{33} \gg r_{13}$ have been used in Eqn. (2.19).

2.3.2 Quadratic electro-optic effect

In the case of symmetric crystals such as paraelectric $KTa_{1-x}Nb_xO_3$, there is no destabilization of the polar vector, so the linear electro-optic effect will be zero. In cases such as these, the index variation Δn will be the result of the next higher order, quadratic (or Kerr) electro-optic effect which is present in all materials without regards to its symmetry. Other materials that exhibit this effect include $BaTiO_3$ in the cubic phase when heated above its ferroelectric phase transition temperature.

For the quadratic electro-optic effect, the birefringence is proportional to the polarization squared, being given by[13]

$$\Delta n = \frac{1}{2} n_0^3 g P^2 \,, \tag{2.21}$$

where $P = \epsilon_0(\epsilon_r - 1)E$, Δn is the index variation from n_0 due to the polarization, and g is the electro-optic coefficient. In the presence of a spatially varying space charge field E_{sc} and a dc bias field E_0, the spatial variation of the refractive index $n_1 = n(x)$ - n_0 will be given by[14]

$$\begin{aligned} n_1 =& \Delta n(E_{sc} + E_0) - \Delta n(E_0) \\ =& \frac{1}{2} n_0^3 g \epsilon_0^2 (\epsilon_r - 1)^2 (2E_0 E_{sc} + E_{sc}^2) \,. \end{aligned} \tag{2.22}$$

Dropping the higher order grating represented by E_{sc}^2, which is insignificant for thick volume holograms, gives

$$n_1 = n_0^3 g \epsilon_0^2 (\epsilon - 1)^2 E_{sc} E_0 \,. \tag{2.23}$$

Note that the index modulation will be present only with an applied field, and that it is also linearly dependent on the external field for the case of volume holograms where the higher order term can be neglected. This also makes possible amplitude

modulation of the diffracted signal with a time-varying external bias field E_0, which has been demonstrated at frequencies of up to 1 KHz in KTN.[10,15] In addition, the dependence of the index variation on ϵ^2, where ϵ typically is on the order of 10^3 to 10^4 in KTN, indicates a potentially large effect. In particular, if the crystal temperature is cooled down to near its Curie temperature T_C, the discontinuity in the dielectric constant at the phase boundary will result in a large value for ϵ and consequently a large photorefractive effect.

2.4 Two-beam coupling in photorefractive crystals

As mentioned in Chapter 1, wave mixing in photorefractive crystals results in two-beam coupling, or transfer of energy from one beam to the other, when the nonlinear medium exhibits a phase shift between the light interference pattern and the index modulation. This is an important basis for phase conjugate mirrors, beam cleanup, and optical signal processing applications. Ferroelectric materials such as $BaTiO_3$, SBN, and BSKNN have been used as the wave mixing medium for such applications. Therefore, these types of materials are often characterized by the magnitude of the two-beam coupling constant, which indicates the exponential gain in the amplified signal beam. KTN crystals which have been poled and cooled to below their ferroelectric phase transition temperatures have also exhibited two-beam coupling, although the measured two-beam coupling constant was considerably less than that of $BaTiO_3$ or SBN.

2.4.1 Coupled wave equations

The coupled wave equations describing the process in the configuration of Fig. 2-1, with the coordinate system oriented as shown in the figure, are derived from the scalar wave equation

$$\nabla^2 \mathbf{E} + k^2 \mathbf{E} = 0, \tag{2.24}$$

where the total electric field is given by

$$\mathbf{E} = \mathbf{A}_1 e^{i(k_1 x - \omega_1 t)} + \mathbf{A}_2 e^{i(k_2 x - \omega_2 t)} + c.c. \tag{2.25}$$

In general, the grating motion must be slow enough for the crystal to "keep up"; therefore the requirement that $\omega_1 \approx \omega_2 \approx \omega$ can be imposed. The index of refraction of the material, which enters into the magnitude of the wavenumber of the optical field, k, in Eqn. (2.24), is given by

$$\begin{aligned} n =& n_0 + n_1 \\ =& n_0 - \frac{1}{2} n_0^3 r_{\text{eff}} E_{sc} e^{iKx} . \end{aligned} \tag{2.26}$$

Defining the complex coupling constant to be

$$\gamma \equiv \frac{i\omega}{4c} r_{\text{eff}} E_{sc} \left(\frac{I_0}{A_1 A_2^*} \right) , \tag{2.27}$$

where $I_0 = |A_1|^2 + |A_2|^2$ is the total intensity, and using the slowly varying field approximation,[16]

$$\frac{\partial^2 A_j}{\partial z^2} \ll k \frac{\partial A_j}{\partial z} , \tag{2.28}$$

in Eqns. (2.24) and (2.25) results in the following coupled differential equations for A_1 and A_2,

$$\begin{aligned} \cos\theta_1 \frac{\partial A_1}{\partial z} &= -\gamma \frac{A_1 A_2^*}{I_0} A_2 - \frac{\alpha}{2} A_1 \\ \cos\theta_2 \frac{\partial A_2}{\partial z} &= \gamma^* \frac{A_1^* A_2}{I_0} A_1 - \frac{\alpha}{2} A_1 , \end{aligned} \tag{2.29}$$

where α is the linear absorption of the crystal such that $I(\ell) = I(0) e^{-\alpha \ell}$. Using $I_j = |A_j|^2$ and $A_j = \sqrt{I_j} e^{i\phi_j}$, Eqn. (2.29) can be rewritten for the magnitude and phase of A_1 and A_2:

$$\begin{aligned} \cos\theta_1 \frac{\partial I_1}{\partial z} &= -\Gamma \frac{I_1 I_2}{I_0} - \alpha I_1 \\ \cos\theta_2 \frac{\partial I_2}{\partial z} &= \Gamma \frac{I_1 I_2}{I_0} - \alpha I_2 \\ \cos\theta_1 \frac{\partial \psi_1}{\partial z} &= \gamma_i \frac{I_2}{I_0} \\ \cos\theta_2 \frac{\partial \psi_2}{\partial z} &= \gamma_i \frac{I_1}{I_0} , \end{aligned} \tag{2.30}$$

where $\gamma = \frac{1}{2}\Gamma + i\gamma_i$. In this configuration, I_2 is amplified by energy coupling from I_1, and the maximum coupling occurs when $\gamma_i = 0$, that is, when E_{sc} is purely imaginary. In the one carrier, one species solution, this occurs when $E_0 = 0$ or when E_0 becomes large.

2.4.2 Solutions to the coupled wave equations

The solution of Eqn. (2.30) can be obtained for the symmetric case of $\theta_1 = \theta_2 = \theta$ by first making the change of variables $z = s(\cos\theta)$. The resulting solutions for I_1 and I_2 are given by

$$\begin{aligned} I_1(s) &= \frac{I_0 e^{-\alpha s}}{1 + [I_2(0)/I_1(0)]e^{\Gamma s}} \\ I_2(s) &= \frac{I_0 e^{-\alpha s}}{1 + [I_1(0)/I_2(0)]e^{-\Gamma s}} \,. \end{aligned} \tag{2.31}$$

For $[I_2(0)/I_1(0)]e^{\Gamma s} \gg 1$, the two-beam coupling constant is

$$\Gamma = \frac{1}{s}\ln\left[\frac{I_2(s)}{I_1(s)}\frac{I_1(0)}{I_2(0)}\right]. \tag{2.32}$$

In Eqn. (2.32), $I_1(s)$, $I_2(s)$, $I_1(0)$, and $I_2(0)$ are taken as values measured just within the surface of the material; however, since the symmetric geometry implies equal reflection and transmission coefficients, the values measured outside the crystal surface will be sufficient in determining the coupling constant because only the ratios of I_1 and I_2 enter into the equation.

2.5 Other considerations

So far, the discussion has concentrated on the ideal photorefractive crystal model, in the situation with zero applied field and only photoionizable donor and acceptor sites. The following discussion is directed at some additional effects present in real materials that have been observed in some cases to have significant effects. These include temperature dependent dark conductivity arising from the

presence of thermally excited sites, and the additional drift effect on the photoexcited charge carriers from external fields. A complete discussion on the experimental results of dark conductivity and its effect on the photorefractive properties of SBN is presented in Chapter 5, and the effect of external fields in increasing the photorefractive gain and reducing the response time is given is Chapter 6.

2.5.1 Dark conductivity

In Section 2.3, the photorefractive effect was attributed to photoexcitable donors and acceptors in the material. In addition to the photoexcited carriers generated by the donors (and acceptors for cases where hole transport is significant) in a photorefractive material, there is also the presence of thermally excited sites, denoted by β_e (and β_h) in the rate equations. The result is a non-photoactive, dark conductivity factor.[12,17]

In many doped semiconductor materials, dark conductivity is a function of temperature. Therefore, the effect of temperature-dependent dark conductivity on the photorefractive properties of materials would be to introduce an additional temperature-dependent factor, which for doped semiconductors is given by[18]

$$\beta = \beta_0 T^{3/2} e^{-E_t/k_B T} , \tag{2.33}$$

that generates a spatially uniform distribution of conduction electrons in competition with the photoexcitation process. The result would be to depress the gain coefficient through reduction of the space charge field, as can be seen from Eqn. 2.11. In optical storage applications, dark conductivity will result in decay of the grating depth through recombination of electrons due to the dark current. The equivalent situation for this in the case of the capacitor analogy would be a leaky capacitor with some finite resistance which reduces the density of charges separated by the grating period.

Significant dark conductivity has been observed through variations in the dark decay time in Cr-doped bulk GaAs,[19] and also in Cr-doped SBN:60 and SBN:75 over otherwise comparable Ce-doped and Rh-doped SBN:60.[17] The observed result has been sizable variations in the photorefractive gain as a function of temperature. In addition, at low intensities below some threshold, the photorefractive grating buildup will be limited by the leakage current. Although this causes an overall reduction in photorefractive coupling gain, this property has potential applications in thresholding devices provided there is some mechanism for varying this cutoff value by controlling the dark conductivity.

2.5.2 External applied fields

The presence of external dc fields is accounted for in the band transport equations and solutions through the bias term E_0 in the Fourier expansion for the space charge field. The physical description for the role of the dc term is that it drives the electrons into their traps against the built-up retarding field as they accumulate in the regions of low intensity. For sufficiently large fields, this will allow the space charge field to approach the maximum space charge field E_N instead of being limited by the diffusion field E_d. This property has been successfully used to enhance the photorefractive gain in Cr-doped SBN:60, and it also provides another mechanism for external control of the photorefractive effect.[20]

2.6. Summary

The photorefractive band transport was developed and solved for the one species, one carrier (electron) case. The steady-state and time dependent relations for the space charge field were derived by solving the Kukhtarev band transport equations for small modulation depths, and these results were used to obtain

the steady-state two-beam coupling constant Γ and response time τ. The effects of thermally excited sites competing with photoexcitation, or dark conductivity effects, and external fields were also considered.

2.7. References for Chapter 2

1. N.V. Kukhtarev, V.B. Markov, and S.G. Odulov, "Transient energy transfer during hologram formation in $LiNbO_3$ in external electric field," *Opt. Commun.* **23**, 338-343 (1977).

2. N.V. Kukhtarev, V.B. Markov, S.G. Odulov, M.S. Soskin, and V.L. Vinetski, "Holographic storage in electro-optic crystals. I. Steady state," *Ferroelectrics* **22**, 949-960 (1979).

3. N.V. Kukhtarev, "Kinetics of hologram recording and erasure in electro-optic crystals," *Sov. Tech. Phys. Lett.* **2**, 438-440 (1976).

4. J. Feinberg, D. Heiman, A.R. Tanguay, and R.W. Hellwarth, "Photorefractive effects and light-induced charge migration in barium titanate," *J. Appl. Phys.* **51**, 1297-1305 (1980); errata **52**, 537 (1981).

5. E. Ochoa, F. Vachss, and L. Hesselink, "Higher-order analysis of the photorefractive effect for large modulation depths," *J. Opt. Soc. Am. B* **3**, 181-187 (1986).

6. G.C. Valley, "Short-pulse grating formation in photorefractive materials," *IEEE J. Quantum Electron.* **QE-19**, 1637-1645 (1983).

7. P. Yeh, "Fundamental limit of the speed of photorefractive effect and its impact on device applications and materials research," *Appl. Opt.* **26**, 602-604 (1987).

8. R.R. Neurgaonkar and W.K. Cory, "Progress in photorefractive tungsten bronze crystals," *J. Opt. Soc. Am. B* **3**, 274-282 (1986).

9. R.R. Neurgaonkar, W.K. Cory, J.R. Oliver, M.D. Ewbank, and W.F. Hall, "Development and modification of photorefractive properties in the tungsten bronze family crystals," *Opt. Eng.* **26**, 392-405 (1987).

10. A. Agranat, V. Leyva, and A. Yariv, "Voltage-controlled photorefractive effect in paraelectric $KTa_{1-x}Nb_xO_3$:Cu,V," *Opt. Lett.* **14**, 1017-1019 (1989).

11. A. Yariv and P. Yeh, *Optical Waves in Crystals* (New York: Wiley, 1984).

12. M.D. Ewbank, R.R. Neurgaonkar, W.K. Cory, and J. Feinberg, "Photorefractive properties of strontium-barium niobate," *J. Appl. Phys.* **62**, 374-380 (1987).

13. J.E. Geusic, S.K. Kurtz, L. Van Uitert, and S.H. Wemple, "Electro-optic properties of some ABO_3 perovskites in the paraelectric phase," *Appl. Phys. Lett.* **4**, 141-143 (1964).

14. A. Agranat, K. Sayano, and A. Yariv, "Photorefractive diffraction gratings in KTN:Cr,Fe in the paraelectric phase using the quadratic electro-optic effect," paper PD-1, OSA Topical Meeting on Photorefractive Materials, Effects, and Devices, Los Angeles, CA (1987).

15. J.B. Thaxter and M. Kestigian, "Unique properties of SBN and their use in a layered optical memory," *Appl. Opt.* **13**, 913-924 (1974).

16. A. Yariv, *Quantum Electronics*, (New York: Wiley, 1989).

17. K. Sayano, G.A. Rakuljic, A. Agranat, A. Yariv, and R.R. Neurgaonkar, "Photorefractive dark conductivity in Cr-doped strontium barium niobate," *Opt. Lett.* **14**, 459-461 (1989).

18. S.M. Sze, *Semiconductor Devices – Physics and Technology*, (New York: Wiley, 1985).

19. L.J. Cheng and A. Partovi, "Temperature and intensity dependence of photorefractive effect in GaAs," *Appl. Phys. Lett.* **49**, 1456-1458 (1986).

20. K. Sayano, A. Yariv, and R.R. Neurgaonkar, "Enhanced photorefractive gain in Cr-doped strontium barium niobate with an external dc field," *J. Appl. Phys.* **67**, 1594-1596 (1990).

CHAPTER THREE

Characteristics and Preparation of Materials

3.1. Introduction

A wide variety of materials, including $LiNbO_3$,[1] $LiTaO_3$,[2] $Bi_{12}SiO_{20}$ (BSO),[3] $BaTiO_3$,[4] $KNbO_3$,[5] $KTa_{1-x}Nb_xO_3$ (KTN),[6] GaAs,[7] $Ba_{2-x}Sr_xK_{1-y}Na_yNb_5O_{15}$ (BSKNN),[8] and $Sr_xBa_{1-x}Nb_2O_6$ (SBN),[9] have been shown to exhibit the photorefractive effect. In the following chapters, the focus is on two classes of such materials. The first is the perovskite materials, which include $BaTiO_3$, which has been available commercially for a number of years,[10] and KTN, which has been one of the first photorefractive materials developed but has recently seen rekindled interest as a possible optical storage medium for optical memories and devices requiring electrical control of the photorefractive effect. The other is the ferroelectric tungsten bronze class of materials, which include SBN and BSKNN. These materials have been the subject of recent study as possible nonlinear wave mixing media for phase conjugation, beam mixing and cleanup, optical image processing, and optical computing applications.

3.2 Potassium tantalate niobate

Potassium tantalate niobate was one of the first materials in which the photorefractive effect was identified, but it has seen little experimental interest for optical applications until recently.[6,11] These materials had been considered difficult to grow, but recently large (on the order of cm), high quality KTN crystals have been grown successfully through careful control of growth parameters, and high diffraction efficiencies on the order of 50% in 3 mm-thick samples have been measured.[12,13]

3.2.1. Perovskite crystal structure

The ideal perovskite structure has the general formula of ABO_3, with A having a 1+ or 2+ oxidation state, usually being a Group I or II element, and B having an oxidation state of 5+ or 4+, respectively. As shown in Fig. 3-1, the structure is body-centered cubic, with A at the corners, B at the body centers, and O at the face centers. This type of crystal encompasses a wide range of materials, including $BaTiO_3$, $LiNbO_3$, $LiTaO_3$, $KNbO_3$, $KTa_{1-x}Nb_xO_3$, and $K_{1-y}Li_yTa_{1-x}Nb_xO_3$. In the latter two materials, the A and B sites are occupied interchangably by the combination A_1/A_2 and B_1/B_2, with fractional concentrations y and x, respectively, with the Nb/Ta and Li/K ratios having a significant effect on the material and optical properties of the crystal.

3.2.2. Material properties and phase transitions

The KTN crystals have been grown at the California Institute of Technology by the top seeded solution growth, where the crystal boule forms on a seed that is submerged in a molten flux containing K, Ta, Nb, and dopant element salts.[12,13] The dopants used successfully in the past include Cu-V[13] and Cr-Fe.[12] Combinations of two dopants were often used to obtain high optical quality results through charge compensation, since the dopants must displace atoms from the ideal lattice instead of filling vacant sites. Among the dopant combinations, the Cr-Fe combination has previously produced high diffraction efficiency in KTN and has been the focus of this work.

Samples of KTN for the optical measurements described in this work were prepared as needed from the boules. The resulting as-grown boules were transparent, for the most part with high optical quality and well-defined faces along the crystallographic axes. Samples, typically about 5 mm × 10 mm and approximately

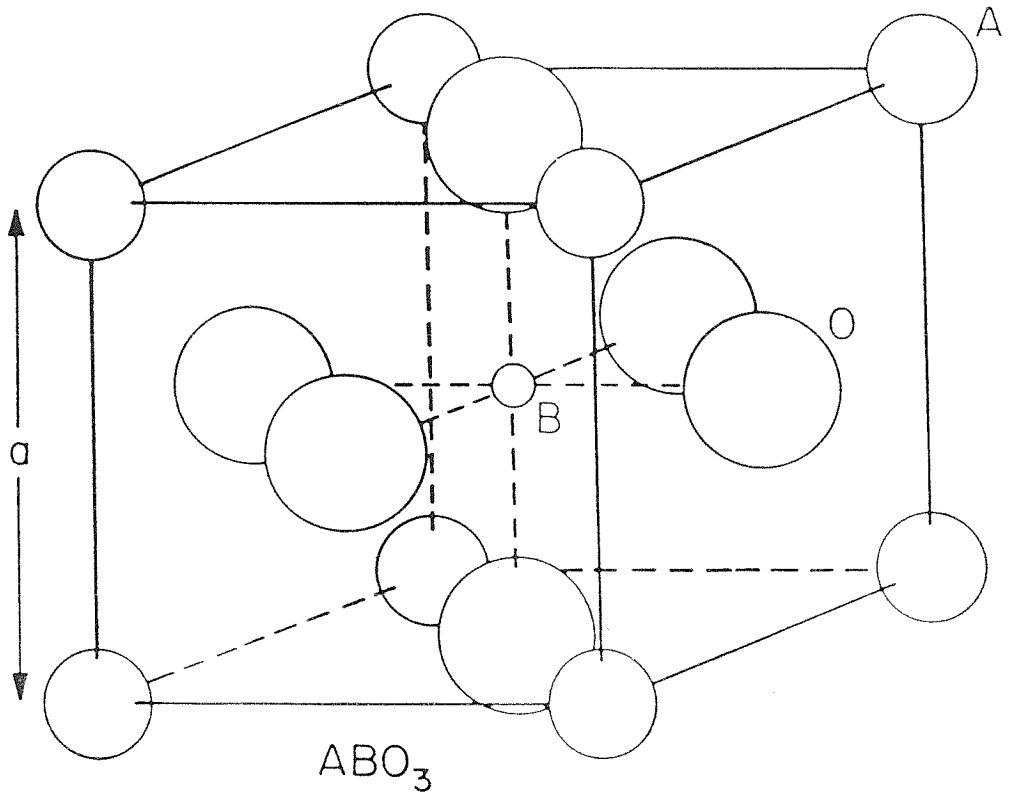

Fig. 3-1: Perovskite crystal structure with A at the corners, B at the body centers, and O at the face centers.

2-3 mm thick, with as much uniformity and as few visible defects as possible, were cut from the boule and hand-polished using varying grades of silicon carbide, and with 0.3 μm alumina as the final step of the process. Recently, significantly improved results in minimizing scattering from surface defects and distortion from non-planar surfaces have been achieved using a 3 μm diamond suspension and then a 0.05 μm alumina suspension with a polishing machine as the final steps in the polishing procedure.

Cr,Fe-doped crystals with varying dopant concentrations and ratios of Fe to Cr have been grown. The usual composition was about 3 to 6 % per mole of dopants in the flux. The absorption spectra of some KTN:Cr,Fe samples, measured over a wavelength range from 350 to 1100 nm using a spectrophotometer, are shown in Fig. 3-2. The as-grown, polished crystals showed a strong absorption band centered around 600 nm, which indicates the photoabsorption band of the dopants. A correction for the surface reflection was made by subtracting the measured front surface reflection at 514.5 nm.

In KTN:Cr,Fe, the Cr has been deemed to be the active photoionizable donor, although Fe has had significant effects in KTN, $BaTiO_3$, and other crystals. Some as-grown KTN crystals had a high percentage of Cr^{6+} instead of Cr^{3+}, which was determined from the deep red or reddish brown color of these samples. To increase the donor concentration, these crystals were reduced by sealing them in a quartz ampule with an oxygen deficient environment of approximately 1/4 to 1/3 atm of Ar and heating for several hours at 700-800° C. Successfully reduced crystals showed a color change to emerald green, indicating a higher concentration of Cr^{3+} over its original state, and also showed a much faster response time. Fig. 3-2 also shows the absorption spectrum of the samples after they were reduced, which indicates increased photoabsorption near 550 nm.

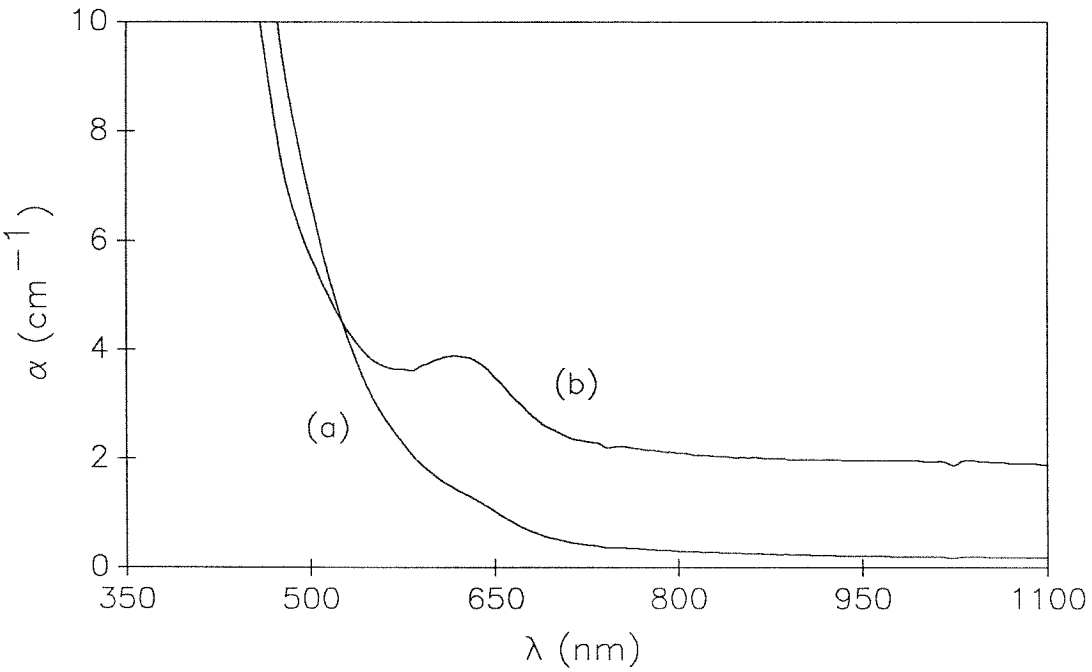

Fig. 3-2: Absorption spectrum of (a) as-grown KTN:Cr,Fe and (b) same KTN:Cr,Fe after reduction of Cr^{6+} by heating in Ar.

The ferroelectric phase transition temperature T_C of KTN is a strong function of the Nb concentration x. In the two extreme cases, $KNbO_3$ has a T_C of approximately 698 K, while $T_C \approx 4$ K for $KTaO_3$.[14] Crystals with lower concentrations of Nb have been found in the past to be easier to grow, but have the disadvantage that they need to be cooled down to temperatures as low as 100 K to be close enough to T_C for the photorefractive effects to be large enough to be observed. The change in T_C is at a rate of about 8.5 K/1% per mole Nb, with $T_C \approx 300$ K at $x = 0.35$.[15] At $T > T_C$, KTN is cubic and exhibits only the quadratic electro-optic effect, which requires an external bias field for readout. In the ferroelectric phase when $T < T_C$, the crystal can be poled by cooling through T_C with an applied field for beam coupling experiments using the linear effect. KTN crystals with significant diffraction efficiency and T_C as high as 310 K have been successfully grown by iteratively increasing the Nb concentration.

The phase transition temperatures were experimentally determined by measuring the low frequency capacitance as a function of temperature and looking for the discontinuity in the dielectric constant at the phase boundaries.[13] Fig. 3-3 shows the circuit diagram, where typical values used to measure the voltage drop V_s across the load resistor were $\nu = 10$ Hz and $R_0 = 1$ KΩ so that $(\omega R_0 C)^2 \ll 1$. Therefore, the dielectric constant is given by

$$\epsilon = \left| Im\left\{ \frac{V_s/V_0}{2\pi\nu R_0 (A/d)} \right\} \right| . \tag{3.1}$$

Fig. 3-4 shows the relative dielectric constant ϵ_r vs. T plots of a KTN:Cr,Fe sample. The largest peak corresponds to the cubic to tetragonal transition, with the smaller peaks corresponding to the tetragonal to orthorhombic and other transitions.[16] As the Nb concentration exceeds 25 to 30%, the transition also changes from second to first order.

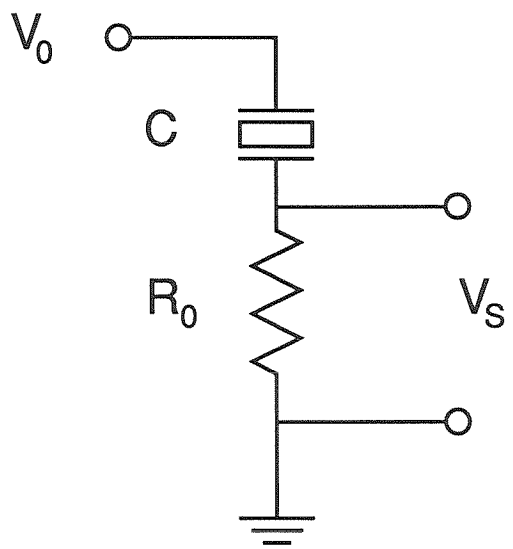

Fig 3-3: Method used to measure the low frequency capacitance and therefore determine the dielectric constant of the crystal. The conditions used were $R_0 = 1$ KΩ and $\nu = 10$ Hz.

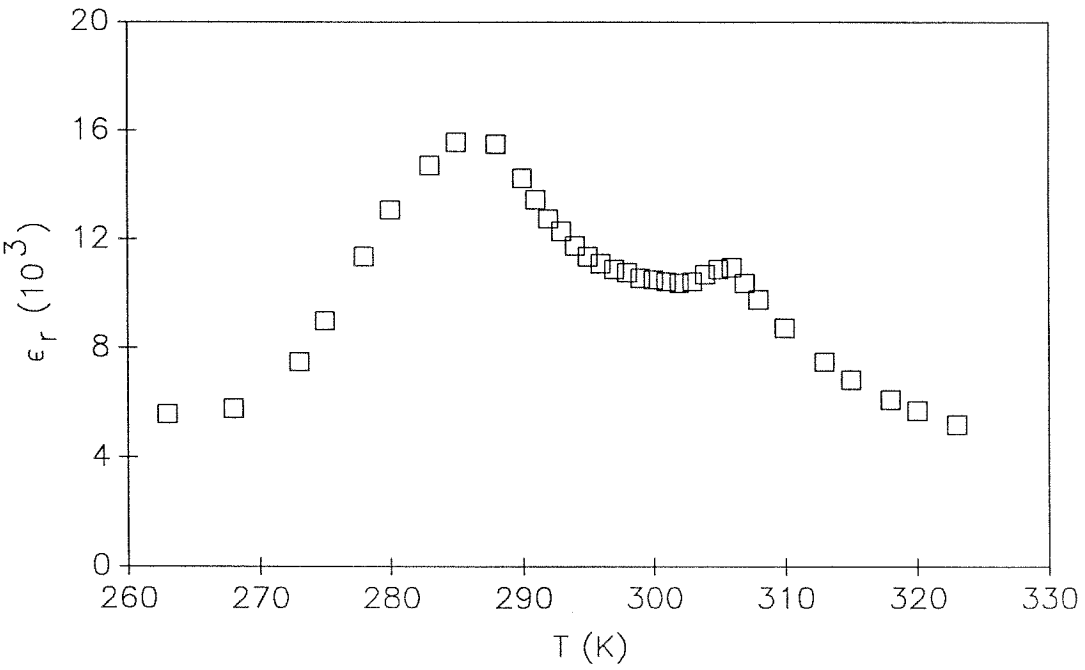

Fig. 3-4: Relative dielectric constant of KTN:Cr,Fe showing the sharp discontinuity in ϵ at the ferroelectric to cubic phase transition temperature.

3.3. Strontium barium niobate

Strontium barium niobate, a member of the tungsten bronze class of materials, has been shown to be photorefractive and useful for a wide variety of applications utilizing photorefractive materials.[17,18] It satisfies many of the desired characteristics of photorefractive materials, including high optical quality, high two-beam coupling gain, and real-time speed of response.[19] In addition, SBN has a number of distinct advantages over $BaTiO_3$ while being ferroelectric at room temperature with comparable nonlinear properties, making it a possible alternative to $BaTiO_3$ for many applications. Table 3-1 shows some of the relevant material properties of $BaTiO_3$ SBN:60, and SBN:75, including their phase transition temperatures and electro-optic coefficients, that have been published.[17,18]

3.3.1. Tungsten bronze crystal structure

Tungsten bronze ferroelectrics, particularly $Sr_xBa_{1-x}Nb_2O_6$ (SBN:x), have been grown in a wide range of compositions for optical applications. The general tungsten bronze configuration can be represented by $(A_1)_4(A_2)_2C_4B_{10}O_{30}$ and $(A_1)_4(A_2)_2B_{10}O_{30}$, where A_1, A_2, C, and B are the 15-, 12-, 9-, and 6-fold coordinated sites in the lattice. A wide range of material properties is possible in SBN by varying the composition and relative concentrations of A_1, A_2, and B.[20] The structure of the tungsten bronze prototypic material is shown in Fig. 3-5, looking down the c axis of the crystal.[21]

3.3.2. Tungsten bronzes vs. $BaTiO_3$

SBN has been seen as holding promise for applications requiring photorefractive materials because of a number of distinct advantages over $BaTiO_3$, which has been the material of choice for some time. Both $BaTiO_3$ and SBN are ferroelectric at room temperature, with large electro-optic coefficients which translate

Material	T_C (K)	E-O Coeff (pm/V)	$n_i^3 r_{ij}/\epsilon_j$ (pm/V)	μ (cm^2/Vsec)	γ_R (cm^3/sec)
SBN:60	348	235	5.8	0.5	5×10^{-8}
SBN:75	329	1340	5.0	0.5	5×10^{-8}
$BaTiO_3$	401	1640	4.9	0.5	5×10^{-8}

Table 3-1: Material properties and phase transition temperatures of SBN:60, SBN:75, and $BaTiO_3$ (from Refs. [16,17]).

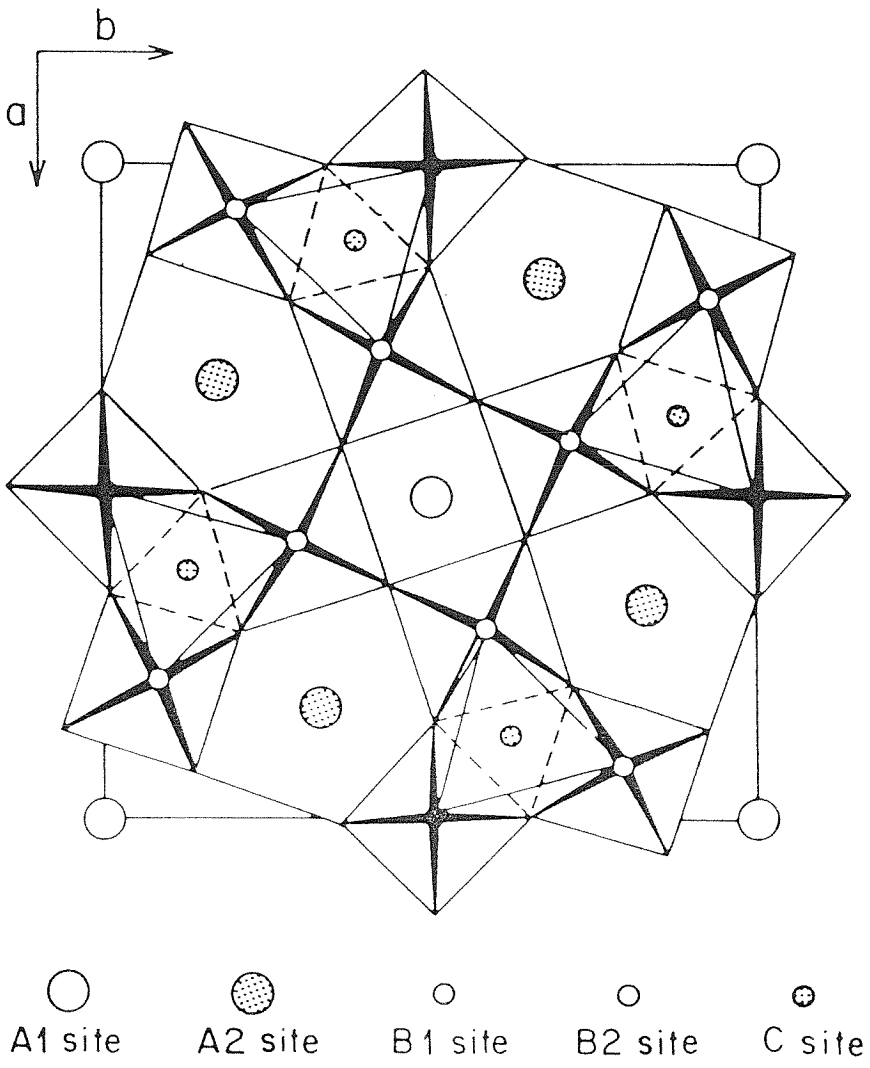

Fig. 3-5: Tungsten bronze crystal structure.

into large nonlinear effects and with storage lifetimes and response times that are comparable. Both materials have been grown in relatively striation-free cubes with sufficient optical quality to make optical measurements; however, SBN has a number of special characteristics that present interesting and significant advantages over $BaTiO_3$ in certain applications, especially in photorefractive nonlinear optics.

Ease of growth of SBN over some other materials has been reported. One of the reasons for this is that the SBN solution mixes congruently at around 1500° C in the case of SBN:60.[22] The crystal is also more rugged in withstanding the physical handling, high electric fields, and temperature variations which are necessary when poling the crystal or investigating field and temperature effects using these materials. In general, applying too large a field across $BaTiO_3$ has usually resulted in catastrophic damage of the crystal, while SBN can easily withstand fields of up to 30 kV/cm before catastrophic depoling destroys the crystal. Also, large size crystals with high optical quality are possible in SBN, which presents advantages in constructing optical systems utilizing these materials. SBN crystals as large as 3 cm on each side have been grown, although recent work in $BaTiO_3$ has succeeded in growing comparably sized cubes as well. In $BaTiO_3$, some anisotopies are introduced by a tetragonal to orthorhombic phase transition point at 283 K, but this point is as low as 120 K in SBN, minimizing this problem. SBN has a simple phase transition (4/mmm to 4mm), with no ferroelectric twinning that is difficult to remove by poling. In addition, $BaTiO_3$ has natural 90° domains, while the domains in SBN are 180° and therefore occur only along the longitudinal axis, which is a consideration in poling the crystal.

SBN also has a wide variability in the electro-optic and photorefractive characteristics, whereas these properties are usually fixed in $BaTiO_3$. Unlike $BaTiO_3$,

which has a fixed composition, the crystal structure of SBN is incompletely filled, so dopants can be added to fill these vacancies. On the other hand, doping $BaTiO_3$ involves substitutions in its filled crystal lattice, although substitution may also occur in SBN. In addition, the Sr/Ba ratio in SBN can be varied from 0.2 to 0.8, with corresponding changes in T_C and the electro-optic coefficients. As an example, for SBN:50, T_C = 401 K and r_{33} = 180 pm/V. For SBN:75, which is the highest Sr concentration achieved with sufficient optical quality to allow beam coupling experiments, T_C = 329 K and r_{33} = 1400 pm/V.[17]

3.3.3. Material properties and dopants

The SBN crystals that were studied in this work were all grown and prepared at Rockwell Science Center using the Czochralski method for growth.[17,19,23–26] Individual samples were cut and polished from the resulting boules which were typically 2-3 cm in diameter. Samples typically in the form of cubes approximately 6 mm on each side were cut from the boules and polished to an optical quality finish on all sides. Although striations, or inhomogeneities in the crystal, were a problem with some samples in the past, their adverse effects have been minimized in recently grown samples. Electrodes were evaporated onto the two surfaces in the direction of the *c* axis to establish a good electrical contact for the poling field and subsequent experiments with external fields. The crystals were then poled by heating them above their phase transition temperatures, to about 120° C, and then cooling them slowly through the phase transition with an applied field of 8-10 kV/cm.[17]

The dominant electro-optic coefficient in SBN is r_{33}, which means the ideal configuration has the space charge field and therefore the grating period parallel to the *c* axis. Larger unit cell tungsten bronzes such as BSKNN tend to have r_{51}

as the dominant coefficient, requiring a different orientation of the space charge field to achieve the maximum possible effect.

Undoped SBN is transparent and photorefractive to some degree, possibly due to trace impurities introduced during growth, but doping the crystals with Ce has been found to significantly improve their photorefractive properties. The SBN unit cell has 10 NbO_6 octahedra, with only 5 alkaline earth cations for 10 interstitial sites.[21] The incompletely filled structure can host a variety of dopants, and in this work, SBN crystals with a variety of dopant types and concentrations were studied and compared. These were: (1) Ce-doped SBN:60, used as a base line for comparison with newer compositions in SBN since these have already been widely characterized;[19,22] (2) Ce- and Ca- doped SBN, where the optically inert Ca ions were used to force the Ce atoms into the smaller 9-fold coordinated sites, resulting in different photoionization characteristics;[23] (3) three Cr-doped SBN:60, with 0.01, 0.016, and 0.03 wt. % of Cr in the 6-fold sites;[24,25] (4) Cr-doped SBN:75, with 0.0015 wt. % of Cr;[25] and (5) two Rh-doped SBN:60, each doped with 0.015 wt. % of Rh.[26]

3.4. Experimental figures of merit

In developing new materials, there are often trade-offs involved among the numerous parameters. A given material will often satisfy only some of the desired characteristics, so in comparing different materials, it is convenient to have a set of figures of merit in order to have one fixed standard for experimental results. In this work, the magnitude of the photorefractive effect of these materials were compared and characterized through their measured diffraction efficiencies, or their two-beam coupling constants for crystals with dominant linear electro-optic effects where beam coupling is present. The exponential time constants for

grating buildup, defined as the $1 - e^{-1}$ rise time, was used to characterize the speed of the photorefractive effect.

3.4.1. Diffraction efficiency

The magnitude of the photorefractive effect in any material can be determined by its diffraction efficiency, since it is a function of the index modulation depth. The relation between the index depth n_1 and the efficiency η has been derived by Kogelnik, which is given by[27]

$$\eta = \sin^2\left(\frac{\pi n_1 d}{\lambda \cos\theta}\right), \tag{3.2}$$

for the symmetric case of Fig. 2-3 with $\theta_1 = \theta_2$, and where d is the thickness of the material, n_1 is the amplitude of the spatial grating deviation, and θ is the half angle of the two writing beams.

Experimentally, the diffraction efficiency was defined as the intensity of the diffracted beam divided by the incident intensity of the probe beam. Since the crystals were place inside a vacuum chamber so they can be cooled below 0° C without condensation of ice on the surfaces, the reflectivity of the window also must be taken into account.

The experimental configuration used to measure the diffraction efficiency of the crystals is shown in Fig. 3-6. To observe the formation and decay of the grating in real time, the index grating was read using a low intensity He-Ne laser that was Bragg matched to the grating and with ordinary polarization so the probe beam does not contribute to the photorefractive effect. The readout beam intensity was set about two orders of magnitude less than the writing beams to avoid erasing or otherwise influencing the gratings. The rise and decay times were measured in real time and assumed to follow the standard exponential buildup and decay functional forms developed in Sec. 2.2.2.

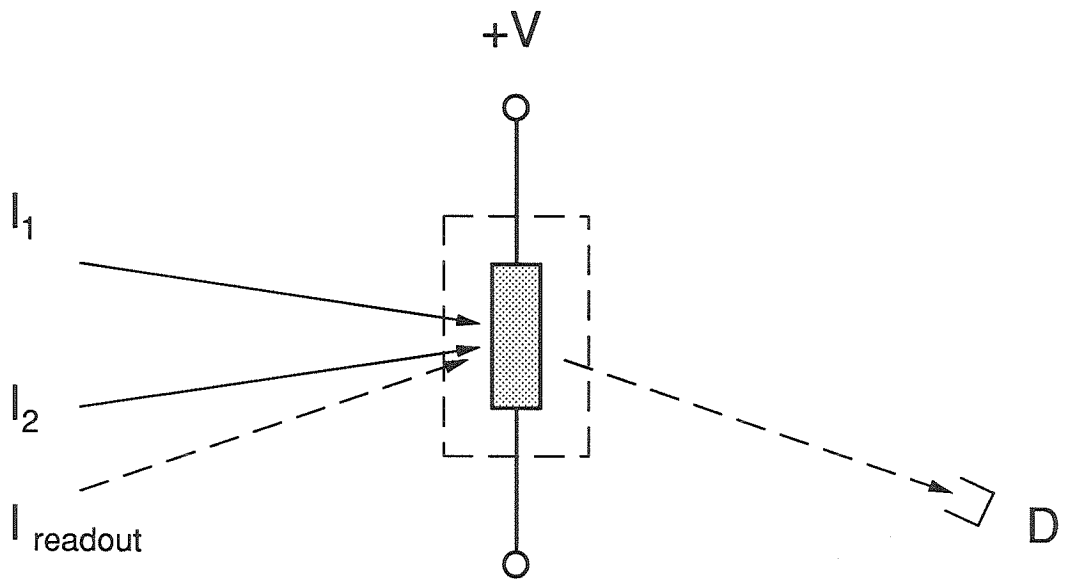

Fig. 3-6: Configuration used to measure the diffraction efficiency of KTN. A Bragg matched, low intensity He-Ne laser was used for readout.

3.4.2. Two-beam coupling constant

In ferroelectric crystals were there was a phase shift between the light interference pattern and the spatial index modulation pattern, beam coupling occurred with steady-state energy transfer from one beam to the other. The two-beam coupling constant defined in Eqn. (2.32) also relates to the index modulation depth in the steady state as

$$\Gamma = \frac{\omega}{c} n_{1,ss} \,. \tag{3.3}$$

This parameter is useful since many applications of ferroelectric materials in optical applications, such as phase conjugate mirrors and photorefractive oscillators, rely on two-beam coupling.

Two-beam coupling experiments in SBN were performed in a similar fashion to the diffraction measurements with cubic crystals, with the exception that the coupling constant was determined by measuring the two transmitted beam intensities simultaneously in real time. Eqn. (2.32) gave the definition of the two-beam coupling constant Γ, with $I_1(0)$, $I_2(0)$, $I_1(l)$, and $I_2(l)$ being the values inside the crystal. However, because the ratios of the intensities enter into the equation, and since the transmission coefficients can be assumed to be nearly the same for all four beams, the four intensities can be substituted by their values measured outside the crystal surface. In determining the grating period, the intersection angle inside the crystal is smaller by Snell's law; however, since $n_0 \sin\theta_i = \sin\theta$ and the optical wavelength inside the crystal is λ/n_0, the exterior incidence angle can be used to calculate the grating period:

$$\lambda_g = \frac{\lambda_i}{2\sin\theta_i} = \frac{\lambda/n_0}{2\sin\theta/n_0} = \frac{\lambda}{2\sin\theta} \,. \tag{3.4}$$

To achieve the maximum possible photorefractive effect, both for diffraction efficiency and two-beam coupling, crystals with as large a steady state index change

as possible are desired. Since $n_1 \propto n_0^3 r_{\text{eff}}$, crystals with large effective electro-optic coefficients would be ideal for high efficiency device applications since they will produce larger effects for a given space-charge field.

3.4.3. Response time

The photorefractive reponse time is an important parameter in cases requiring real-time operations or variability of the response time. In general, response time is proportional to intensity, according to Eqn. (2.16a), with t_0 being the fundamental limit of the time required to separate $N_{A,C}^-$ charges given the energy density deposited in the crystal as a result of the incident light intensity. There are additional limits in the carrier transport time across one grating period or the response time of the electro-optic effect to the Coulombic field of the displaced charge, but these are usually negligible compared to the space charge buildup time.

3.4.4. Photorefractive sensitivity

The photorefractive sensitivity gives an indication of the efficiency of the material, that is, how much optical energy is required to achieve a given index change in a certain period of time. The definition of photorefractive sensitivity S is given by[28]

$$S = \frac{n_1}{\alpha I_0 t}, \tag{3.5}$$

where n_1 is the transient index modulation, $I_0 t$ is the incident energy density, and α is the total absorption coefficient.

This parameter provides a means for comparing various materials with different compositions, dopants, and optical characteristics. As with the two-beam coupling constant, maximum sensitivity is obtained for a large index modulation depth and short response time.

3.5. Summary

KTN:Cr,Fe crystals were grown, cut, and polished for optical storage applications. The Cr,Fe combination was selected for the dopant based on past experience, and the Nb concentration was gradually increased to bring the phase transition temperature to near room temperature. Other samples of KTN:Cr,Fe were reduced to study the effect on its photorefractive properties.

SBN crystals doped with Ce, Ce and Ca, Cr, and Rh were studied as two-beam coupling wave mixing media. SBN has comparable applications and characteristics to $BaTiO_3$ which was previously used for such applications, and SBN has unique advantages over $BaTiO_3$ as well. The photorefractive figures of merit of diffraction efficiency, coupling constant, response time, and photorefractive sensitivity used to compare various materials were introduced.

3.6. References for Chapter 3

1. F.S. Chen, J.T. LaMacchia, and D.B. Fraser, "Holographic storage in lithium niobate," *Appl. Phys. Lett.* **13**, 223-225 (1968).

2. F.S. Chen, "Optically induced change of refractive indices in $LiNbO_3$ and $LiTaO_3$," *J. Appl. Phys.* **40**, 3389-3396 (1969).

3. A. Marrakchi, J.P. Huignard, and P. Günter, "Diffraction efficiency and energy transfer in two-wave mixing experiments with $Bi_{12}SiO_{20}$ crystals," *Appl. Phys.* **24**, 131-138 (1981).

4. J. Feinberg, D. Heiman, A.R. Tanguay, and R.W. Hellwarth, "Photorefractive effects and light-induced charge migration in barium titanate," *J. Appl. Phys.* **51**, 1297-1305 (1980).

5. P. Günter and F. Micheron, "Photorefractive effects and photocurrents in $KNbO_3$:Fe," *Ferroelectrics* **18**, 27-38 (1978).

6. F.S. Chen, "A laser-induced inhomogeneity of refractive indices in KTN," *J. Appl. Phys.* **38**, 3418-3420 (1967).

7. A.M. Glass, A.M. Johnson, D.H. Olson, W. Simpson, and A.A. Ballman, "Four-wave mixing in semi-insulating InP and GaAs using the photorefractive effect," *Appl. Phys. Lett.* **44**, 948-950 (1984).

8. R.R. Neurgaonkar, W.K. Cory, J.R. Oliver, W.W. Clark III, G.L. Wood, M.J. Miller, and E.L. Sharp, "Growth and ferroelectric properties of tungsten bronze $Ba_{2-x}Sr_xK_{1-y}Na_yNb_5O_{15}$," *J. Cryst. Growth* **84**, 629-637 (1987).

9. J.B. Thaxter and M. Kestigian, "Unique properties of SBN and their use in a layered optical memory," *Appl. Opt.* **13**, 913-924 (1974).

10. Lockheed-Sanders, 95 Canal St., Nashua, NH 03060.

11. R. Orlowski, L.A. Boatner, and E. Kratzig, "Photorefractive effects in the

cubic phase of potassium tantalate-niobate," *Opt. Commun.* **35**, 45-48 (1980).

12. A. Agranat, K. Sayano, and A. Yariv, "Photorefractive diffraction gratings in KTN:Cr,Fe in the paraelectric phase using the quadratic electro-optic effect," paper PD-1, OSA Topical Meeting on Photorefractive Materials, Effects, and Devices, Los Angeles, CA (1987).

13. A. Agranat, V. Leyva, and A. Yariv, "Voltage-controlled photorefractive effect in paraelectric $KTa_{1-x}Nb_xO_3$:Cu,V," *Opt. Lett.* **14**, 1017-1019 (1989).

14. F.S. Chen, J.E. Geusic, S.K. Kurtz, J.G. Skinner, and S.H. Wemple, "Light modulation and beam deflection with potassium tantalate-niobate crystals," *J. Appl. Phys.* **37**, 388-398 (1966).

15. A. Agranat, V. Leyva, K. Sayano, and A. Yariv, "Photorefractive properties of $KTa_{1-x}Nb_xO_3$ in the paraelectric phase," *Proc. SPIE* **1148**, 52-66 (1989).

16. C.M. Perry, R.R. Hayes, and N.E. Tornberg, in *Proceedings of the International Conference on Light Scattering in Solids*, M. Balkanski, ed. (New York: Wiley, 1975).

17. R.R. Neurgaonkar and W.K. Cory, "Progress in photorefractive tungsten bronze crystals," *J. Opt. Soc. Am. B* **3**, 274-282 (1986).

18. G.A. Rakuljic and A. Yariv, "Photorefractive materials for optical computing and image processing," *Proc. SPIE* **881**, 146-149 (1988).

19. G.A. Rakuljic, A. Yariv, and R.R. Neurgaonkar, "Photorefractive properties of undoped, Ce-doped, and Fe-doped single crystal $Sr_{0.6}Ba_{0.4}Nb_2O_6$," *Opt. Eng.* **25**, 1212-1216 (1986).

20. F.W. Ainger, W.P. Bickley, and G.V. Smith, "The search for new ferroelectrics with the tungsten bronze structures," *Proc. Brit. Ceram. Soc.* **18**, 221 (1970); T. Ikeda, K. Uno, K. Oyamada, A. Sagara, J. Kato, S. Takano, and H. Sato, "Some solid solutions of the $A_5B_{10}O_{30}$- and $A_6B_{10}O_{30}$-type tungsten

bronze ferroelectrics," *Jpn. J. Appl. Phys.* **17**, 341-348 (1978).

21. P.B. Jamieson, S.C. Abrahams, and J.L. Bernstein, "Ferroelectric tungsten bronze-type crystal structures. I. Barium strontium niobate $Ba_{0.27}Sr_{0.75}Nb_2O_6$," *J. Chem. Phys.* **48**, 5048-5057 (1968); "Ferroelectric tungsten bronze-type crystal structures. II. Barium sodium niobate $Ba_{4+x}Na_{2-2x}Nb_{10}O_{30}$," *J. Chem. Phys.* **50**, 4352-4363 (1969).

22. K. Megumi, N. Nagatsuna, Y. Kashiwada, and Y. Furuhata, "The congruent melting composition of strontium barium niobate," *J. Mater. Sci.* **11**, 1583-1592 (1976).

23. G.A. Rakuljic, K. Sayano, A. Agranat, A. Yariv, and R.R. Neurgaonkar, "Photorefractive properties of Ce- and Ca-doped $Sr_{0.6}Ba_{0.4}Nb_2O_6$," *Appl. Phys. Lett.* **53**, 1465-1467 (1988).

24. K. Sayano, A. Yariv, and R.R. Neurgaonkar, "Photorefractive gain and response time of Cr-doped strontium barium niobate," *Appl. Phys. Lett.* **55**, 328-330 (1989).

25. K. Sayano, A. Yariv, and R.R. Neurgaonkar, "Photorefractive properties of Cr-doped single crystal strontium barium niobate," *Proc. SPIE* **1148** (1989).

26. K. Sayano, A. Yariv, and R.R. Neurgaonkar, "Order of magnitude reduction of the photorefractive response time in rhodium-doped $Sr_{0.6}Ba_{0.4}Nb_2O_6$ with a dc electric field," *Opt. Lett.* **15**, 9-11 (1990).

27. H. Kogelnik, "Coupled wave theory for thick hologram gratings," *Bell Syst. Tech. J.* **48**, 2909-2947 (1969).

28. A.M. Glass, "The photorefractive effect," *Opt. Eng.* **17**, 470-479 (1978).

CHAPTER FOUR

Optical Information Storage in KTN

4.1. Introduction

Potassium tantalate niobate (KTN), a perovskite crystal which has the general formula of $KTa_{1-x}Nb_xO_3$, holds considerable promise for optical storage and optical information processing applications in the areas of optical computing and opto-electronic neural networks because of its high diffraction efficiency and the capability for electrical control and modulation of its large quadratic electro-optic effect in the paraelectric phase. Large diffraction efficiency, high optical quality crystals with phase transition temperatures at approximately 140 K have been previously studied, but these required bulky cooling and temperature control systems. One of the underlying goals of this work has been to increase the Nb concentration in order to raise the transition temperature closer to room temperature, where cooling requirements can be met with simpler systems, while maintaining the high optical quality and high efficiency of the material to enable the storage of multiple images with high resolution for optical memorites, optical neural networks, or similar applications.

4.2. Optical properties of as-grown KTN:Cr,Fe

The Cr, Fe combination of dopants has resulted in high diffraction efficiency with samples in previously reported work using low-temperature (approximately 20% Nb concentration, 140 K phase transition) crystals.[1] The dopants were usually introduced in pairs in order to realize charge compensation in the crystal structure, resulting in better optical quality growths with relatively high concentrations of impurities. Of the two dopants in the Cr,Fe combination, the Cr is believed to be

the photoactive dopant in this combination, although Fe by itself is also a known photoionizable donor for $LiNbO_3$, $BaTiO_3$, and SBN.[2,3]

4.2.1. Procedure for temperature controlled experiments

In order to take advantage of the large values of the electro-optic coefficients of KTN near its cubic to ferroelectric phase transition temperature, the samples were cooled to within 5 to 10 K of their Curie temperatures, where the relative dielectric constant was on the order of 10^4. For low temperature phase transition materials, that is, samples with T_C around 100 K, a vacuum chamber with a liquid nitrogen-cooled cold finger was used. A copper block mount with electrodes for applying the external field was mounted on the cold finger. Sapphire was used to electrically isolate the crystal but still provide good thermal conductivity between the crystal and the cold finger. The temperature controller that was used was able to maintain a temperature stability within 0.2 K after allowing time for the system to stabilize.

One of the efforts in KTN materials research has been to increase the phase transition to near room temperature by increasing the Nb concentration. For these crystals, with phase transitions near room temperature, a Peltier effect thermoelectric device, which can operate between 230 and 320 K with much better thermal stability than the liquid nitrogen system, was utilized. The physical dimensions of the chamber used with this cooling system also allowed for larger input angles to be used, giving the capability to experiment with a wider range of grating periods than the low temperature system would allow.

4.2.2. High temperature KTN

One of the problems with previously available KTN crystals was their low cubic to ferroelectric phase transition temperature, which required considerable

cooling in order to take advantage of the large electro-optic coefficient near the phase boundary. By increasing the Nb concentration in the crystals from approximately 20 up to 30 % per mole, samples with higher phase transition temperatures have been grown. The actual phase transition temperature was also affected to some degree by the concentration of the dopants. A number of high T_C samples have been successfully grown with phase transitions temperatures of up to 310 K.

The availability of samples with room temperature phase transitions enables or at least simplifies the construction of devices utilizing KTN as the holographic storage medium. The Nb concentration was increased iteratively in small steps, with each successive growth being used to furnish the seed for the next. There was also the added complication of the phase transition changing from a second order transition, where the dielectric constant of the crystal was continuous but the derivative discontinuous, to a first order transition, with discontinuities in both the ϵ and the derivative, when the relative Nb concentration x exceeded approximately 30%.[4] Figure 4-1 illustrates the dielectric constants of several KTN:Cr,Fe samples, with the discontinuity in the low frequency dielectric constant indicating the onset of the ferroelectric phase transition.

In some samples with T_C higher than room temperature, the formation of domain structures was also observed. These for the most part were eliminated by heating the crystal above T_C or by poling with an electric field of about 2 kV/cm. Some experiments in beam coupling were also performed with the crystal being poled and operated about 5 to 10° below the phase transition. These experiments generally showed two-beam coupling constants considerably less than what was obtained in other materials. However, large diffraction efficiencies were observed in these KTN crystals in their cubic phases with applied bias fields.

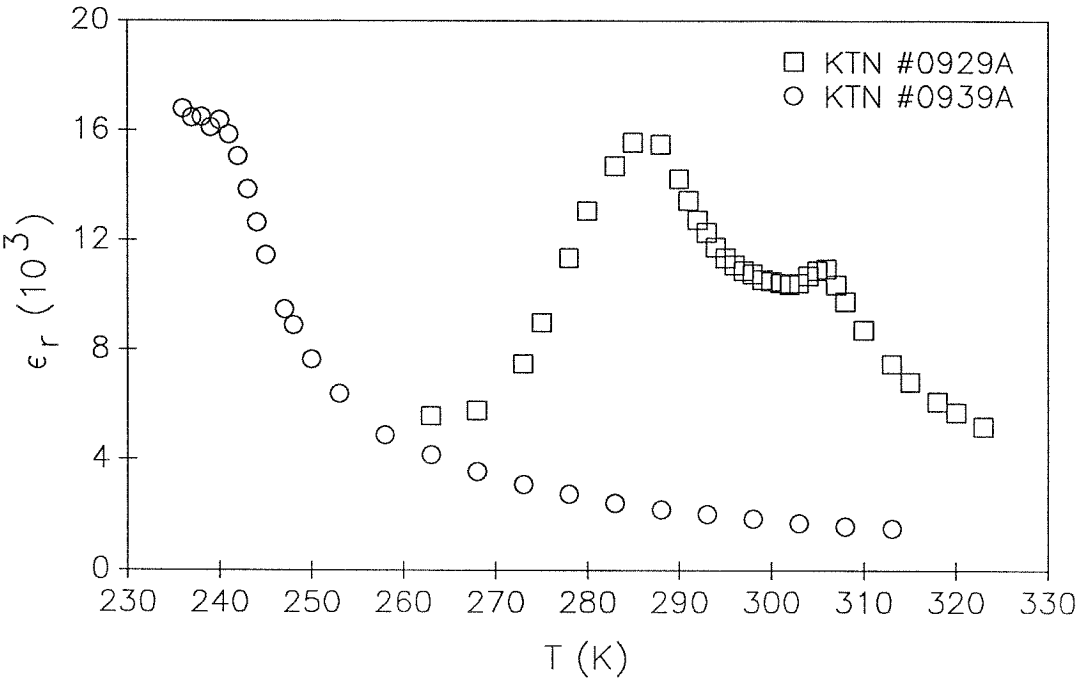

Fig. 4-1: Relative dielectric constant ϵ_r of as-grown KTN:Cr,Fe near the phase transition temperature.

4.2.3. Diffraction efficiency

The diffraction efficiency was used as the figure of merit to characterize paraelectric KTN since the primary aim for these materials is optical storage. In addition, beam coupling would not occur unless the crystals were poled and the measurements made in the ferroelectric phase, below the phase transition temperature. Diffraction efficiency was measured as illustrated in Fig. 3-6. The effects of surface reflection and absorption were not subtracted out of the measurements since these factors would have an effect on typical applications of these materials as well. However, a correction factor accounting for the reflection losses from the vacuum chamber windows have been made.

The procedure for the diffraction measurements was as follows. The crystal was illuminated by the two writing beams for the exposure period, which ranged from 5 to 15 sec at about 0.5 W/cm^2. The beams were then shut off by a shutter and one of the original writing beams, or a separate probe beam from a low intensity He-Ne laser that was Bragg matched to the photorefractive gratings, was used to measure the readout efficiency of the gratings. The probe beam intensity was low enough to not erase or otherwise affect the photorefractive gratings. At the end of the measurement, the gratings were erased by uniform illumination for a period much greater than the grating lifetime. The field E_0 was turned on during both the writing and readout phases.

Figures 4-2(a) and (b) show the experimentally measured diffraction efficiency as a function of applied field for two different as-grown KTN:Cr,Fe crystals. Sample A was grown with approximately 3% per mole of Cr and Fe dopants in the flux, and was 0.245 cm thick. On the other hand, sample B had a higher dopant concentration of about 9%, with the Cr/Fe ratio about 2 to 1. The Nb concentration in sample B was also slightly reduced, so that its phase transition temperature was

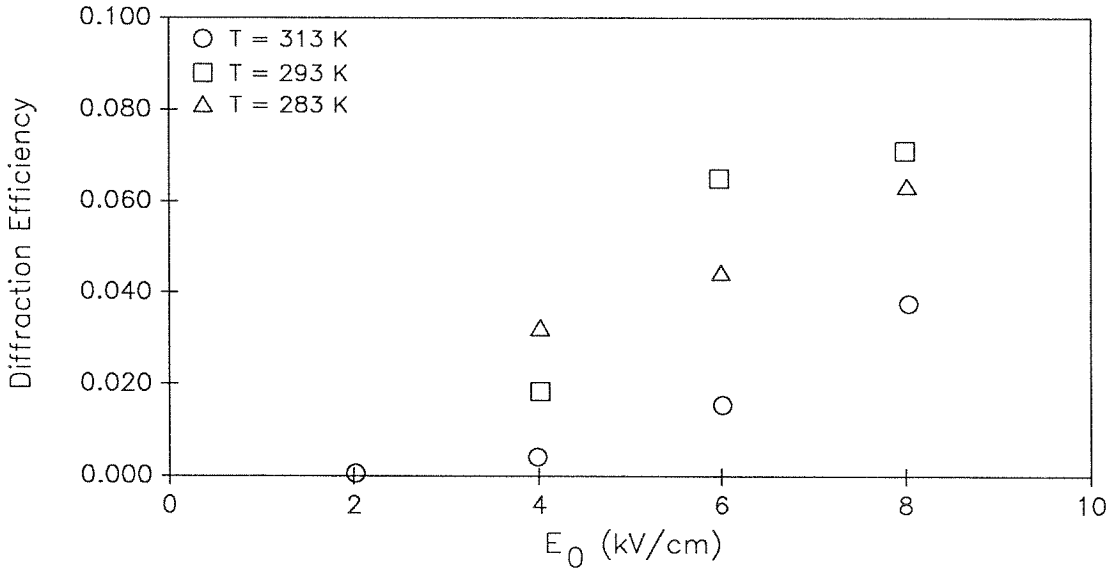

(a)

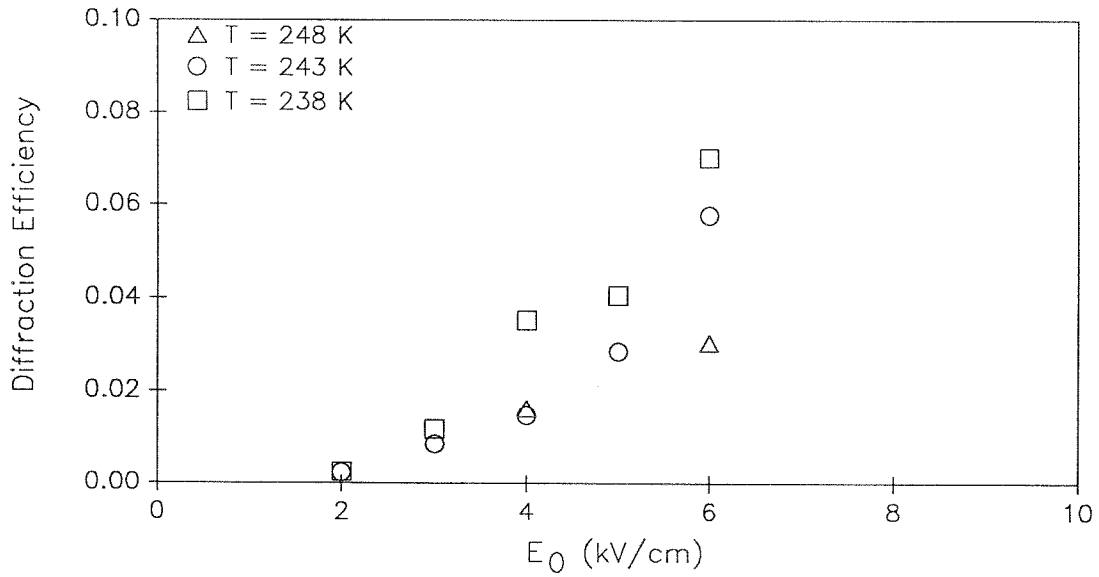

(b)

Fig. 4-2: Diffraction efficiency of as-grown KTN:Cr,Fe for (a) sample A (#0929A) with $T_C \approx 305$ K, and (b) sample B (#0939A) with $T_C \approx 238$ K.

measured at approximately 238 K, compared to 305 K in sample A. The crystal thickness of sample B was 0.28 cm.

Figure 4-2(a) shows the plot of diffraction efficiency of sample A as a function of applied field for T = 283, 293, and 313 K. The diffraction efficiency increases with E_0, which is expected from the index variation being proportional to $E_0 E_{sc}$. Ideally the diffracted beam intensity should go as $n_1 \propto E_0^2$, with deviation from the quadratic dependence due to the dependence of the space charge field on the applied field and other smaller effects. A maximum diffraction efficiency of 7.4% was achieved in this sample at T = 293 K and E_0 = 8 kV/cm. The crystal was exposed by two writing beams at 514.5 nm at 5 J/cm^2, with a grating period of approximately 2 μm.

The diffraction efficiency measurement results of sample B is shown in Fig. 4-2(b) for T = 238, 243, and 248 K. Although this crystal has a lower maximum diffraction efficiency of around 6% compared to sample A, it had much better optical quality by not having its ferroelectric phase transition just above room temperature and the resulting formation of domain walls. The exposure conditions from the writing beams was approximately 7.5 J/cm^2 with an incident wavelength of 514.5 nm and a grating period of 2 μm. In both cases the modulation index m $\approx$ 1 for maximum possible diffraction efficiency.

4.2.4. Dark decay time

The dark decay time of the KTN samples was measured by using a probe beam from a low intensity He-Ne laser, polarized orthogonally to the writing beams and with an intensity about 2 orders of magnitude less than that of the writing beams to avoid erasing the gratings, that was Bragg matched to the photorefractive gratings written using the Ar-ion laser. The intensity of the diffracted beam was

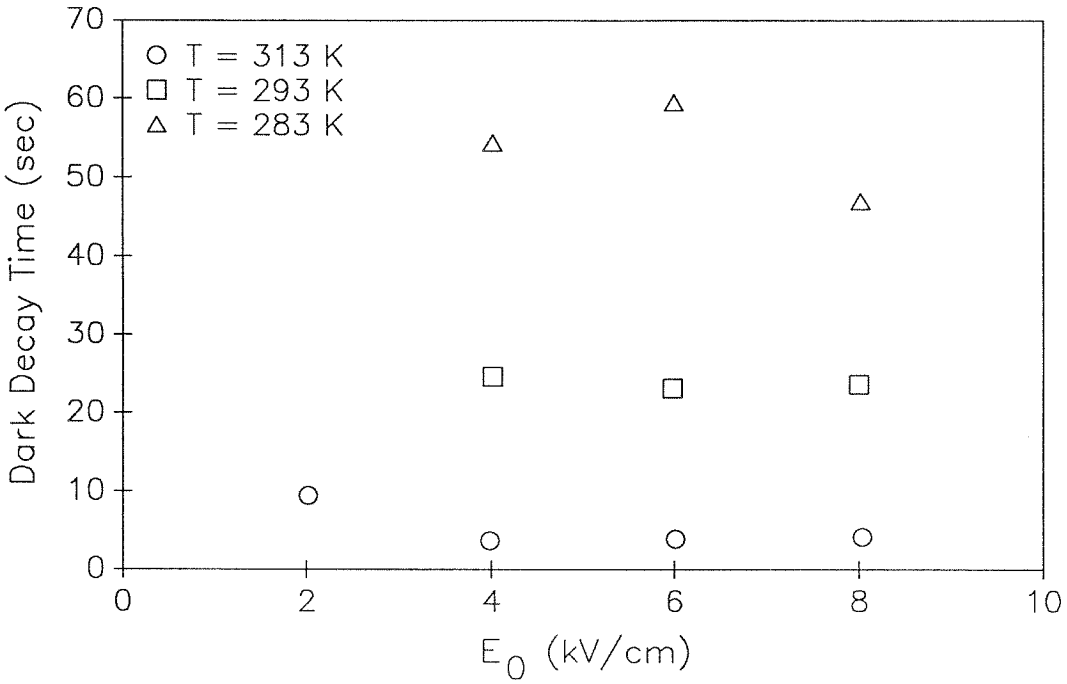

Fig. 4-3: Dark decay time of KTN:Cr,Fe, sample A.

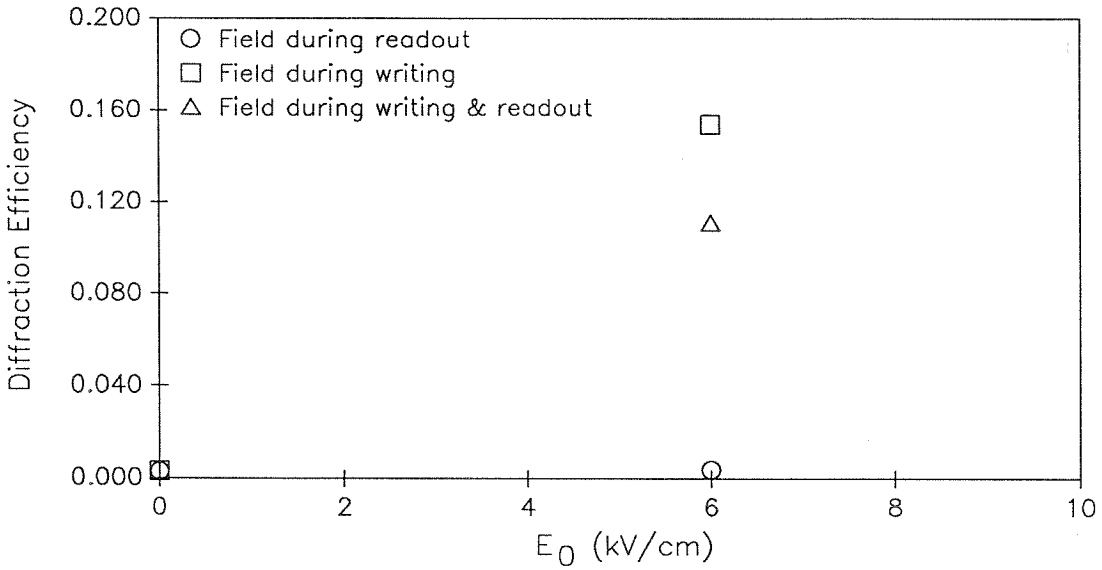

(a)

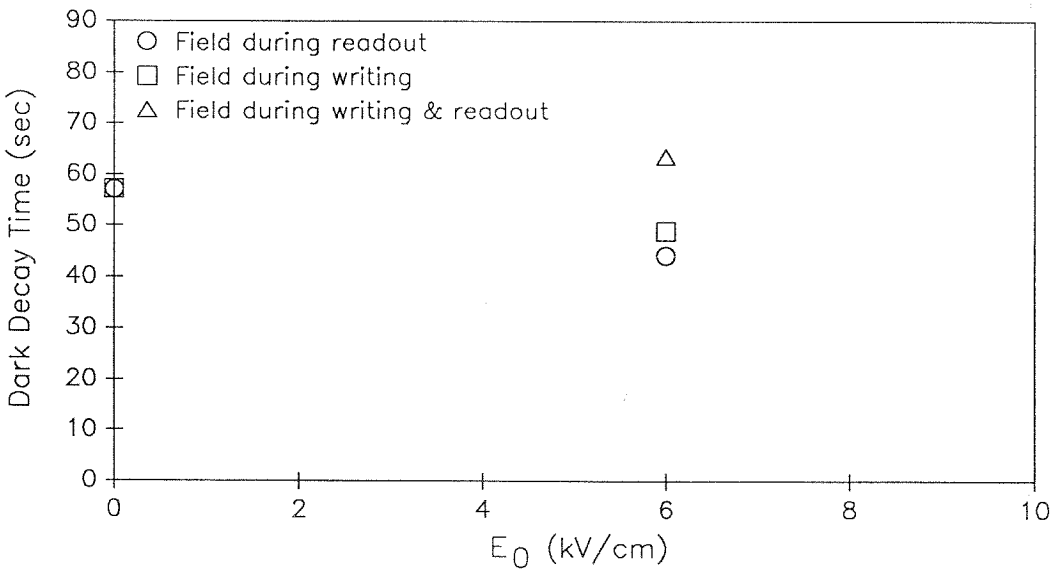

(b)

Fig. 4-4: Experimental results from KTN:Cr,Fe, sample A, after poling and cooldown to 273 K – (a) diffraction efficiency, and (b) dark decay time.

4.3. Reduction of as-grown KTN

As mentioned in Sec. 3.2.2, in as-grown KTN:Cr,Fe, the Cr ion often goes into the crystal as Cr^{6+}, instead of the photoactive Cr^{3+} state. In order to increase the Cr^{3+} concentration, the crystal was reduced by heating in an oxygen deficient atmosphere.

4.3.1. Procedure for reduction

Reduction was accomplished by baking the sample in an oxygen deficient atmosphere for several hours at temperatures of up to 800° C. The KTN:Cr,Fe crystal, cut from the same boule as sample A in the previous experiments, was sealed in a quartz ampule containing Ar at a pressure of 1/4 to 1/3 atmosphere at room temperature (so that $P \approx 1$ atm at the peak temperature) in order to moderate the reduction. Reduction by heating in a vacuum is also possible, but in most cases would result in too much reduction and reduction of other elements of the crystal in addition to the dopants.

The sample was then placed in a furnace and ramped up to the bake temperature of 750° C at a rate of about 90°/hr, allowed to soak for approximately 8 hours, and ramped back down to room temperature at 40°/hr to avoid large thermal shocks to the crystal. Experiments have indicated that the length of time the crystal is heated, beyond 1-2 hours is not a significant parameter in determining the degree of reduction.

No change in the crystal color or absorption spectrum was noticed after this process, so the procedure was repeated, with the crystal being heated up again to a bake temperature of 800° C for 2 hours, quenched to 560° at a rapid 120°/hr, then cooled slowly back to room temperature at the normal 40°/hr. The crystal was then repolished and used for the following measurements.

4.3.2. Experimental results

The reduced crystal showed considerable improvement in diffraction efficiency over the as-grown sample. From the low frequency capacitance measurements, shown in Fig. 4-5, the phase transition temperature was observed to have shifted slightly in the reduced crystal to the 280 to 285 K range.

Figure 4-6 shows the diffraction efficiency of the reduced crystal, with a maximum value of 14% at $T = 313$ K with an 8 kV/cm applied field. This is considerably higher than the 4% efficiency measured under comparable conditions in the as-grown crystal. The crystal thickness was 0.43 cm, and the total intensity of the writing beams were 0.5 W/cm^2, which becomes a 5 J/cm^2 exposure with the 10 sec exposure time.

The response time of the reduced KTN:Cr,Fe crystal is shown in Fig. 4-7 for several values of temperature ranging from 293 to 313 K. The measured values were similar to those measured in the as-grown sample. As in the measurements in the previous sections, the decay time was measured by monitoring the decay in the diffracted beam from a Bragg matched He-Ne probe laser.

4.4. Summary

Potassium tantalate niobate crystals with phase transition temperatures near room temperature have been grown with diffraction efficiencies approaching 10% in the as-grown samples. Reduction of the Cr^{6+} dopant to Cr^{3+} resulted in larger photorefractive effects, with up to 15% diffraction efficiency and 30 sec dark decay time at room temperature. The effect of temperature variations on these properties was also investigated.

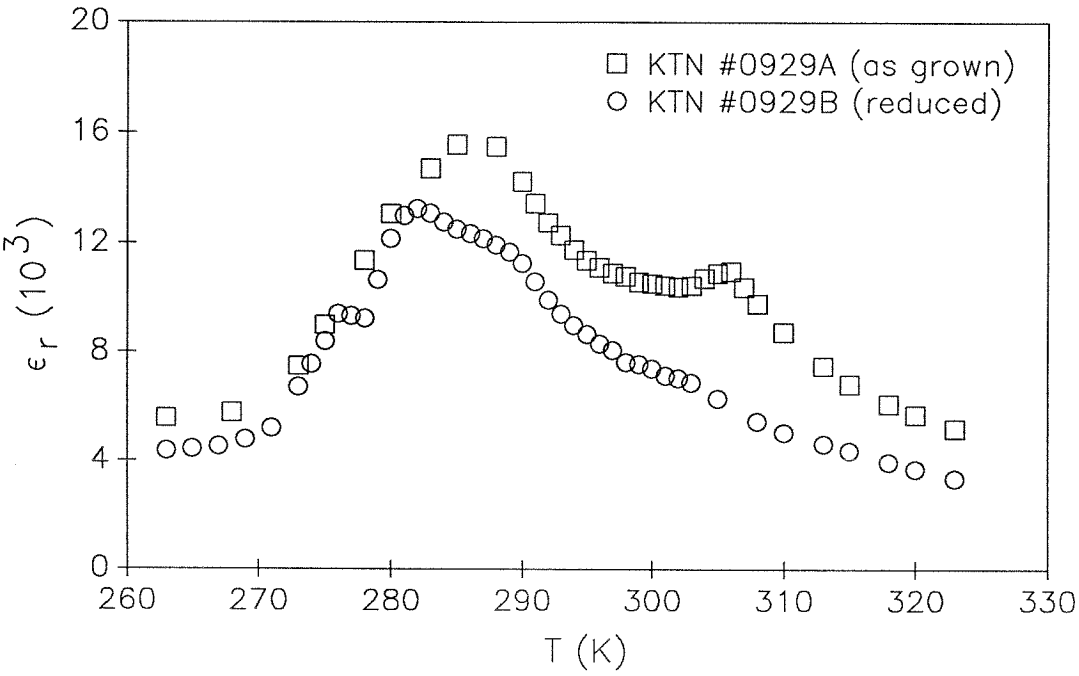

Fig. 4-5: Shift in the phase transition temperature of KTN:Cr,Fe (sample A, #929A) after reduction.

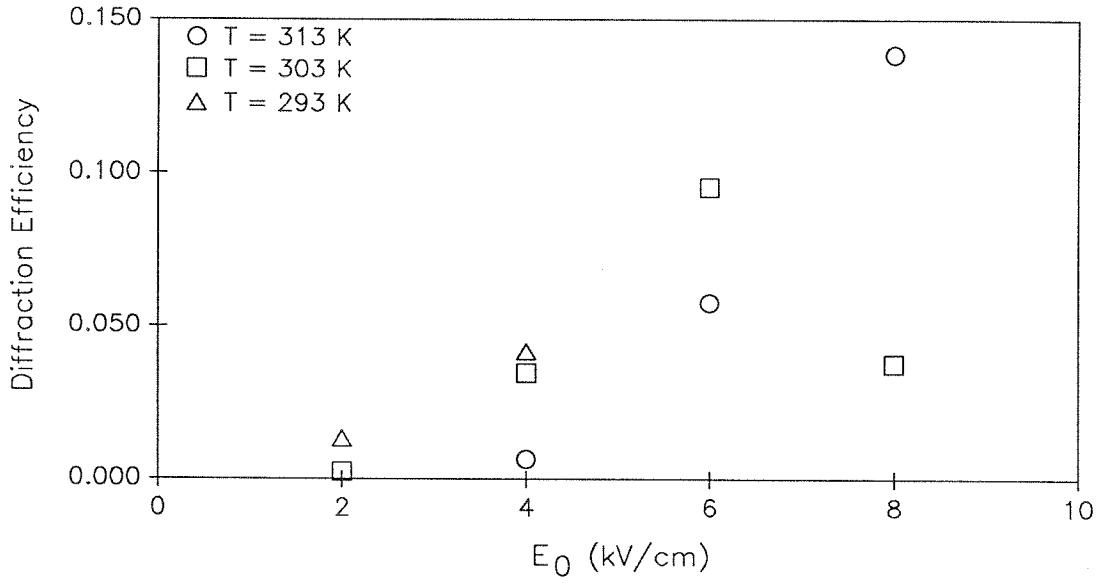

(a)

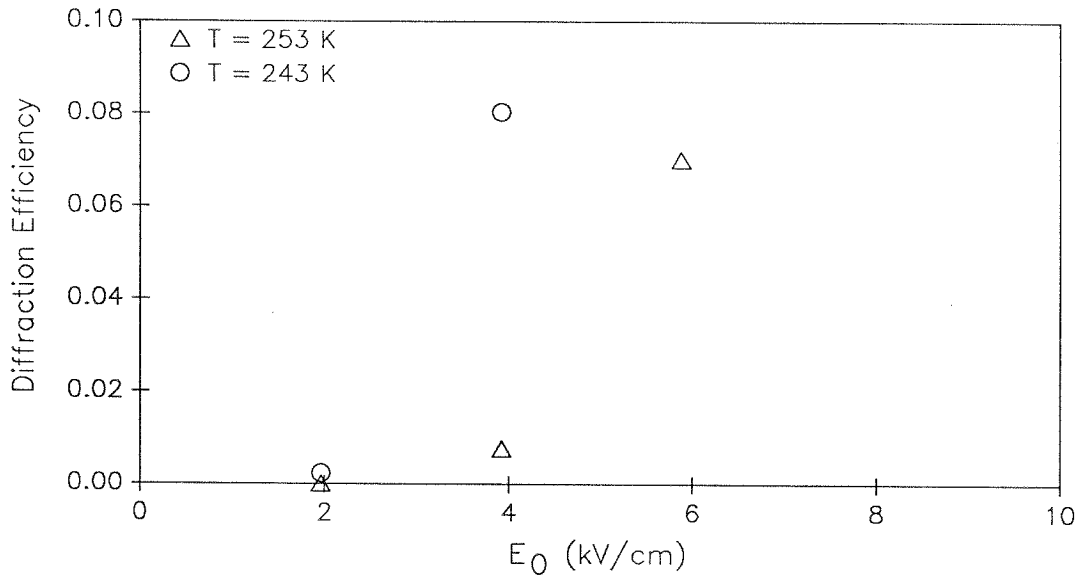

(b)

Fig. 4-6: Diffraction efficiency of the reduced KTN:Cr,Fe crystal – (a) sample A (#0929B), and (b) sample B (#0939B).

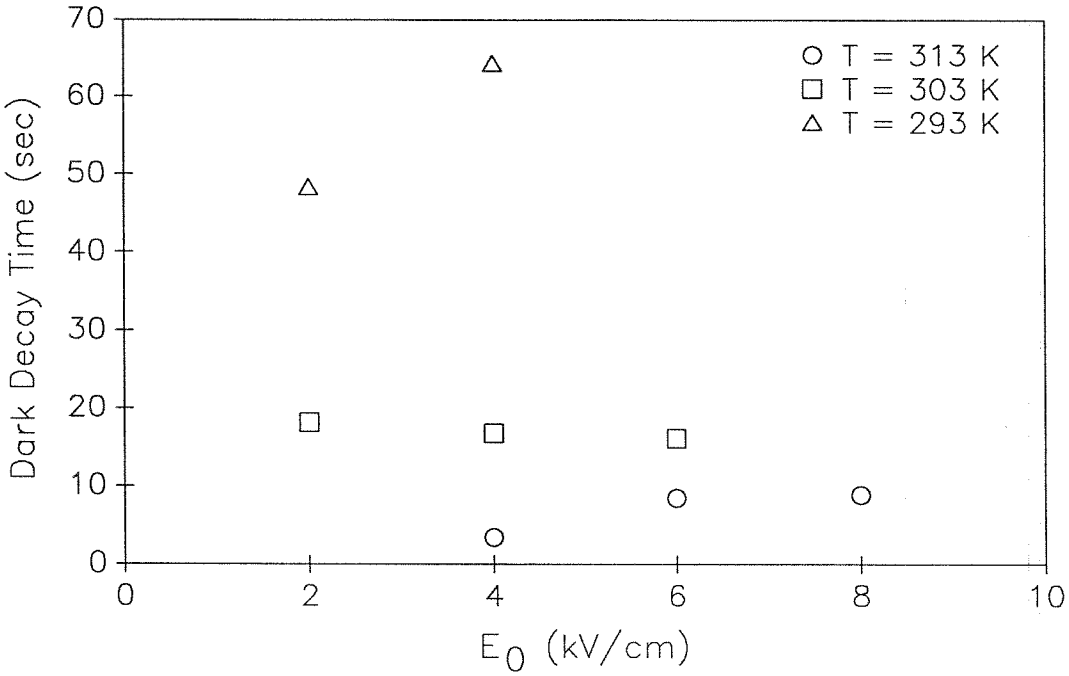

Fig. 4-7: Dark decay time of the reduced KTN:Cr,Fe crystal (sample A, #929A).

4.5. References for Chapter 4

1. A. Agranat, K. Sayano, and A. Yariv, "Photorefractive diffraction gratings in KTN:Cr,Fe in the paraelectric phase using the quadratic electro-optic effect," paper PD-1, OSA Topical Meeting on Photorefractive Materials, Effects, and Devices, Los Angeles, CA (1987).

2. W. Phillips, J.J. Amodei, and D.L. Staebler, "Optical and holographic storage properties of transition metal doped lithium niobate," *RCA Review* **33**, 94-109 (1972).

3. G.A. Rakuljic, A. Yariv, and R.R. Neurgaonkar, "Photorefractive properties of undoped, Ce-doped, and Fe-doped single crystal $Sr_{0.6}Na_{0.4}Nb_2O_6$," *Opt. Eng.* **25**, 1212-1216 (1986).

4. A. Agranat, V. Leyva, K. Sayano, and A. Yariv, "Photorefractive properties of $KTa_{1-x}Nb_xO_3$ in the paraelectric phase," *Proc. SPIE* **1148**, 52-66 (1989).

CHAPTER FIVE

Photorefractive Properties of As-grown SBN

5.1 Introduction

SBN has been the subject of much interest in that it can be photorefractive at room temperature, with high two-beam coupling gain, fast response time, and high optical quality. In addition, it has a number of significant advantages over other materials such as $BaTiO_3$ that has been used in the past for optical wave mixing and phase conjugation, as outlined in previous sections.

One of the principal advantages of SBN over $BaTiO_3$ is in the variability of the electro-optic and photorefractive parameters by changing composition, and the ease in introducing a variety of dopants into its incompletely filled crystal structure.[1] This allows variations and optimization of the optical characteristics to suit a given application. In the following sections of this chapter, the effects of various dopant and composition changes on the photorefractive properties of SBN will be examined and compared. The effects of dark conductivity, incident wavelength, and poling on the photorefractive properties in SBN will also be presented.

5.2. Coupling constant

The photorefractive two-beam coupling constant is an important parameter for determining the magnitude of energy transfer between the signal and pump beams that interact inside the material. High coupling constants are desirable for optical amplifiers, passive phase conjugate mirrors, photorefractively-pumped resonators, optical limiters, and most other applications relying on two-beam coupling. High gain materials also allow thinner samples, with less absorption,

scattering losses, and distortion, to be used for given situations since the two-beam coupling amplification is exponential in Γ, with the amplified beam intensity going as $e^{\Gamma \ell}$.

5.2.1. Experimental procedure

The two-beam coupling constant, or gain coefficient, was measured in the manner described in Sec. 3.4.2 and shown in Fig. 5-1, with both the pump and signal beams being measured simultaneously and in real time through the data acquisition system. The 514.5 nm line of the Ar-ion laser was used, with the beams polarized in the extraordinary direction (parallel to the c axis of the crystal) to take advantage of the large r_{33} electro-optic coefficient of SBN. In most instances the intensity of the pump beam was set at $I_1(0) = 0.25$ W/cm^2, with the signal to pump intensity ratio $I_2(0)/I_1(0) \ll 0.01$ to avoid pump depletion. In some of the higher gain materials such as SBN:60:Ce and SBN:60:Rh, there was considerable depletion of the beam intensities due to beam fanning, or the asymmetric scattering of the incident beam energy due to two-beam coupling amplification of scattered light in the direction of the c axis. However, since this effect had a time scale longer than that of the buildup of the amplified signal beam, it was easily detected and isolated.

The measurements were made by triggering the shutter to illuminate the crystal with both beams simultaneously, and waiting for the gratings to build to the steady state. Since surface reflection and absorption is approximately equal for both beams, their effect on the two-beam coupling constant drops out since the ratio of the beam intensities enters into the equation. At the conclusion of the measurements, the gratings were erased by uniform illumination for a period much longer than the time constant of the material.

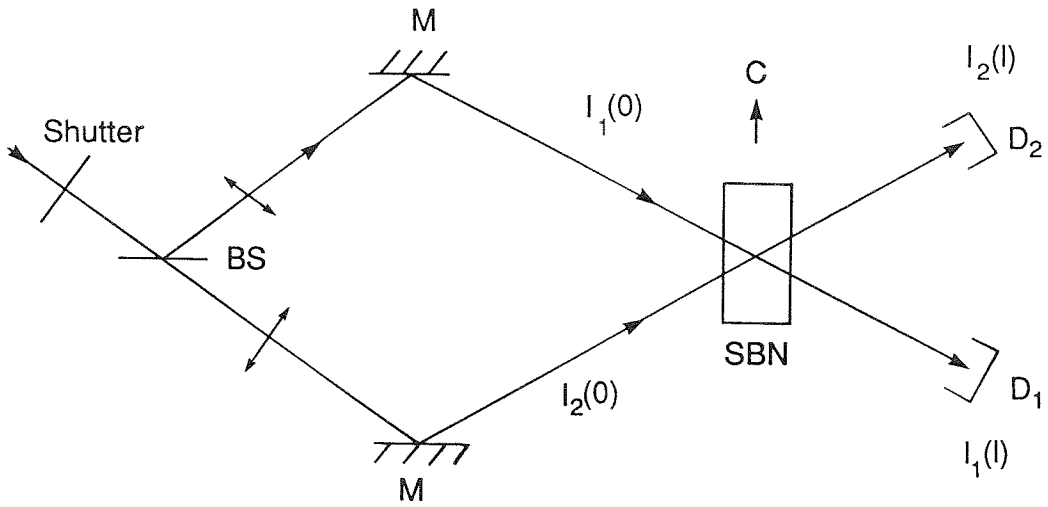

Fig. 5-1: Configuration for the two-beam coupling experiment used to characterize the SBN crystals. The beam polarization was in the same plane as the c axis. $I_1(0) + I_2(0)$ was approximately 0.25 W/cm^2, with $I_2(0) \ll I_1(0)$ to avoid pump depletion.

5.2.2. Effect of Ce and Rh doping

In prior work by G.A. Rakuljic et al., undoped SBN crystals were found to be photorefractive, but the addition of Ce to SBN:60 and SBN:75 was found to dramatically improve the gain and response time of the material. Maximum photorefractive coupling constants of over 10 cm^{-1} have been obtained in a sample of Ce-doped SBN:60 measuring 5 mm on each side, compared to < 3 cm^{-1} for undoped SBN:60 crystals.[2]

The results of two-beam coupling experiments with Rh-doped SBN showed similar characteristics as Ce-doped SBN in that the coupling constant had a value comparable to that of SBN:60:Ce, approximately 10 cm^{-1}.[3] For very long exposures, the fanning loss set in to deplete energy from both beams, which was reflected in the measured coupling constants. However, this effect was easily isolated due to its longer time scale compared to the two-beam coupling amplification of the signal beam because of the lower intensities involved in this secondary effect. The coupling constant of an SBN:60 sample doped with 0.015 wt. % of Rh, along with that of a Ce-doped SBN:60 crystal, is shown in Fig. 5-2.

5.2.3. Effect of Cr doping

The effect of doping SBN:60 and SBN:75 with Cr was also investigated.[4,5] SBN:60 crystals doped with 0.01, 0.016, and 0.03 wt. % of Cr, and SBN:75 with 0.001 wt. % Cr, were successfully grown with sufficient optical quality to make optical measurements. Using the same experimental setup as for the measurements using SBN:60:Rh and SBN:60:Ce, the maximum gain of the as-grown crystals ranged from 3 cm^{-1} with the 0.01 and 0.03 wt. % crystals to 5.7 cm^{-1} for the 0.016 wt. % sample. The SBN:75:Cr crystal, with its larger electro-optic coefficient that resulted in large effects even for smaller values of the space charge field, had

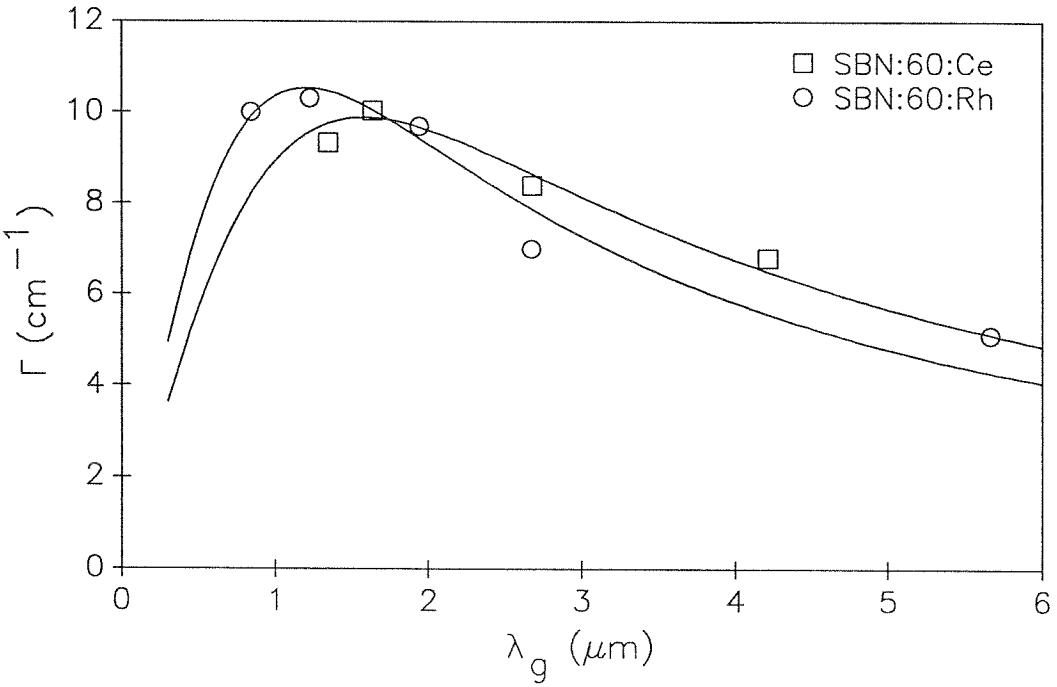

Fig. 5-2: Coupling constant as a function of grating wavelength for Rh-doped SBN:60 and Ce-doped SBN:60. The lines are the best fits of the expected gain coefficient as a function of grating period.

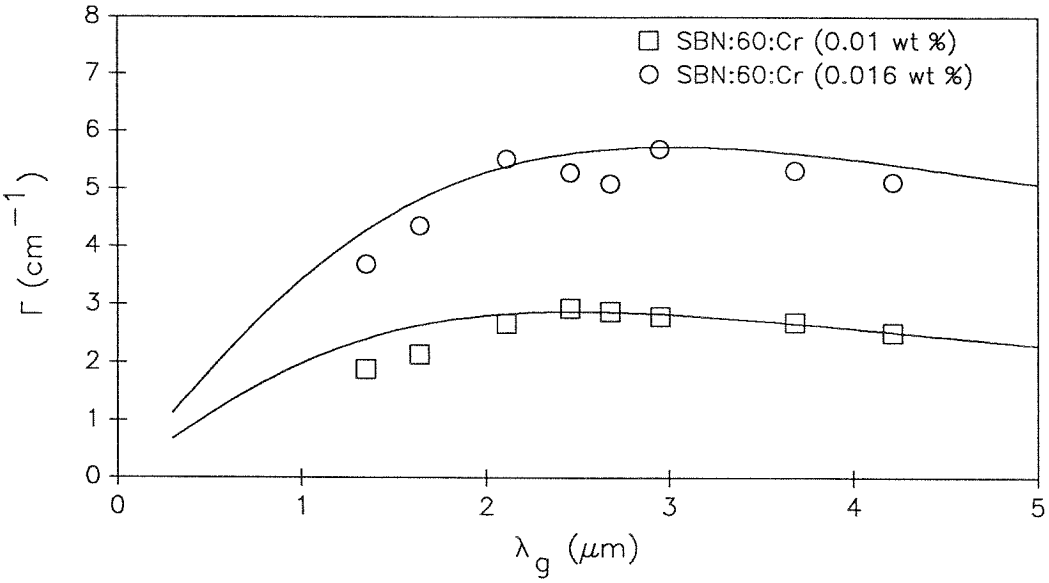

(a)

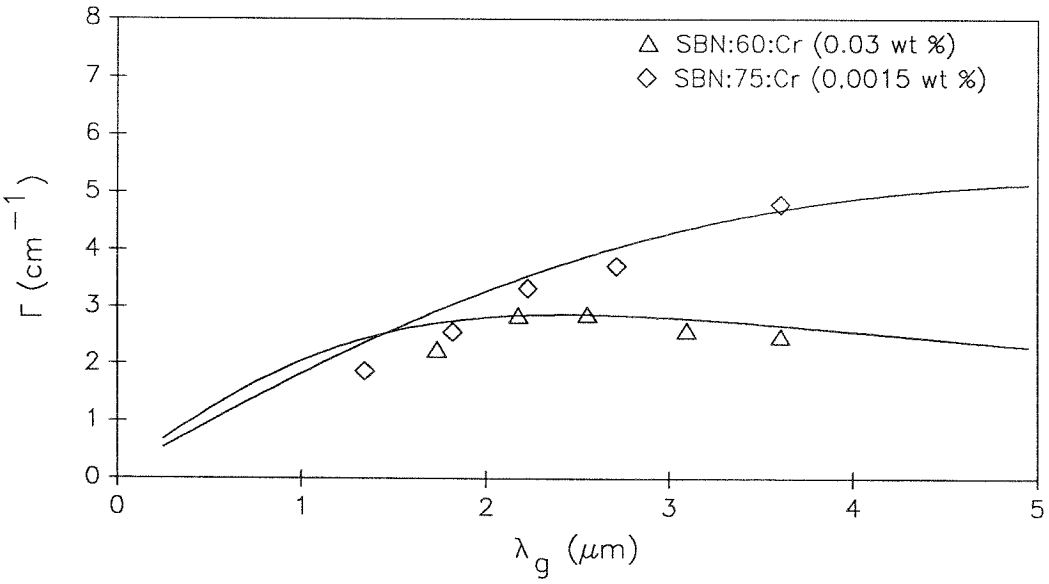

(b)

Fig. 5-3: Coupling constant as a function of grating wavelength for (a) 0.01 and 0.016 wt. % Cr-doped SBN:60, and (b) 0.03 wt. % Cr-doped SBN:60 and 0.0015 wt. % Cr-doped SBN:75.

a maximum coupling constant of almost 5 cm^{-1}. These values measured in Cr-doped SBN were significantly lower than that of Ce- or Rh-doped SBN, but there are numerous situations where moderate gain is sufficient, and where the adverse effects of beam fanning resulting from very large coupling constants are not desired. Figs. 5-3(a) and (b) show the measured coupling constants as a function of grating wavelength for the three SBN:60:Cr and the SBN:75:Cr crystals.

The solid lines through the experimental points in Figs. 5-2, 5-3(a), and 5-3(b) were obtained by fitting using Eqns. (2.11) and (2.12) to the data points assuming no dark conductivity and no external fields. The dielectric constant ϵ was determined using the static capacitance measurement method described in Sec. 3.2.2 and Eqn. (3.1).[6]

5.3. Response time

One of the advantages of SBN or $BaTiO_3$ over some other materials such as $LiNbO_3$ is in their real time response. In $LiNbO_3$, writing and erasing times were measured in minutes. With Ce- or Rh-doped SBN:60, the response time for two-beam coupling gain buildup was on the order of seconds. With Cr-doped SBN, that figure was reduced again by almost another order of magnitude in some of the samples.

The photorefractive response time was determined to be the exponential rise time of the two-beam coupling constant, or

$$\Gamma(t) = \Gamma_{ss}(1 - e^{-t/\tau}), \tag{5.1}$$

where τ is the response time constant. Using the setup shown in Fig. 5-1, the shutter was opened at $t = 0$ and the two detectors simultaneously recorded the buildup in intensity of the amplified signal beam and the attenuated intensity of the pump beam. As in the measurement for the coupling constant, $I_1(0)$ was set at

approximately 0.25 W/cm^2, with $I_2(0)/I_1(0) \ll 0.01$, so the total incident intensity $I_0 = 0.25$ W/cm^2 and pump depletion was negligible. Between measurements, any residual gratings were erased by uniform illumination of the crystal for a period greater than the photorefractive response time.

5.3.1. SBN:60:Ce and SBN:60:Rh

The response times of Ce-doped and 0.015 wt. % Rh-doped SBN:60 are shown in Fig. 5-4 for grating periods from 1.3 to 4.2 μm.[3] Both crystals showed response time constants of approximately 3-4 sec under the experimental conditions used. Since $t_0 \propto 1/I_0$, higher beam intensities will result in proportionally faster response. The response time can also be varied through the wavelength of the incident light, changes in the photoionization cross section, temperature, and external fields, and the results of changing these parameters will be discussed in later sections.

5.3.2. Reduced response time in Cr-doped SBN

Experimental results have demonstrated that Cr-doped SBN crystals have a significant reduction in the time of response compared to Ce- or Rh-doped SBN, with room temperature time constants as short as 0.12 sec.[4,5] The successful growth of crystals with fast response times represents an important step forward in providing improved materials for real-time image processing, optical modulation, and optical signal processing applications where speed of response is desired over large coupling gain.

The measured response time for grating buildup of the as-grown SBN:60:Cr and SBN:75:Cr crystals as a function of grating period are shown in Fig. 5-5. From the plot, it can be seen that the 0.01 and 0.03 wt. % crystals had the fastest response times of 0.16 and 0.12 sec, respectively, while the 0.016 wt. % crystal,

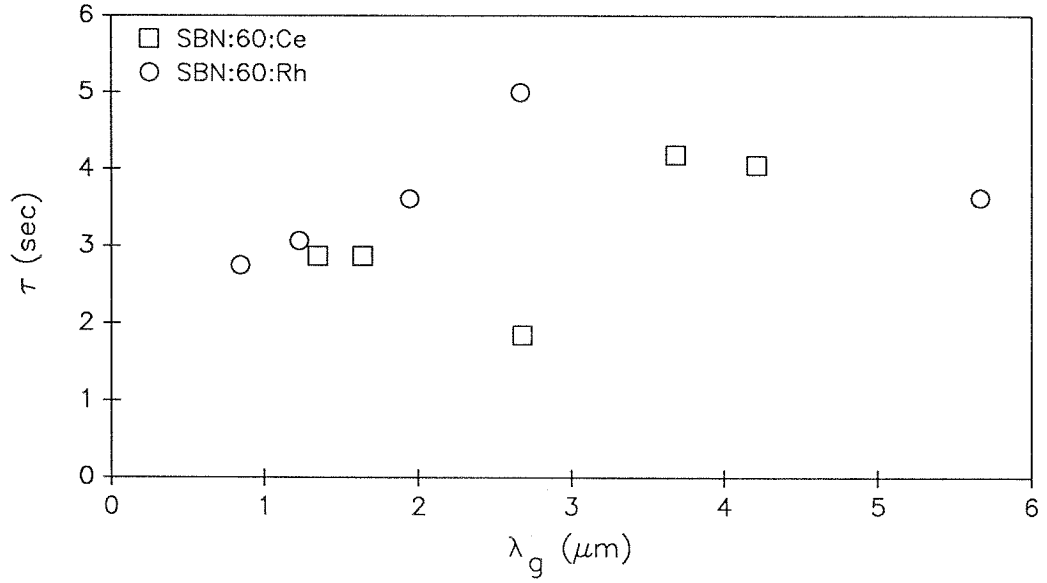

Fig. 5-4: Response time of Ce-doped SBN:60 and Rh-doped SBN:60 as a function of grating period.

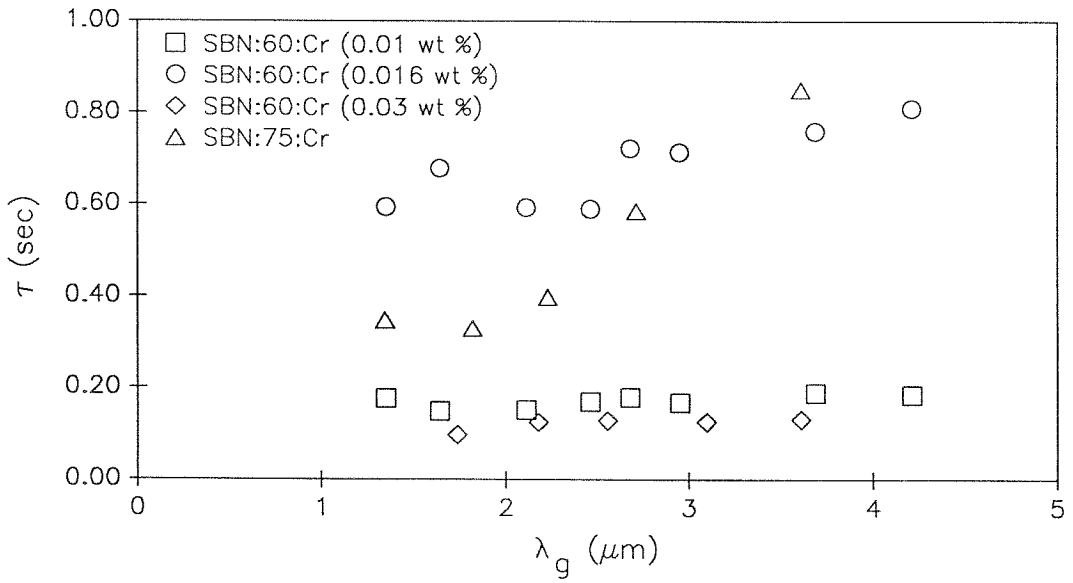

Fig. 5-5: Response time of the three Cr-doped SBN:60 and Cr-doped SBN:75, showing the almost order of magnitude increase in the speed of response over Ce or Rh doping.

although having a higher gain than the other Cr-doped samples, had a slightly slower response time of 0.59 sec. The response time of the SBN:75:Cr, as shown in the figure, had a value ranging from approximately 0.4 to 0.85 sec, depending on the grating period.

5.3.3. Comparison of dopant types/concentrations

Both Ce-doped SBN:60 and Rh-doped SBN:60 had high two-beam coupling gain, which is the result of large steady-state index changes, which were approximately 5×10^{-4} for both. This would make them useful for high efficiency devices, but their slow response time (on the order of 1 sec) poses a significant drawback for real-time image processing and similar applications requiring faster-responding materials.

Significant increases in the response time of up to an order of magnitude over Ce-doped or Rh-doped SBN were obtained through Cr doping. Response times ranging from 0.6 sec for the 0.016 wt. % Cr-doped crystal to 0.12 sec for the 0.03 wt. % Cr-doped sample were obtained, with gain coefficients of about 3 cm^{-1} at their optimum grating periods.

Table 5-1 compares the figures of merit of the various SBN crystals, including the photorefractive sensitivity which was defined in Sec. 3.4.4. The 0.03 wt. % Cr-doped crystal, which had the highest dopant concentration of the SBN crystals, had the largest photorefractive sensitivity, on the order of 2×10^{-3} cm/J, which was an order of magnitude larger than that of the Ce-doped SBN crystal. Because of their slow response, the Ce-doped or Rh-doped crystals, although having large photorefractive gain coefficients, showed a significantly lower sensitivity than the Cr doped crystals.

Another interesting point to note is that the KTN:Cr,Fe crystals, the results

Material	Γ_{ss} (cm^{-1})	τ (sec)	$n_{1,ss}$ (10^{-4})	S (cm^3/J)
SBN:60:Cr (0.01)	2.93	0.16	1.51	1.43×10^{-3}
SBN:60:Cr (0.016)	5.28	0.59	2.72	7.16×10^{-4}
SBN:60:Cr (0.03)	2.90	0.12	1.00	2.29×10^{-3}
SBN:75:Cr	4.80	0.85*	2.47	3.99×10^{-4}
SBN:60:Ce	10.04	3.27	5.17	2.82×10^{-4}
SBN:60:Ce,Ca	10.00	0.86	5.15	7.45×10^{-4}
SBN:60:Rh	10.30	1.78	5.30	9.64×10^{-4}
SBN:60:Cr (0.016)†	1.63	5.53	0.84	1.01×10^{-5}
KTN:Cr,Fe	– –	– –	0.20	3.61×10^{-6}

*At $\lambda_g = 3.61$ μm

†At $\lambda = 632.8$ nm

Table 5-1: Figures of merit used to compare the photorefractive effects of SBN:60:Cr (0.01, 0.016, and 0.03 wt. %), SBN:75:Cr, double doped SBN:60:Ce,Ca, SBN:60:Ce, SBN:60:Rh and KTN:Cr,Fe. The 0.03 wt. % Cr-doped SBN:60 had the highest photorefractive sensitivity, while SBN:60:Rh had the largest steady-state index change. As expected, the SBN:60:Cr had lower sensitivity at 632.8 nm compared to 514.5 nm.

of which were presented in Chapter 4, showed a much lower photorefractive sensitivity of approximately 4×10^{-6} cm/J, with a steady state index change of 2×10^{-5}. However, the exposure time of 5 sec was probably considerably longer than the minimum, so saturation effects were undoubtedly affecting the calculated value of S. Using a shorter exposure time will probably result in a higher figure for the sensitivity.

5.4. Poling SBN crystals

The SBN:60 and SBN:75 crystals used in this work were all poled into a single domain by cooling through their cubic to ferroelectric phase transition temperatures with an applied field. This serves to align the crystal domains in order to realize the large electro-optic effects cited in Chapter 3 and in Table 3-1. In $BaTiO_3$, the 90° domains make them easy to see when the crystal is depoled. SBN has 180° comains, which make them less visible.

In order to determine the minimum threshold for poling and any effect of poling voltage on the magnitude of the photorefractive effect, an SBN:60:Rh crystal was used for two-beam coupling measurements after depoling and repeating the poling process for various voltages. The crystals were heated to about 390 K in an oil bath and allowed to cool at about 0.5° per minute through the phase transition with an applied field of E_p. Each time, the polarity of the applied field on the crystal was switched to ensure that no residual poling remained. As shown in Fig. 5-6, the measured two-beam coupling constant appears independent of E_p from 0.5 to 10 kV/cm. The crystals obtained from Rockwell were all poled at approximately 8 kV/cm, so the results from this experiment also indicate that lower voltages can be used with little effect on the optical characteristics of the crystal.

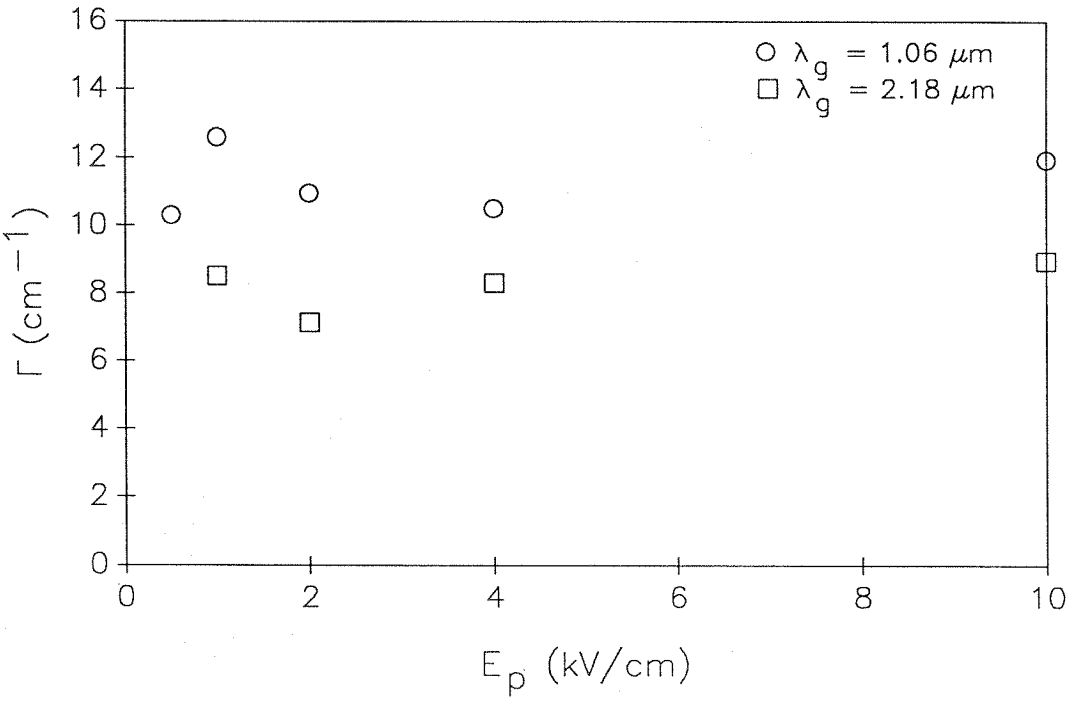

Fig. 5-6: Two-beam coupling constant of Rh-doped SBN:60 as a function of poling voltage from 0.5 to 10 kV/cm.

5.5. Wavelength dependence of the photorefractive effect

All of the preceding experiments, as well as most of the previous work in photorefractive materials, have concentrated on the visible spectrum, specifically the 514.5 nm Ar-ion laser wavelength. However, there are numerous applications where sources with other wavelengths are more suited, especially those using lower photonic energy wavelength He-Ne lasers at 632.8 nm and semiconductor lasers at approximately 840 nm and longer wavelengths.[7]

The photorefractive measurements were repeated using the 0.016 wt. % Cr-doped SBN:60 crystal as the two-beam coupling medium for the 632.8 nm output of a He-Ne laser with total intensity of approximately 0.75 W/cm^2.[5] Photorefractive gain and response time were measured over a temperature range of 253 K $\leq T \leq$ 313 K at $\lambda_g = 2.46$ μm. Figures 5-7 and 5-8 show the gain and response time, respectively, of the Cr-doped SBN:60 sample at both 632.8 and 514.5 nm. Because of the lower absorption and fewer ionizable donors available at the longer wavelength, the gain was predictably lower, and with a longer response time, than comparable measurements using shorter wavelength (and therefore higher energy) sources. Measurable results were not obtainable at 840 nm using this same crystal, although the crystal absorption spectrum shows a broad-band absorption region in the red to infra-red range, centered around 650 nm.

The steady state index change at 632.8 nm and $T = 293$ K, reflected in the two-beam coupling constant, was about $\frac{1}{3}$ of its value when measured using 514.5 nm light. However, with its slower response time, the photorefractive sensitivity at the He-Ne laser wavelength was 10^{-5} cm/J, which indicates an almost 2 orders of magnitude drop from that at the Ar-ion line.

Experiments have also been carried out to determine whether SBN is photorefractive at 840 nm and 1.06 μm. Ce-doped SBN:60 using optically inactive Ca

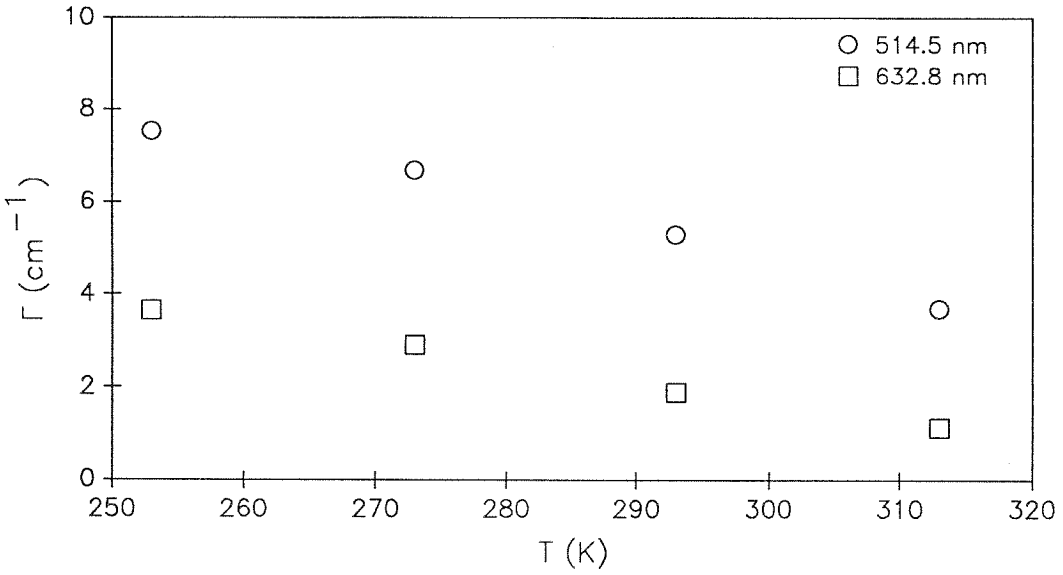

Fig. 5-7: Photorefractive two-beam coupling constant of Cr-doped SBN:60 at 514.5 and 632.8 nm incident wavelength with $\lambda_g = 2.46$ μm.

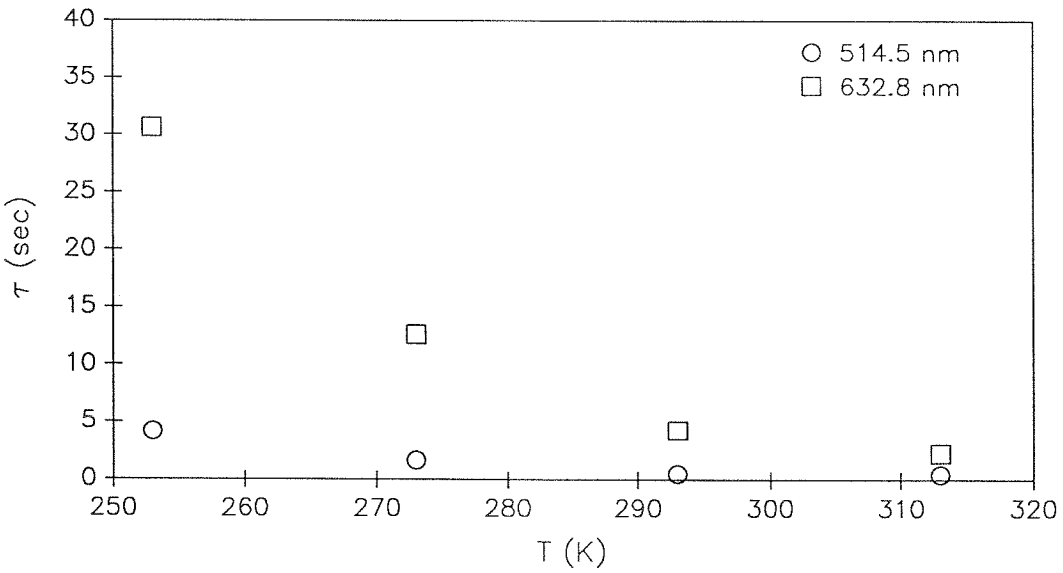

Fig. 5-8: Response time of the Cr-doped SBN:60 crystal at the two incident wavelengths.

to force Ce into the 9-fold sites has been found to have significantly improved sensitivity at the 840 nm semiconductor laser wavelength over Ce-doped SBN:60 with Ce in the 12- or 15-fold sites.[7] However, Cr-doped SBN did not show a measurable effect at 840 nm. Although $BaTiO_3$ has exhibited the photorefractive effect at wavelengths down to 1.06 μm, no effect at that wavelength was observed in the currently available line of SBN crystals.

5.6. Dark conductivity effects

Certain SBN crystals have previously been observed to exhibit increased photorefractive coupling gain as the crystal temperature was lowered below room temperature and away from its cubic to ferroelectric phase transition near 345 K. This effect was observed and reported in Ce- and Ca- double doped SBN:60 over the temperature range of 243 to 313 K, in Cr-doped semi-insulating bulk GaAs from 280 to 400 K, and in 0.01 wt. % Cr-doped SBN:60.[5,8–10] Although the effects were much smaller, this temperature dependence has also been observed in Ce-doped SBN:60 and Rh-doped SBN:60.

5.6.1. Temperature dependence of photorefractive gain

The equations governing the photorefractive coupling constant have been derived from the band transport model in Chapter 2 for the general case, with some temperature-dependent function $\beta(T)$ representing the effects of thermally excited sites, or dark conductivity. Without accounting for the dark conductivity, the expected temperature dependence of the gain should be $d\Gamma/dT > 0$ since the dielectric constant increases sharply near the phase transition temperature, as shown in Fig. 5-9 for Cr-doped SBN:60. The two-beam coupling constant should

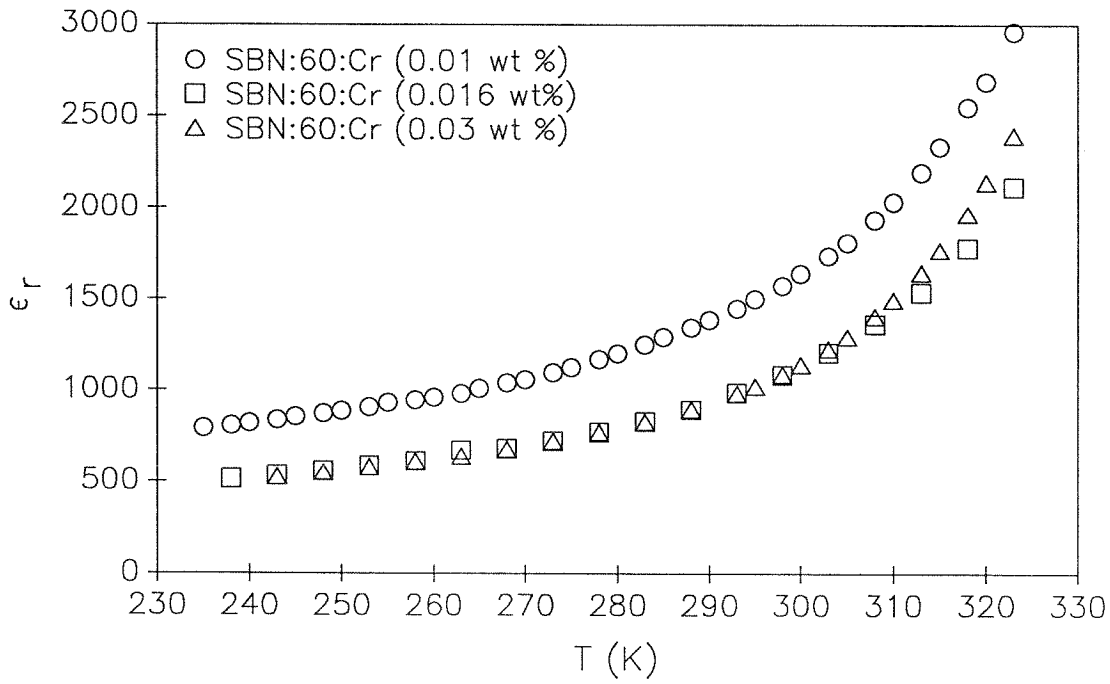

Fig. 5-9: Increase in the dielectric constant (and therefore the effective electro-optic coefficient) near the phase transition for the various Cr-doped SBN:60 crystals.

have the following temperature dependence in this case:

$$\Gamma \propto \frac{T}{T + B/\epsilon} . \tag{5.2}$$

The experimentally measured steady-state coupling constant for the Ce,Ca-, Rh-, and Cr-doped SBN:60 and Cr-doped SBN:75 crystals as a function of temperature at their optimum grating periods are shown in Fig. 5-10(a) and (b). Although the decrease in gain with respect to increases in temperature was small for the Ce- and Ca-doped SBN:60 and Rh-doped SBN:60, there was a considerable drop in gain in the case of the Cr-doped sample as it was heated. Therefore, there must be a competing phenomenon with a negative temperature dependence near the phase transition to explain the observed negative temperature dependence of gain over this range, this being the dark conductivity.

From Sec. 2.5.1, the dark conductivity of a doped semiconductor arising from thermally excited sites, which serves as an approximate model for these types of materials, is given by Eqn. (2.33),[11]

$$\beta(T) = \beta_0 T^{\frac{3}{2}} e^{E_t/k_B T} . \tag{5.3}$$

Figure 5-11 shows the temperature dependence of the dark conductivity factor, $[1 + (h\nu/sI_0)\beta(T)]^{-1}$, which is responsible for reducing the photorefractive gain in Eqn. (2.11) and response time in Eqn. (2.16), for $E_t = 0.02$ meV and $h\nu\beta_0/sI_0 = 60$.

The theoretical photorefractive gain as a function of all temperature dependent quantities can be given by

$$\Gamma = \Gamma_0 \frac{T}{T + B/\epsilon_r} \frac{1}{1 + AT^{3/2}\exp(-E_t/k_B T)} , \tag{5.4}$$

where $A = (h\nu/sI_0)\beta_0$ and $B = e^2 N_A/\epsilon_0 k_B K^2 = 4.49 \times 10^5$, for three different values of A representing low to high dark conductivity effects. Eqn. (5.4) was fitted

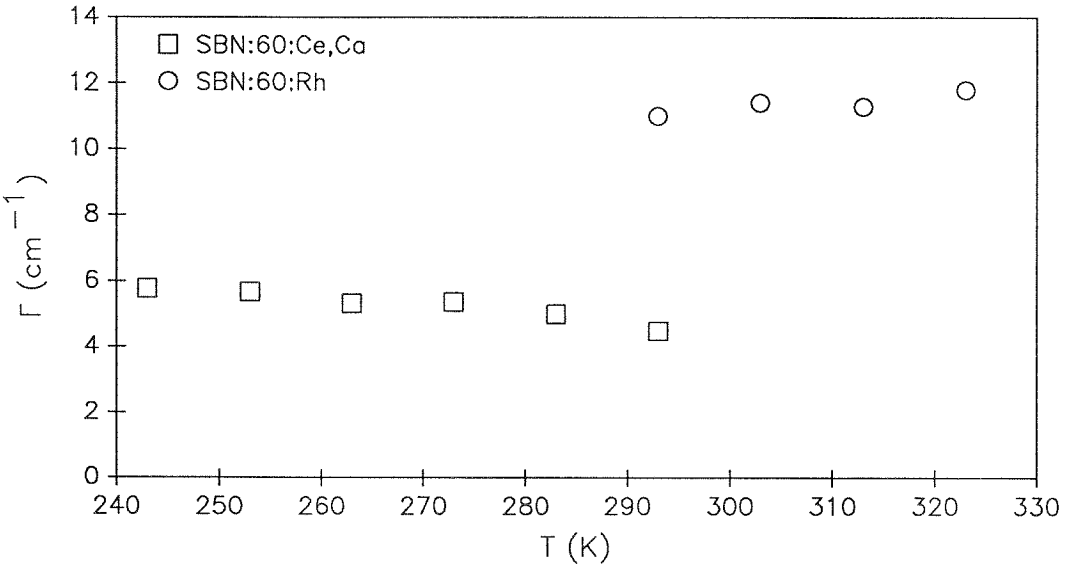

(a)

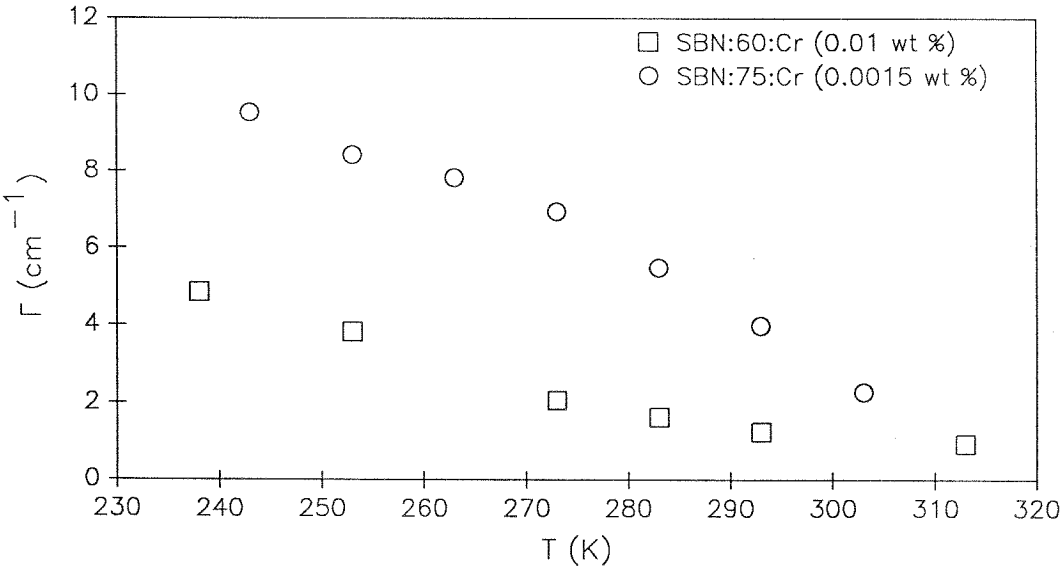

(b)

Fig. 5-10: Coupling constant as a function of temperature for (a) Ce- and Ca-doped SBN:60 and Rh-doped SBN:60, and (b) 0.01 wt. % Cr-doped SBN:60 and 0.0015 wt. % Cr-doped SBN:75.

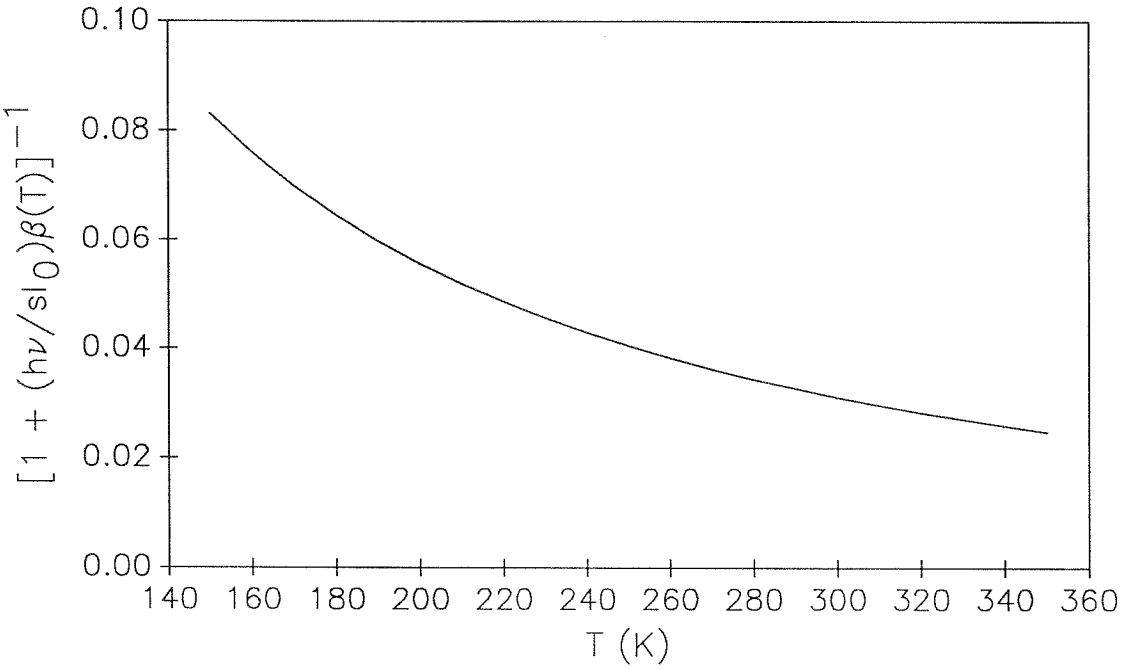

Fig. 5-11: Temperature dependence of the dark conductivity factor in the equations for gain and response time, $[1 + (h\nu/sI_0)\beta(T)]^{-1}$, from 150 to 350 K for $E_t = 0.02$ meV and $h\nu/sI_0) = 60$.

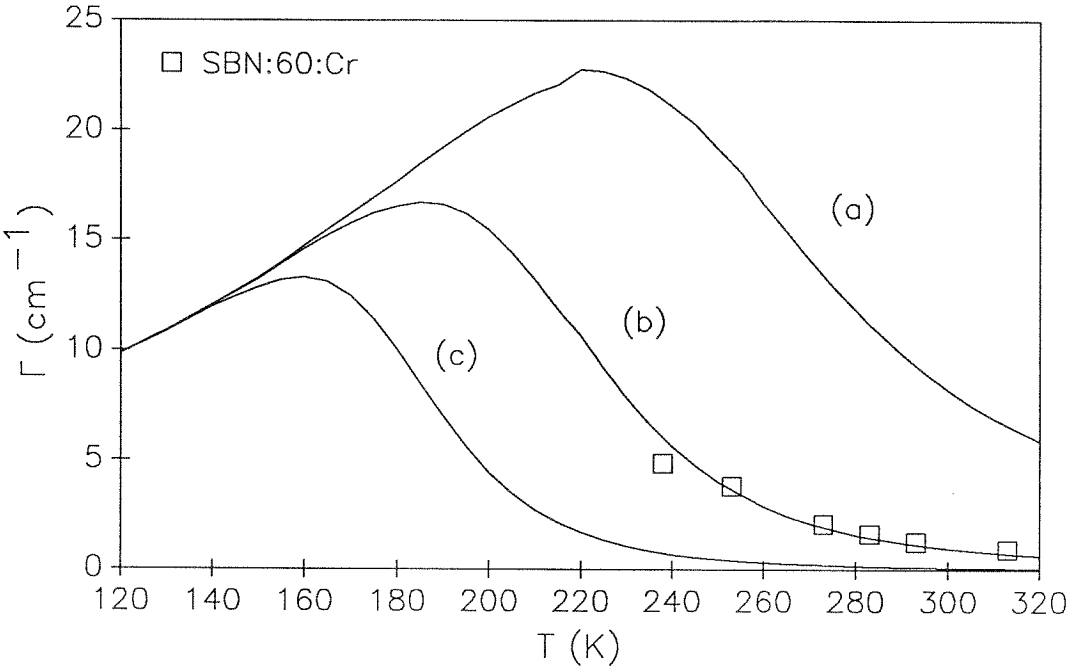

Fig. 5-12: Theoretical temperature dependence of the gain for different dark conductivities. The experimental points in the plot were obtained using the 0.01 wt. % Cr-doped SBN:60 crystal. The three cases illustrated are: (a) low dark conductivity, $A = (h\nu/sI_0)\beta_0 = 6$; (b) best fit of the experimental points, $A = 60$; and (c) high dark conductivity, $A = 600$.

to the experimental points obtained from Cr-doped SBN:60 and extended to lower temperatues beyond what was experimentally measured. As expected, Fig. 5-12 shows the gain increasing to a peak at some optimum temperature T_0, which itself is dependent on the strength of the dark conductivity effect. It can be inferred from the figure that for $T < T_0$ the original Kukhtarev's equations hold, while for $T > T_0$ the additional factor that takes dark conductivity into account becomes significant. Also, as the dark conductivity decreases, the optimum temperature T_0 increases, so for low dark conductivity materials, the original equations should still be valid at room temperature.

The presense of significant dark conductivity can be determined by measuring the coupling constant for low total intensity I_0. From Eqn. (2.11),

$$\Gamma \propto \frac{1}{1 + I_{th}/I_0} \tag{5.5}$$

where $I_{th} = h\nu\beta/s$. If dark conductivity were present, it would follow that Γ should be intensity dependent at low total intensity and constant at high intensity, as observed by M.D. Ewbank et al. for some Ce-doped SBN:60 crystals.[12] The effect in Ce-doped SBN, however, was much smaller than that of Cr-doped SBN. Fig. 5-13 shows the experimentally measured dependence of gain on total intensity in the 0.01 wt. % Cr-doped SBN:60 crystal at $T = 293$ K and $T = 313$ K. The solid lines represent the best fit based on Eqn. (5.5). Note that since I_{th} is a function of temperature through its dark conductivity, this nonlinear effect has potential applications in optical thresholding using temperature as a means of controlling the thresholding level.

5.6.2. Response time and dark decay time

Although cooling SBN:60:Cr has resulted in a significant increase in the coupling constant, the response time became bigger at lower temperatures.

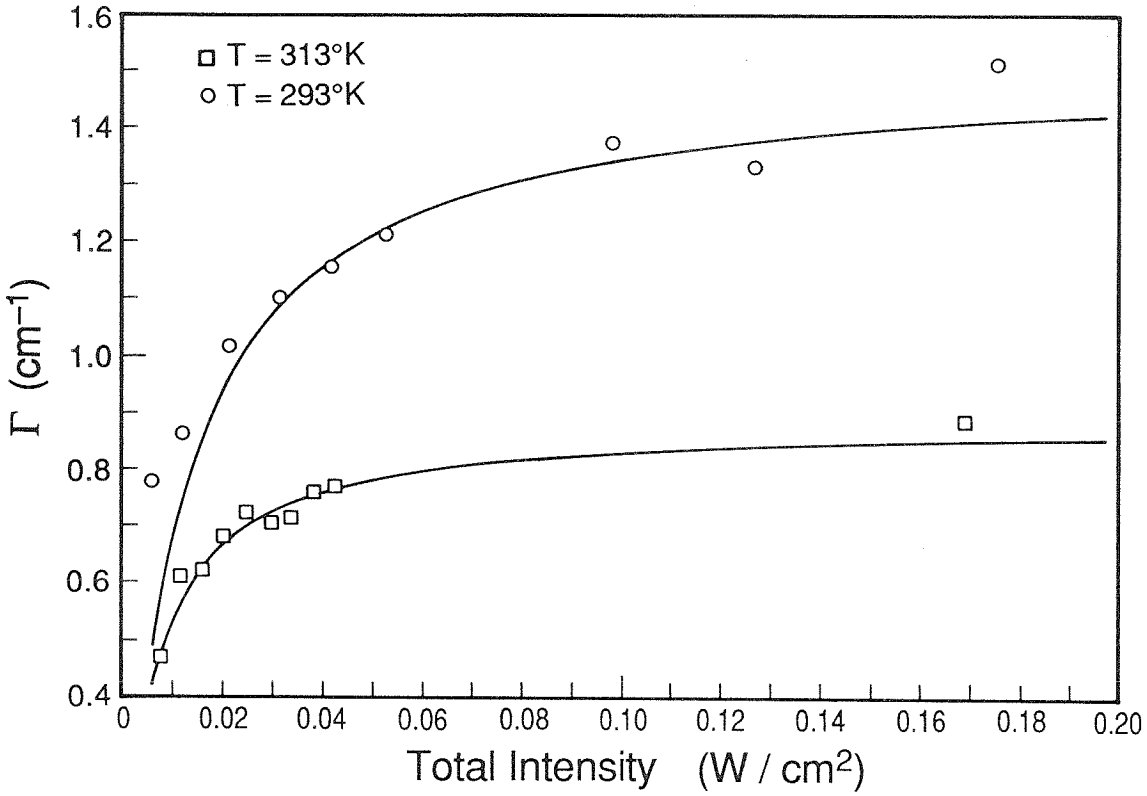

Fig. 5-13: Gain as a function of total intensity at low intensity, showing significant intensity dependence of gain and therefore dark conductivity in the crystal, for $T = 293$ and 313 K.

Conversely, faster response times were obtained at a cost of lower gain when these crystals were heated, and this method has indeed been used in the past to speed up the response times of $BaTiO_3$ and other materials.[13,14]

As in the equation for the coupling constant, the dark conductivity enters as a $(1 + h\nu\beta/sI_0)$ factor into the fundamental limit response time t_0 as shown in Eqn. (2.16). However, obtaining a theoretical value for the response time is more complicated than for gain because of additional temperature dependent parameters whose functional dependence on temperature is not well known. By approximating parameters such as μ and γ as constants in Eqn. (2.16), it can be seen that the increased dark conductivity at higher temperatures will result in faster response. The experimental results of response time (for grating buildup) of Rh-doped SBN:60 and Cr-doped SBN:60 and SBN:75 crystals are shown in Figs. 5-14(a) and (b). Rh-doped SBN, which has a low dark conductivity, showed little change in τ with temperature, while the Cr-doped SBN crystals had response times which ranged from 10.2 sec at 238 K to 0.44 sec at 313 K for SBN:60 and 4 sec at 243 K to 0.44 sec at 303 K for SBN:75.

A comparison among the various dopants in its effects on dark conductivity can be made from the dark decay rates of the various crystals. For storage applications, low dark conductivity, long dark storage materials such as Ce-doped or Rh-doped SBN will be desired. On the other hand, real-time devices not requiring high efficiency or high coupling, or where the fanning effect arising from high gain is not desired, can make use of higher dark conductivity, fast dark decay materials such as Cr-doped SBN. Fig. 5-15 shows the dark decay times, measured in real time with a low intensity He-Ne probe beam Bragg matched to the photorefractive gratings written using an Ar-ion laser with total intensity 0.5 W/cm^2, showing the change in dark conductivity with temperature.

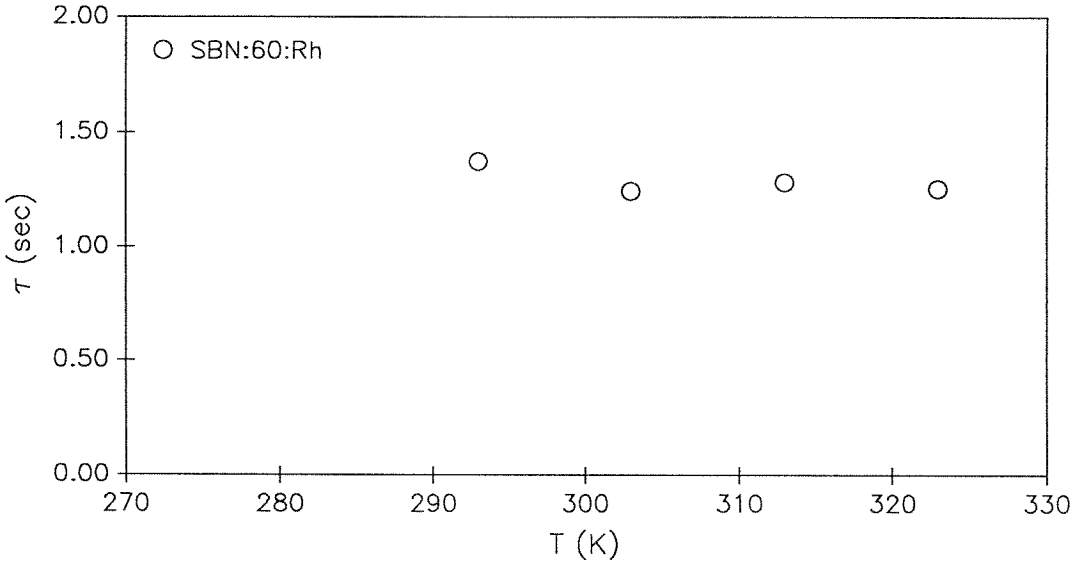

(a)

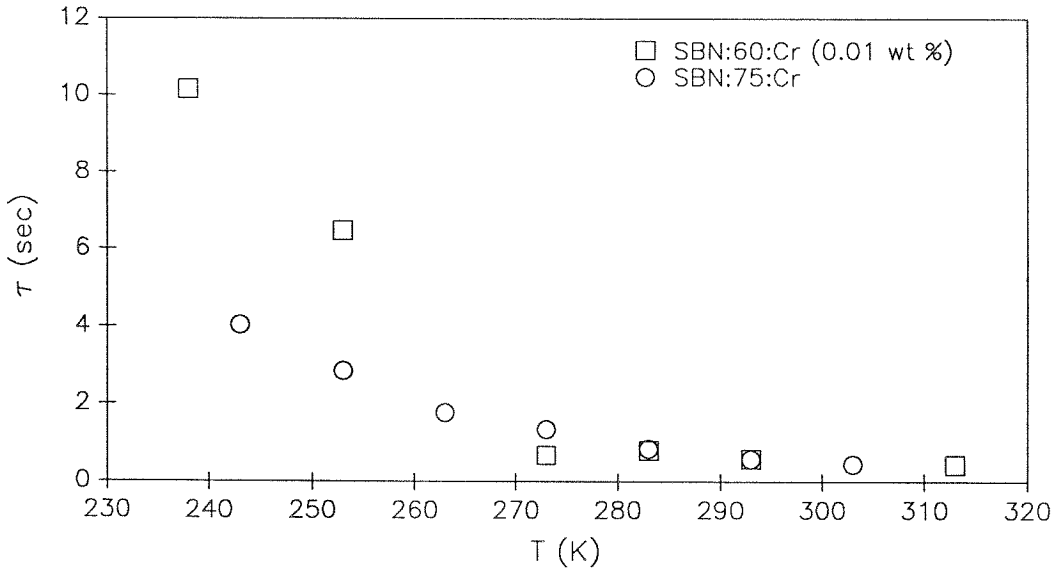

(b)

Fig. 5-14: Experimental response time for grating buildup as a function of temperature in (a) Rh-doped SBN:60, and (b) Cr-doped SBN:60 and SBN:75.

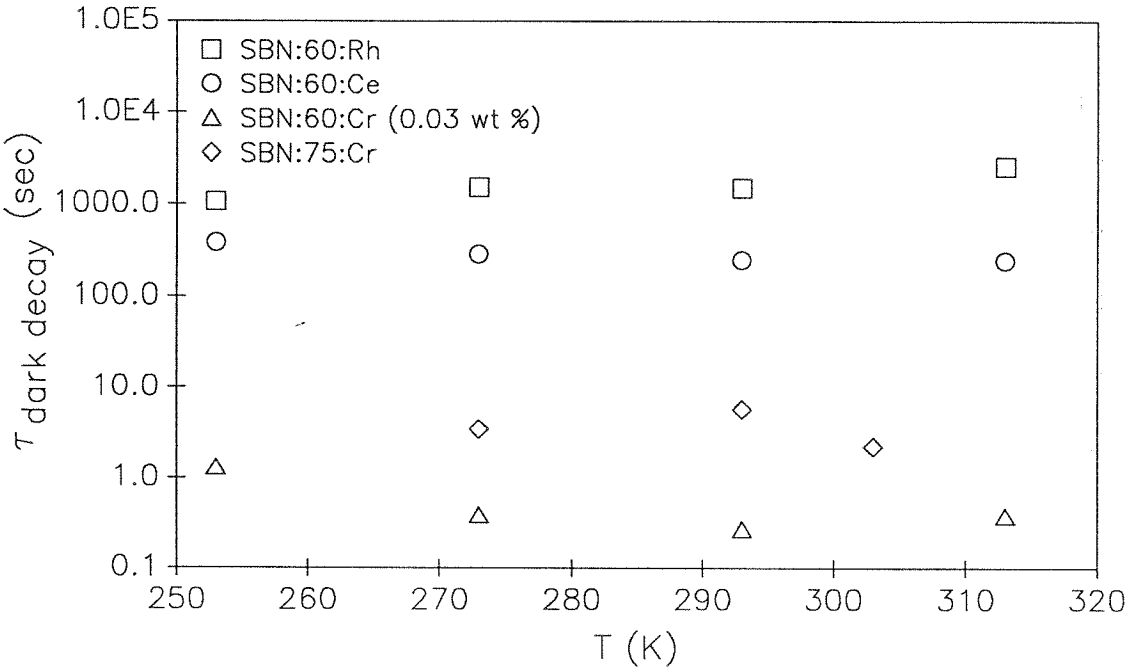

Fig. 5-15: Dark decay times for various SBN:60 and SBN:75 crystals, measured using a low intensity, vertically polarized He-Ne laser Bragg-matched to the photorefractive gratings, for $I_0 = 0.5$ W/cm^2 and $m = 1$.

5.7. Summary

Optical quality Cr-doped SBN:60 and SBN:75 and Rh-doped SBN:60 have been grown and characterized. Cr-doping resulted in significant reduction of the response times of these materials. The temperature dependence of the photorefractive properties were investigated, with the result being significant increases in gain and response time as the Cr-doped crystals were cooled. A model was proposed that incorporated dark conductivity in the band transport equations to account for the observed temperature dependence.

5.8. References for Chapter 5

1. R.R. Neurgaonkar and W.K. Cory, "Progress in photorefractive tungsten bronze crystals," *J. Opt. Soc. Am. B* **3**, 274-282 (1986).

2. G.A. Rakuljic, A. Yariv, and R.R. Neurgaonkar, "Photorefractive properties of undoped, Ce-doped, and Fe-doped single crystal $Sr_{0.6}Ba_{0.4}Nb_2O_6$," *Opt. Eng.* **25**, 1212-1216 (1986).

3. K. Sayano, A. Yariv, and R.R. Neurgaonkar, "Order of magnitude reduction of the photorefractive response time in rhodium-doped $Sr_{0.6}Ba_{0.4}Nb_2O_6$ with a dc electric field," *Opt. Lett.* **15**, 9-11 (1990).

4. K. Sayano, A. Yariv, and R.R. Neurgaonkar, "Photorefractive gain and response time of Cr-doped strontium barium niobate," *Appl. Phys. Lett.* **55**, 328-330 (1989).

5. K. Sayano, A. Yariv, and R.R. Neurgaonkar, "Photorefractive properties of Cr-doped single crystal strontium barium niobate," *Proc. SPIE* **1148**, 7-11 (1989).

6. A. Agranat, V. Leyva, and A. Yariv, "Voltage-controlled photorefractive effect in paraelectric $KTa_{1-x}Nb_xO_3$:Cu,V," *Opt. Lett.* **14**, 1017-1019 (1989).

7. G.A. Rakuljic, K. Sayano, A. Agranat, A. Yariv, and R.R. Neurgaonkar, "Photorefractive properties of Ce- and Ca-doped $Sr_{0.6}Ba_{0.4}Nb_2O_6$," *Appl. Phys. Lett.* **53**, 1465-1467 (1988).

8. L.J. Cheng and A. Partovi, "Temperature and intensity dependence of photorefractive effect in GaAs," *Appl. Phys. Lett.* **49**, 1456-1458 (1986).

9. Y. Tomita, *Modal dispersion of intormation and wave mixing in photorefractive crystals for information retrieval, processing, and sensing*, Ph.D. thesis (1989).

10. K. Sayano, G.A. Rakuljic, A. Agranat, A. Yariv, and R.R. Neurgaonkar, "Photorefractive dark conductivity in Cr-doped strontium barium niobate," *Opt. Lett.* **14**, 459-461 (1989).

11. S.M. Sze, *Semiconductor Devices – Physics and Technology*, (New York: Wiley, 1985).

12. M.D. Ewbank, R.R. Neurgaonkar, W.K. Cory, and J. Feinberg, "Photorefractive properties of strontium-barium niobate," *J. Appl. Phys.* **62**, 374-380 (1987).

13. D. Rytz, M.B. Klein, R.A. Mullen, R.N. Schwartz, G.C. Valley, and B.A. Wechsler, "High-efficiency fast response in photorefractive $BaTiO_3$ at 120° C," *Appl. Phys. Lett.* **52**, 1759-1761 (1988).

14. D. Rytz, B.A. Wechsler, R.N. Schwartz, C.C. Nelson, C.D. Brandle, A.J. Valentino, and G.W. Berkstresser, "Temperature dependence of photorefractive properties of strontium-barium niobate ($Sr_{0.6}Ba_{0.4}Nb_2O_6$)," *J. Appl. Phys.* **66**, 1920-1924 (1989).

CHAPTER SIX

Enhancement of the Photorefractive Properties of SBN

6.1. Introduction

One of the major thrusts of photorefractive materials research has been in enhancing the photorefractive effect in materials, that is, increasing the two-beam coupling gain as well as speeding up the response of the crystal. Depending on the application, either higher gain or faster response time requirements may be the dominant goal. For example, optical amplifiers, phase conjugate mirrors, photorefractively-pumped resonators, and optical limiters demand high gain coefficients, while in signal processing applications faster response times are desired but moderate gain often suffices. A number of schemes which attempt to improve the photorefractive properties of SBN along these lines were investigated and are described in the following sections.

6.2. Optimized grating spacing

As can be observed from the data presented in Chapter 5, the two-beam coupling gain coefficient is a function of the grating period. For small grating periods, the coupling constant is linear with the grating wavelength, since the availability of trapping sites becomes the limiting factor. For large grating periods, the diffusion field becomes significant, and the gain Γ becomes inversely proportional to the grating wavelength.

6.2.1. Dependence on trap density

In photorefractive materials, the trap density $N_{A,C}^{-}$ ($= N_A$) first introduced in Chapter 2 plays an important role in determining the grating wavelength

corresponding to the optimum gain coefficient. The two competing effects of drift and charge separation result in the gain coefficient attaining a maximum at some optimal grating wavelength.

This phenomenon can be seen in the equations for the space charge field, Eqn. (2.11) and (2.12). The optimized grating wavelength corresponds to the Debye screening wavelength of the material. This dependence arises from the characteristic fields E_N and E_d, which are functions of the grating period λ_g through the grating wavenumber, in Eqn. (2.11). From Eqn. (2.11), the photorefractive two-beam coupling constant is given by

$$\begin{aligned}\Gamma \propto & \frac{E_N E_d}{E_N + E_d} \\ = & \frac{e k_B T K N_A (1 - N_A/N_D)}{e^2 N_A (1 - N_A/N_D) + \epsilon k_B T K^2}\end{aligned} \tag{6.1}$$

where N_A is the trap density, N_D is the donor density, and $K = 2\pi/\lambda_g$ is the grating wavenumber, for the case where there is no applied field. Note that for $N_A \ll N_D$, N_A/N_D is small, so E_N can be approximated by $eN_A/\epsilon K$. The relative maximum of the photorefractive gain as a function of grating wavenumber then gives the optimum grating period:

$$\lambda_{g,max} = \frac{2\pi}{e}\sqrt{\frac{\epsilon k_B T}{N_A(1 - N_A/N_D)}}\,. \tag{6.2}$$

Eqn. (6.2) can also be used to determine the trap density of a given sample from the peak of the experimentally measured values of the gain coefficient over a range of grating wavelengths.

At the optimum grating period obtained in Eqn. (6.2), the two characteristic fields E_N and E_d are equal and given by

$$E_N = E_d = \sqrt{\frac{k_B T N_A}{\epsilon}\left(1 - \frac{N_A}{N_D}\right)}\,, \tag{6.3}$$

so the coupling constant at the optimum grating period determined in Eqn. (6.2) is proportional to E_N and E_d in Eqn. (6.3):

$$\Gamma \propto \frac{E_N E_d}{E_N + E_d} = \frac{1}{2}\sqrt{\frac{k_B T N_A}{\epsilon}\left(1 - \frac{N_A}{N_D}\right)}. \tag{6.4}$$

Figure 6-1 shows the predicted behavior of the space charge field, which determines the coupling constant Γ, as a function of grating period for several values of the trap density N_A. It also follows from Eqns. (6.2) and (6.4) that for $N_A \ll N_D$, the optimum grating period goes as $(N_A)^{-\frac{1}{2}}$, so if the gain is measured at the optimum grating period corresponding to the particular value of N_A, the coupling constant goes as $(N_A)^{\frac{1}{2}}$.

6.2.2. Experimental results of trap density vs. gain

The experimental results of optimizing grating spacing to maximize the two-beam coupling gain were shown in Fig. 5-2 for Ce-doped and Rh-doped SBN, and in Fig. 5-3 for Cr-doped SBN:60 and SBN:75.[1-4] Eqn. (6-1) was used to obtain the best fit line in the two figures, where the experimentally measured peak of the photorefractive gain as a function of grating period was used in determining the $\lambda_{g,max}$ parameter for the fit. Table 6-1 shows the optimum grating periods and corresponding trap densities of the various SBN:60 and SBN:75 crystals used in this work.

Note that for small grating periods, the space charge field is linear in λ_g, since in the model, as the grating period is increased, charges are separated within a larger volume in the crystal, resulting in more total charge migrating to the peaks of the light interference pattern. This results in a larger electric field due to the charge separation. However, at grating periods larger than the Debye screening wavelength, diffusion becomes a significant factor and results in the space charge field dropping off as $1/\lambda_g$ for $\lambda_g > \lambda_{g,max}$.

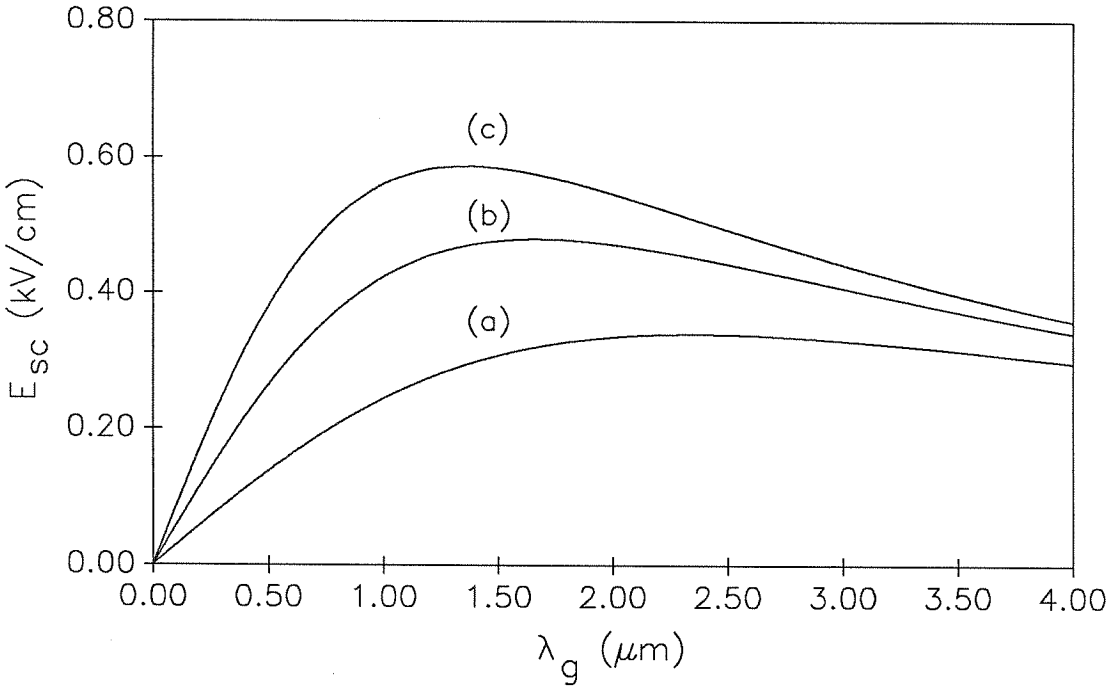

Fig. 6-1: Space-charge field as a function of grating period for (a) $N_A = 10^{22}$ m^{-3}, (b) $N_A = 2 \times 10^{22}$ m^{-3}, and (c) $N_A = 3 \times 10^{22}$ m^{-3}.

Material	ϵ_r	$\lambda_{g,max}$ (μm)	N_A (10^{22} m^{-3})
SBN:60:Cr (0.01)	1572	2.50	1.41
SBN:60:Cr (0.016)	1083	3.02	0.67
SBN:60:Cr (0.03)	1018	2.50	0.92
SBN:75:Cr	5844	5.77	0.17
SBN:60:Ce	850	1.58	1.90
SBN:60:Rh	582	1.20	2.27
SBN:60:Cr (0.01)*	1261	2.75	0.94

*After heat treatment

Table 6-1: Optimum grating period for maximum photorefractive gain and trap density of the SBN:60:Cr, SBN:75:Cr, SBN:60:Ce, and SBN:60:Rh crystals.

6.3. Oxidation and reduction of SBN

Increasing the trap density of a material opens up another possible avenue in attempting to increase the maximum space charge field that can be sustained in the crystal. This is especially true in the case that will be described in Sec. 6.5 when external fields are also utilized. The reverse of this problem may also occur, as in the KTN crystals described in Chapter 4, where there are insufficient numbers of dopant atoms in the proper oxidation state to act as donors, in which case the donor density must be increased. Oxidation or reduction of as-grown samples through heat treatments provide a mechanism for making these alterations in the trap and donor densities after growth.

6.3.1. Desired effect on donor/trap densities

The objective of oxidation is to transform some of the dopants to their higher oxidation states, so the number density of traps is increased. In the model where the space charges are assumed to be concentrated at the minima of the light interference pattern so the system can be described as a simple capacitor, this would enable more charges to be placed at each capacitor plate, resulting in an increased space charge field in the crystals.

The opposite occurs in a crystal that is donor limited. One example already mentioned was KTN:Cr,Fe, where the as-grown crystal was deemed to be dominated by the Cr^{6+} oxidation state of the dopant. Although these materials showed photorefractive diffraction, significant improvement in the magnitude and time response of the photorefractive effect was realized after the crystals were reduced through the following process:

$$3O^- + Cr^{6+} \rightarrow Cr^{3+} + 3V_O + 3e^- + \frac{3}{2}O_2 \,,$$

where V_O is an oxygen vacancy. The absorption spectrum also indicates the effect

of reduction in these materials through changes in the magnitude of the photoabsorption band. As can be seen in Fig. 3-2, which is the absorption spectrum of KTN:Cr,Fe before and after reduction, an expanded photoabsorption band is present at approximately 600 nm in the reduced crystal when compared to the as-grown one.

6.3.2. Procedure for reduction/oxidation

Reduction was accomplished by baking the sample in an oxygen-deficient atmosphere for several hours at temperatures ranging from 500 to 800° C, depending on the material and the degree of reduction required. This procedure was described in Chapter 4 for reduction of Cr^{6+} to Cr^{3+} in KTN:Cr,Fe. In most cases KTN required temperatures of up to 800° C for reduction, while in SBN temperatures of about 400 to 500° were usually sufficient.

In the case of oxidation, the crystal was baked in air in an open quartz test tube, then cooled slowly back to room temperature. In most cases, it was not deemed to be necessary to bake the crystal in a pure oxygen atmosphere because the presence of other inert gases tended to moderate the process. After the procedure, the effects were checked by measuring the absorption spectrum and comparing it to that taken before the process.

Experiments in reducing and oxidizing Cr-doped SBN:60 were carried out with the goal of changing the photorefractive gain or response time by modifying the material propreties of the as-grown crystal. The 0.01 wt. % Cr-doped SBN:60 crystal, which had a relatively low gain of 3 cm^{-1} but a fast response time of 0.2 sec, was initially reduced by heating in $\frac{1}{3}$ atm or Ar for 2 hr at 500° C in the hopes of further reducing its response time. However, the result was over-reduction of the crystal, which became opaque and highly conductive. This was probably due

to reducing the oxygen vacancies and Nb as well as the Cr dopant. In the hopes of restoring the original properties of the crystal, it was heated in air for 2 hr at 400° C to re-oxidize it. The sample was then repolished and repoled with a field of approximately 8 kV/cm.

6.3.3. Effects of trap and donor densities on space charge

Oxidation and reduction heat treatments will have the primary effect of changing the relative concentration of traps and donors, increasing the number of one at the expense of the other. Since the concentration of the dopants will remain unchanged, the assumption that $N_{A,C}^{-} + N_D = N_0$ can be made for the simplified model in the following discussion, where N_0 is a constant that represents the total concentration of impurities in the crystal.

For cases where the grating period is fixed, E_d will remain constant for a fixed temperature. Therefore the only dependence on $N_{A,C}$ will be through E_N, which is given by

$$E_N = \frac{eN_A}{\epsilon K}\left(1 - \frac{N_A}{N_0 - N_A}\right). \tag{6.5}$$

Figure 6-2 shows the dependence of the two characteristic fields, E_d, the diffusion field, and E_N, the maximum space charge field, on the trap density N_A. For the plot, N_0 was set at 10^{24} m^{-3}, which corresponds to a dopant concentration of approximately 0.01 wt. %. In addition, the following values for the various material parameters were assumed: $\lambda_g = 2$ μm, $\epsilon = 10^3\epsilon_0$, and $T = 300$ K. For small N_A relative to N_0, E_{sc} is shown to be increasing with trap density as more electrons are trapped, creating a larger internal field. For the limiting case where $N_A = N_0$, the lack of donors results in the maximum space charge field going back down to zero.

The space charge field at the optimum grating period for no external field will

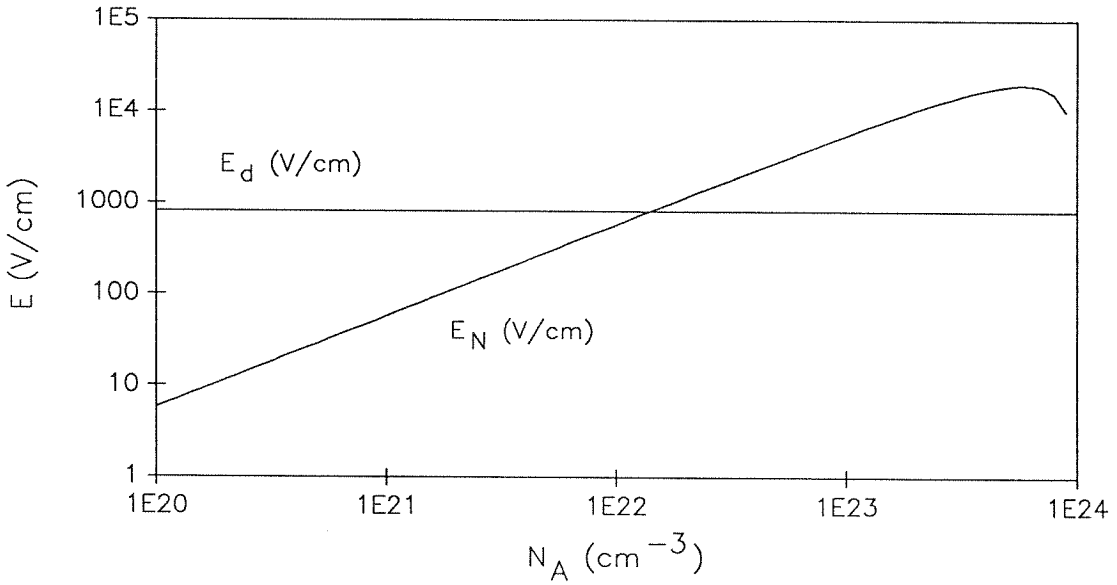

Fig. 6-2: Diffusion field E_d and maximum space charge field E_N as a function of trap density N_A for a fixed grating period $\lambda_g = 2$ μm.

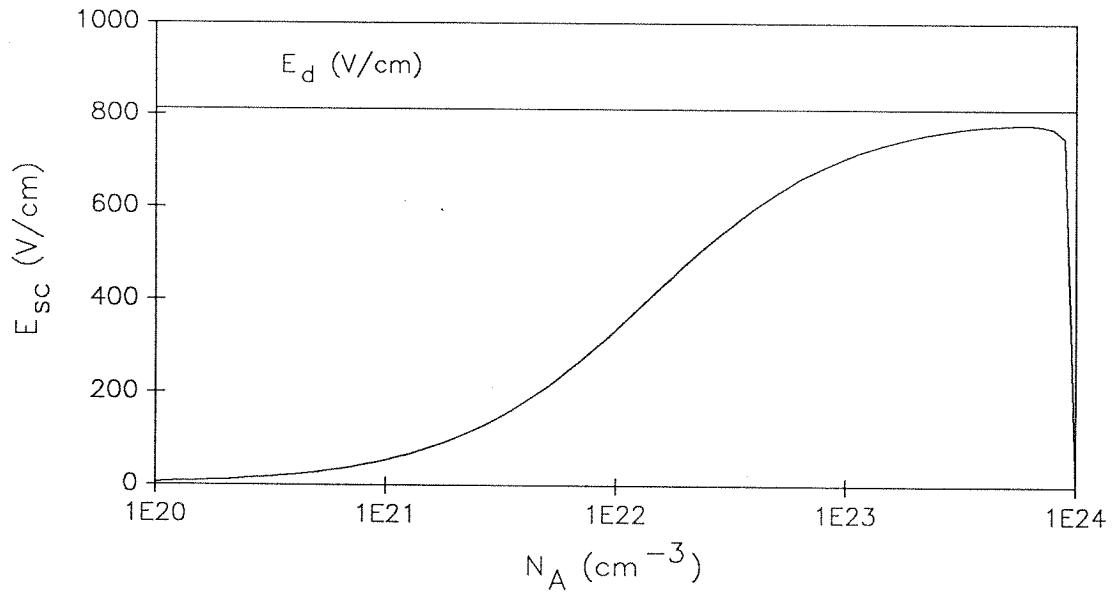

Fig. 6-3: Space charge field as a function of trap density for a fixed grating period.

then be given by

$$E_{sc} = -im\frac{ek_BTKN_A(1-\frac{N_A}{N_0-N_A})}{e^2N_A(1-\frac{N_A}{N_0-N_A})+\epsilon k_BTK^2}\,, \tag{6.6}$$

where N_A is the trap density, N_0 is the total impurity density, and m is the modulation depth. The plot of E_{sc} for $N_0 = 10^{24}$ m^{-3} and $\lambda_g = 2$ μm is shown in Fig. 6-3, with the constant E_d plotted for comparison. Note that at larger E_{sc}, the diffusion field becomes the limiting factor. For the donor limited case of $N_A \approx N_0$, the space charge field again goes to zero.

If the grating period is set equal to its optimum value for each new value of N_A, E_N and E_d will be equal as indicated by Eqn. (6.3). A plot of the space charge field in this instance is shown in Fig. 6-4, and this indicates a $(N_A)^{\frac{1}{2}}$ increase with N_A, except that the space charge field goes to zero as N_A approaches N_0. Another consideration is that the optimum grating period, and therefore the required incidence angle of the writing beams on the crystal, changes with N_A as shown in Fig. 6-5, and the maximum possible incidence angle may be constrained by experimental geometries.

6.3.4. Experimental results

The resulting heat-treated Cr-doped SBN:60 crystal, although having a physical appearance, color, and absorption spectrum resembling that of the original as-grown crystal, had a number of interesting properties that warranted further study. The process resulted in changes to its original photorefractive properties, including a significant increase, by almost a factor of three in the gain coefficient. Along with the increased gain was a slight increase in the response time and increased temperature stability of these photorefractive parameters over temperatures from 253 to 313 K.

The photorefractive gain of the crystal before and after the heat treatment

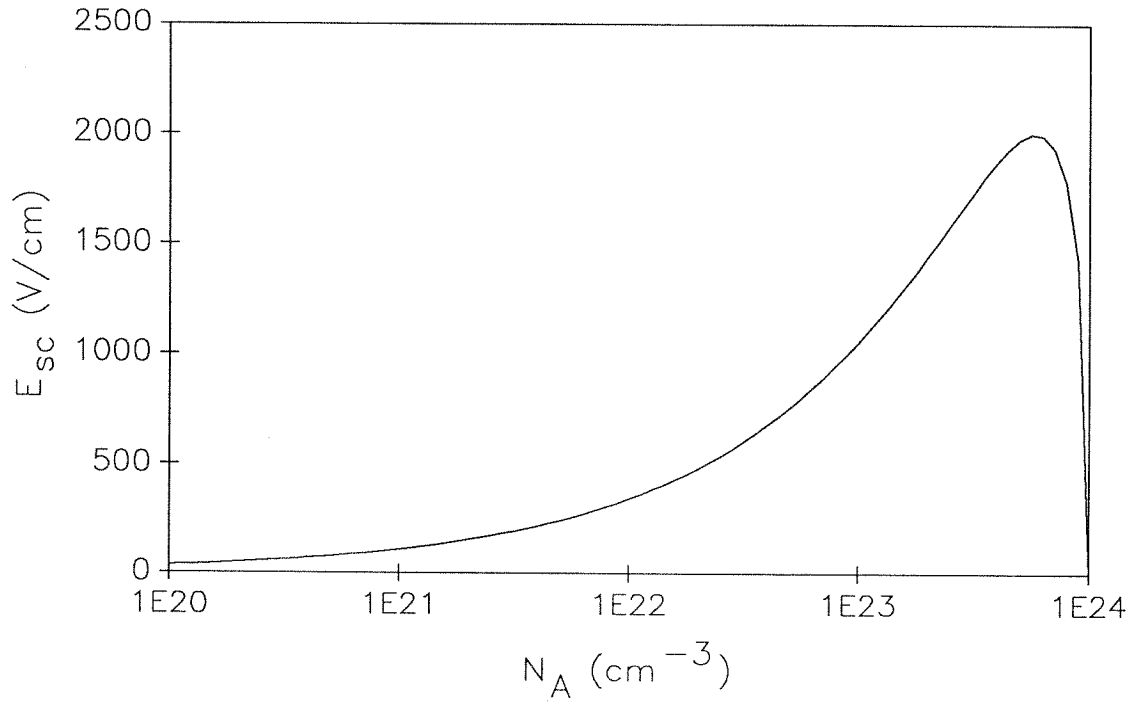

Fig. 6-4: Space charge field at the optimum grating period as a function of trap density, showing a $\sqrt{N_A}$ dependence for $N_A < N_0$.

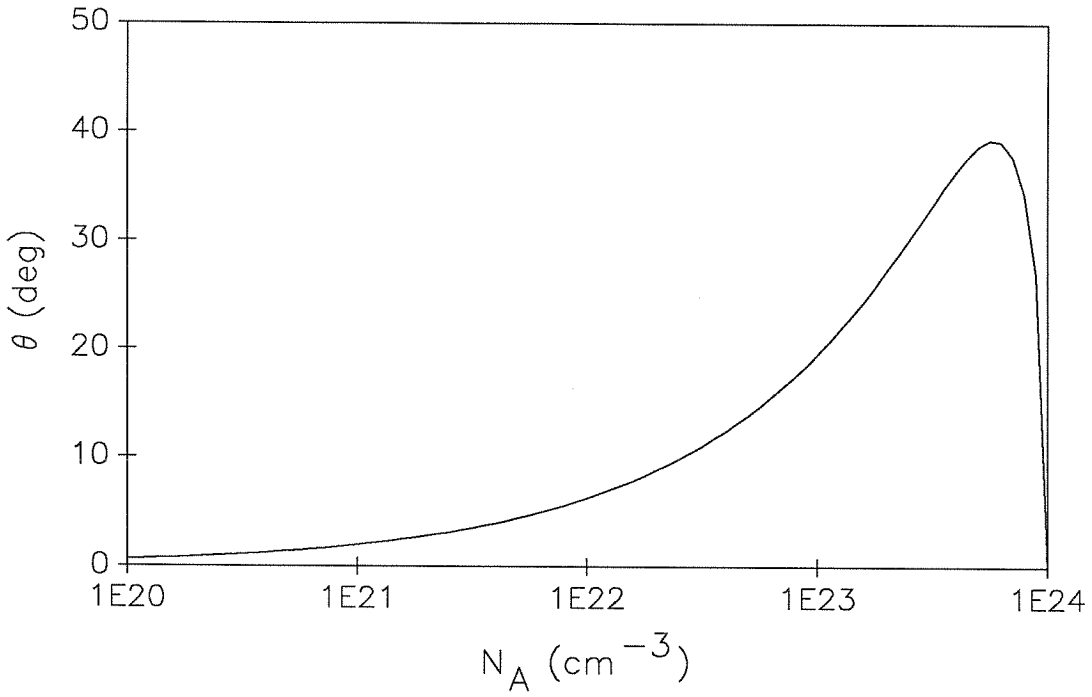

Fig. 6-5: Intersect angle required for the two incident beams in order to obtain the optimum grating period as trap density is varied from 10^{20} to 10^{24} m^{-3}.

process as a function of grating period is shown in Fig. 6-6(a). The coupling constant increased to approximately 8 cm^{-1} at the optimum grating period of 2.5 μm in the annealed crystal. In comparison, the original value for the gain in the as-grown crystal was 3 cm^{-1} at $\lambda_g = 2.5$ μm. The response time was also affected by the process, and its result is shown in Fig. 6-6(b) compared to its original value before the annealing process.

In addition to any changes in N_A in the heat treated crystal, other factors may also be responsible for the large increase in the gain. From Sec. 5.4, it appears that variations in the poling voltage is not a significant factor affecting the photorefractive properties of SBN. However, some of the other factors that may have had an effect are changes in the electro-optic coefficient, dielectric constant, and defects in the crystal.

Increased temperatue stability was also observed in the heat-treated crystal. As shown in Fig. 6-7(a), the gain varied from 8.0 to 6.8 cm^{-1}, which was within a factor of 10% of its room temperature value of 7.6 cm^{-1}, over a temperature range of 253 to 313 K at $\lambda_g = 2.5$ μm, the optimum grating period. The as-grown sample had demonstrated a strong temperature dependence of the gain, which ranged from 4.9 cm^{-1} at 238 K to 0.93 cm^{-1} at 313 K. Figure 6-7(b) shows the temperature dependence of the response time for the crystal before and after heat treating, which shows a similar effect as the gain. The improved stability of the heat treated crystal that can be attributed in part to its reduced thermal excitation eliminates or scales back the need for temperature control of devices utilizing this effect for operation in temperature-varying environments.

6.4. Temperature

Certain SBN crystals have been observed to show strong temperature

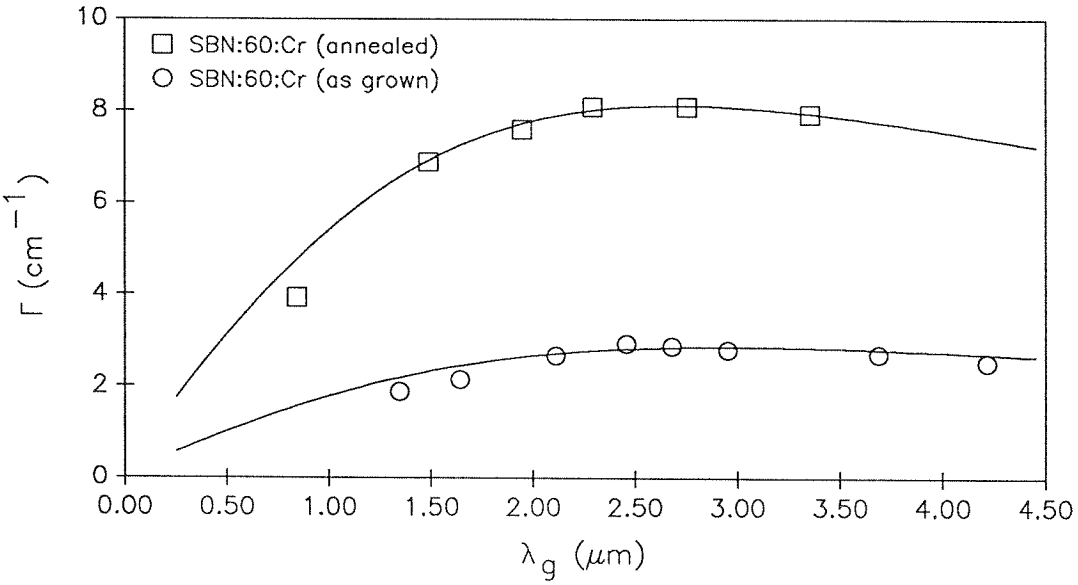

(a)

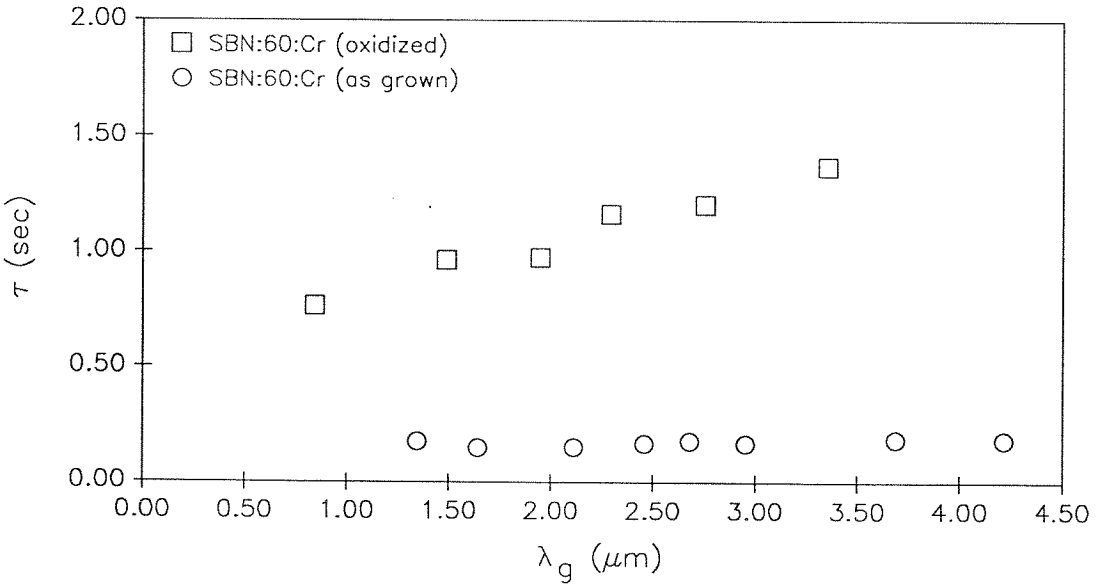

(b)

Fig. 6-6: Photorefractive properties of 0.01 wt. % Cr-doped SBN:60 before and after oxidation – (a) coupling constant, and (b) response time.

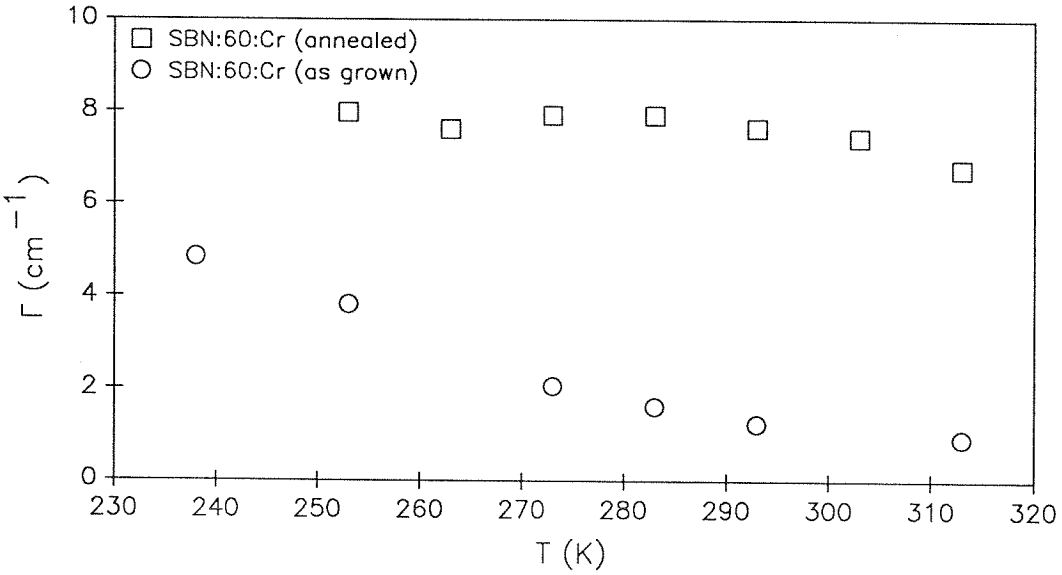

(a)

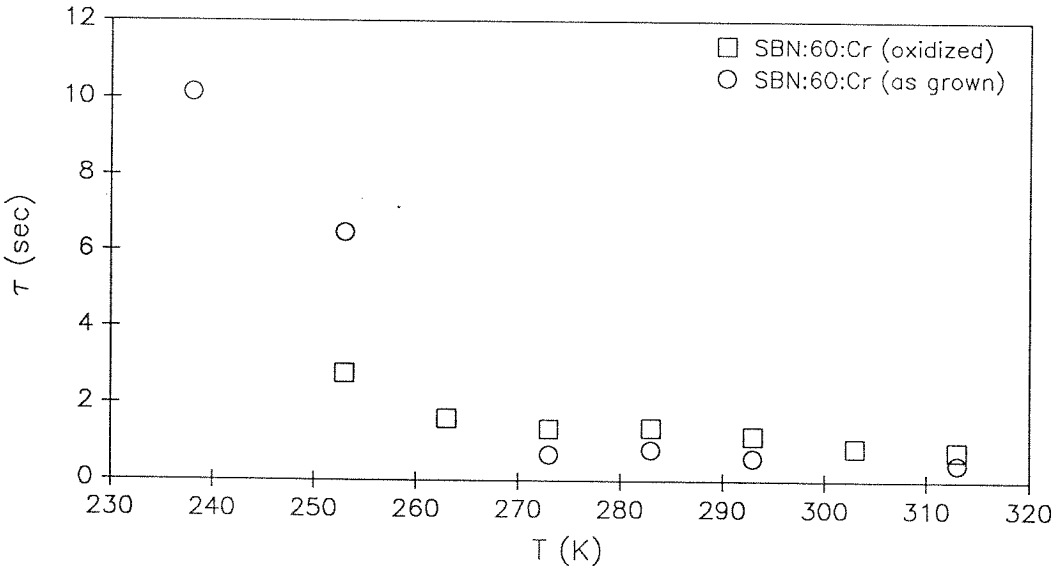

(b)

Fig. 6-7: Temperature dependence of the photorefractive properties of as-grown and heat-treated SBN:60:Cr – (a) coupling constant, and (b) response time.

dependence in their photorefractive properties, which in most cases was gain increases with cooling and faster response time upon heating. Temperature dependences are carried in several material parameters and characteristic fields used in determining the photorefractive constants, including the diffusion field, dielectric constant, electro-optic coefficient, mobility, and dark conductivity.[5,6] The variability of these parameters through temperature control enables the crystal properties to be improved depending on specific needs.

6.4.1. Dielectric constant and electro-optic coefficient

The dielectric constant of a ferroelectric material is strongly dependent on temperature near its phase transition temperature, which for most SBN samples is around 348 K. Below the phase transition, the dielectric constant approximates the Curie-Weiss Law dependence. By heating the crystal to near its phase transition, but not to the extent of risking depoling, the dielectric constant, and therefore the electro-optic coefficient, can be increased. However, any improvement through heating may be nullified by the effect of temperature changes on other parameters. Fig. 5-9 shows the experimentally measured temperature dependence of the dielectric constant for several SBN crystals, which gives an indication of the temperature dependence of the effective electro-optic coefficient.

6.4.2. Characteristic fields

In the equations determining the photorefractive gain and response time, the diffusion field, given by

$$E_d = \frac{k_B T K}{e}, \tag{6.7}$$

contains an explicit temperature dependence that affects the space charge field if there is no external field. As derived in Chapter 2, the space charge field is always less than the smaller of E_d and E_N, so increasing the diffusion field through

increased temperatures in cases that E_d is the limiting factor should allow larger space charge fields. In cases where $E_N < E_d$, increasing E_d will still increase the overall space charge field, up to the point where $E_{sc} = E_N$.

The maximum space charge field also has a temperature dependence through the dielectric constant ϵ. As a result of increasing ϵ as the temperature approaches that of the phase transition, the maximum space charge field will decrease with increasing temperature, which may counteract any gains from a larger diffusion field and electro-optic coefficient.

6.4.3. Dark conductivity

The effect of dark conductivity was discussed in Sec. 5.5, with particular emphasis on the temperature dependence of this effect and its impact on photorefractive parameters. Strong inverse temperature dependences in the photorefractive gain coefficients were observed for materials deemed to have high dark conductivities due to their short dark decay times, while those with low dark conductivities did not have strong temperature dependences. This includes the annealed SBN:60:Cr crystal in Sec. 6.3, where the dark conductivity was probably among the properties affected by the heat treatment process.

Dark conductivity also acts to speed up the response time of the crystals through reducing the grating formation time. Although the grating magnitude, and hence the gain coefficient, will be smaller, applications requiring faster response time may not require large gain. As the dark conductivity increases with temperature due to larger thermal excitation, the fundamental response time t_0 will see further increases.

6.4.4. Experimental results

Figures 5-10(a), 5-10(b), 5-14(a), and 5-14(b) show the photorefractive gain

coefficient and response times as a function of temperature for Ce- and Cr-doped SBN:60, Cr-doped SBN:60, Cr-doped SBN:75, and Rh-doped SBN:60. In all these samples gain decreased, the extent depending on the particular crystal, as they were heated. However, heating the crystals resulted in some reduction in their response times, which is consistent with efforts in heating $BaTiO_3$ to speed up its response.

In each of the measurements, I_0 was 0.25 W/cm^2, with the beam intensity ratio $I_2(0)/I_1(0) \ll 1$ to avoid pump beam depletion. The crystals were cooled in a cryostat and the temperature allowed to stabilize before the experiments. Between measurements, any residual gratings were erased by uniform illumination. The response time was taken to be the exponential buildup time of the two-beam coupling constant.

6.5 External DC electric fields

Two-beam coupling in ferroelectric SBN crystals doped with various transition metals combinations including Fe, Ce, Ce-Ca, Cr, and Rh have been shown to have high photorefractive gain and response times on the order of 0.1 to 1.0 sec. This mechanism has been responsible for a variety of optical devices including phase conjugate mirrors and optical amplifiers. The experimental results presented so far have been measurements with no applied electric field, that is, with $E_0 = 0$. However, by applying an external field of up to 10 kV/cm, significant improvements in the photorefractive properties, either the coupling constant or the response time, has been realized.[7]

6.5.1. Expected effect on photorefractive properties

As derived in Chapter 2, the photorefractive two-beam coupling constant, which characterizes the magnitude of the photorefractive two-beam coupling effect,

is given by[8-10]

$$\begin{aligned}\Gamma =& \mathrm{Re}\left(\frac{i\omega}{4c} n_0^3 r_{\mathrm{eff}} E_{\mathrm{sc}}\right) \\ =& \frac{\omega}{4c} n_0^3 r_{\mathrm{eff}} m E_N \frac{E_0 + iE_d}{E_0 + i(E_d + E_N)} [1 - \exp(-t/\tau)],\end{aligned} \tag{6.8}$$

for the one carrier, one species case of electrons being the dominant charge carrier and only one donor type being photoactive. The response time of the exponential buildup of two-beam coupling is given by

$$\tau = t_0 \frac{E_0 + i(E_d + E_\mu)}{E_0 + i(E_d + E_N)} . \tag{6.9}$$

Recall that the characteristic fields are given by

$$\begin{aligned}E_N =& \frac{eN_A}{\epsilon K}\left(1 - \frac{N_A}{N_D}\right) \approx \frac{eN_A}{\epsilon K} \text{ for } N_A \ll N_D \\ E_d =& \frac{k_B T K}{e} \\ E_\mu =& \frac{\gamma N_A}{\mu K} .\end{aligned} \tag{6.10}$$

For typical values of $N_A = 2 \times 10^{-22}$ m^{-3}, $\epsilon = 570\epsilon_0$, $T = 295$ K, $\lambda_g = 1.5$ μm, and $\gamma/\mu = 2 \times 10^{-10}$ V-m, which are used later in this section for the graph of the expected photorefractive parameters, the characteristic fields are $E_d = 1.06$ kV/cm, $E_N = 1.55$ kV/cm, and $E_\mu = 10$ kV/cm.[2,11]

A major thrust of current photorefractive materials research is the increase of the coupling constant Γ. An unfortunate consequence of Eqn. (6.8) is that with $E_0 = 0$, E_{sc} tends towards the smaller of E_N and E_d. The obvious strategy of increasing the trap density N_A by increasing the acceptor doping will be effective only to the extent of getting E_{sc} to approach E_d.

To take advantage of increased doping so that E_{sc} is made to approach the maximum "available" field E_N, we need to drive the photo-excited carriers into the traps (a half grating period away) against the retarding space charge field.

This can be done by an imposed external field E_0. Indeed in the limit $E_0 \gg E_N > E_d$, Eqn. (6.8) predicts $E_{sc} \approx imE_N$. The theoretically predicted dependence of E_{sc} on E_0 for two typical cases, one where $E_N < E_d$ and the other for $E_N > E_d$, is illustrated in Fig. 6-8.

The external field will also have an effect on the response time τ. From Eqn. (6.9), it can be seen that in the limit of large E_0, τ approaches t_0, which is the fundamental limit of the time required to generate N_A photoexcitations per unit volume from energy deposition considerations.[12] In the $E_\mu > E_N$ case, which typically holds, τ approaches its limit from above as the dc field is increased. Using the typical values given above, that is $E_N = 1.55$ kV/cm, $E_d = 1.06$ kV/cm, and $E_\mu = 10$ kV/cm, Fig. 6-9 shows the expected decrease in τ/t_0 as E_0 increases under these conditions.

6.5.2. Gain Enhancement in Cr-doped SBN

To test the above conclusions, the coupling constant Γ was measured as a function of the applied field E_0 in a number of Cr-doped strontium barium niobate samples.[10] These were the 0.01, 0.016, and 0.03 wt. % Cr-doped SBN:60 crystals. The gain coefficients for these crystals with no applied fields were 2.93, 5.28, and 2.90 cm^{-1} at their optimum grating periods, respectively. The experimental measurements were made at $\lambda_g = 1.73$ μm for the 0.01 and 0.016 wt. % crystals, where their gain with no field was 2.2 and 3.7 cm^{-1}. The measurements for the 0.03 wt. % crystal were made at $\lambda_g = 2.41$ μm, where the gain was 2.90 cm^{-1}. The other significant material parameters were: $N_A = 1.4 \times 10^{22}$ m^{-3}, $\epsilon = 1.57 \times 10^3$ ϵ_0, and response time $\tau = 0.16$ sec for the 0.01 wt. % Cr-doped crystal, $N_A = 6.7 \times 10^{21}$ m^{-3}, $\epsilon = 1.1 \times 10^3$ ϵ_0, and $\tau = 0.59$ sec for the 0.016 wt. % Cr-doped sample, and $N_A = 9.2 \times 10^{21}$ m^{-3}, $\epsilon = 1.0 \times 10^3$ ϵ_0, and $\tau = 0.12$ sec

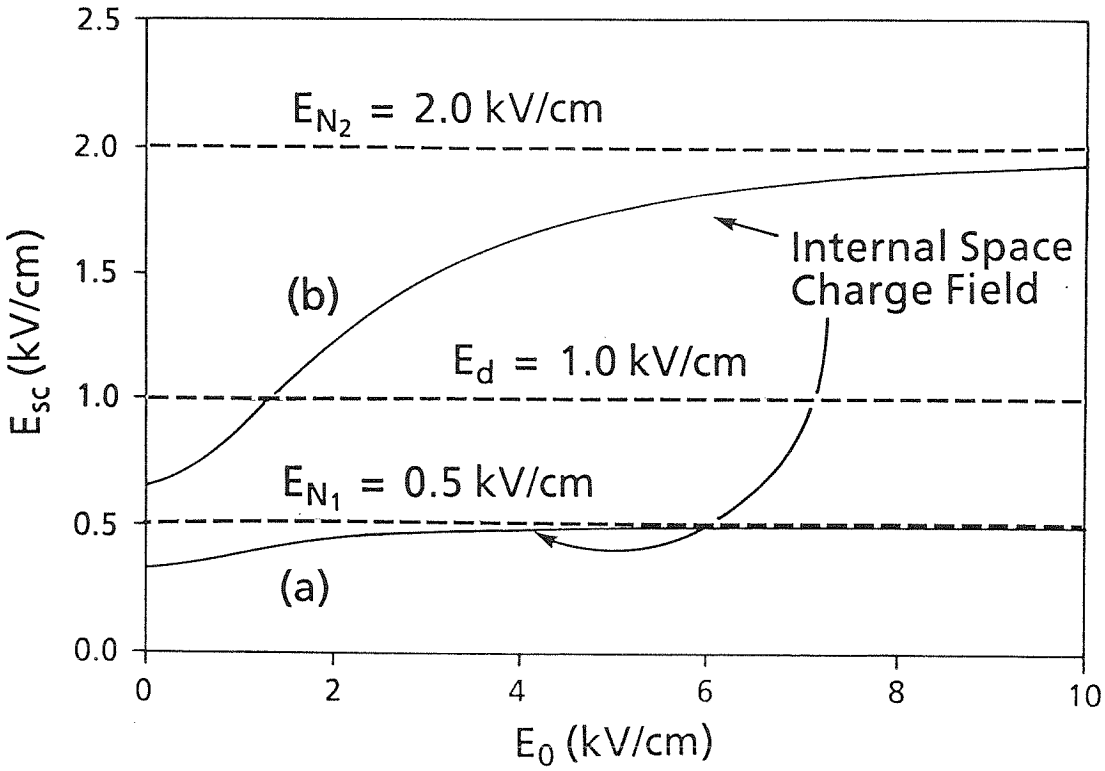

Fig. 6-8: Expected space-charge field as a function of the applied DC field for (a) $E_N < E_d$, with $E_N = 0.5$ kV/cm and $E_d = 1.0$ kV/cm, and (b) $E_N > E_d$, with $E_N = 2.0$ kV/cm and $E_d = 1.0$ kV/cm. Note that the space-charge field approaches E_N for large E_0.

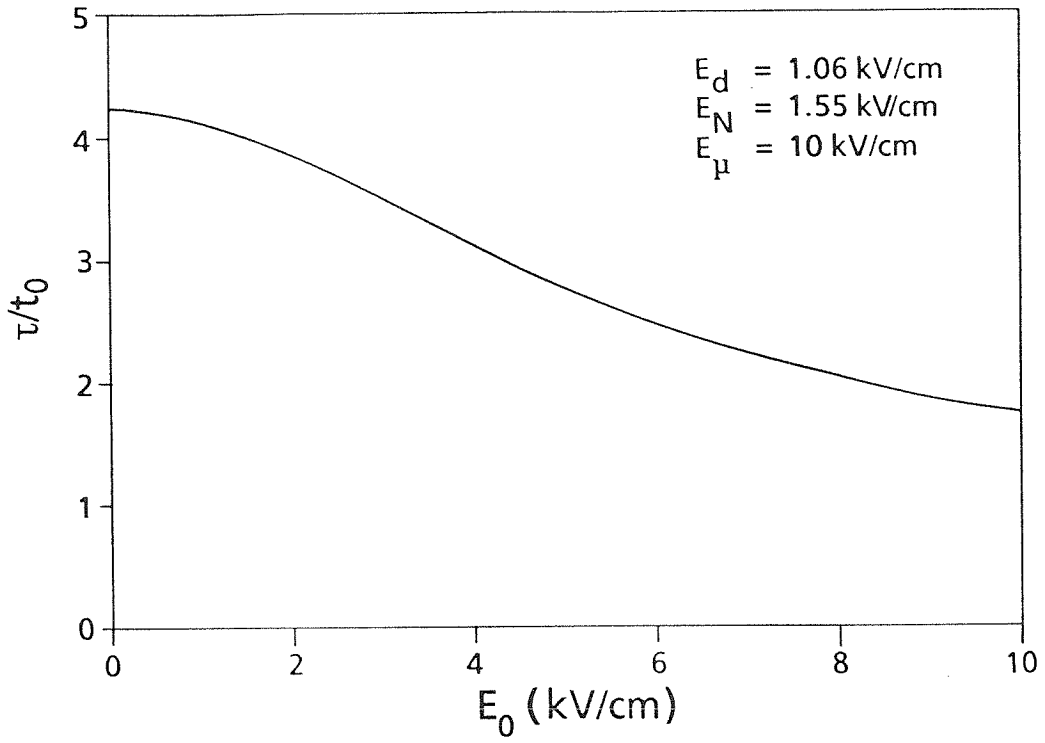

Fig. 6-9: Expected response time as a function of applied field for $E_d = 1.06$ kV/cm, $E_N = 1.55$ kV/cm, and $E_\mu = 10$ kV/cm, showing τ/t_0 approaching unity for large applied field E_0.

for the 0.03 wt. % Cr-doped SBN.[1,2]

The effect of applying a DC field on the coupling constant is shown in Fig. 6-10 for the three Cr-doped SBN:60 samples. All three showed significant increases in the photorefractive gain coefficient, from less than 4 cm^{-1} to more than 10 cm^{-1} with a 10 kV/cm external field for the 0.016 wt. % crystal. The 0.01 wt. % doped crystal showed an increase from 2.15 cm^{-1} at $E_0 = 0$ to 4.7 cm^{-1} at $E_0 = 8$ kV/cm, while the gain of the 0.03 wt. % sample increased from 2.96 to 4.48 cm^{-1} at $E_0 = 6$ kV/cm. The expected behavior of Γ as a result of the dependence of the space charge field on the applied field E_0 is shown using the initial $E_0 = 0$ value as the operating point. At the higher applied fields, the gain is shown to be increasing beyond the theoretical model due to the effect of the applied field on other material parameters which were assumed to be constant with E_0; further investigation is continuing in this area.

It is important to recall that the exponential nature of the two-beam coupling, that is,

$$\begin{aligned} I_1(\ell) &= I_1(0)e^{-\Gamma\ell} \\ I_2(\ell) &= I_2(0)e^{\Gamma\ell}, \end{aligned} \tag{6.11}$$

makes a factor of 2 increase in Γ of major importance in the device applications which utilize this effect. This makes it possible to obtain large coupling effects using these materials, or to use thinner crystals of SBN to obtain a given coupling constant in the experiments and devices.

The exponential time constant for the photorefractive gain coefficient to build up to its steady state value was also measured to determine the effectiveness of applying a field on real-time devices using these materials, with the results shown plotted in Fig. 6-11. In the 0.016 wt. % crystal, the time constant remained fairly constant at approximately 0.5 to 0.6 sec. for $E_0 \leq 6$ kV/cm, and increased slowly

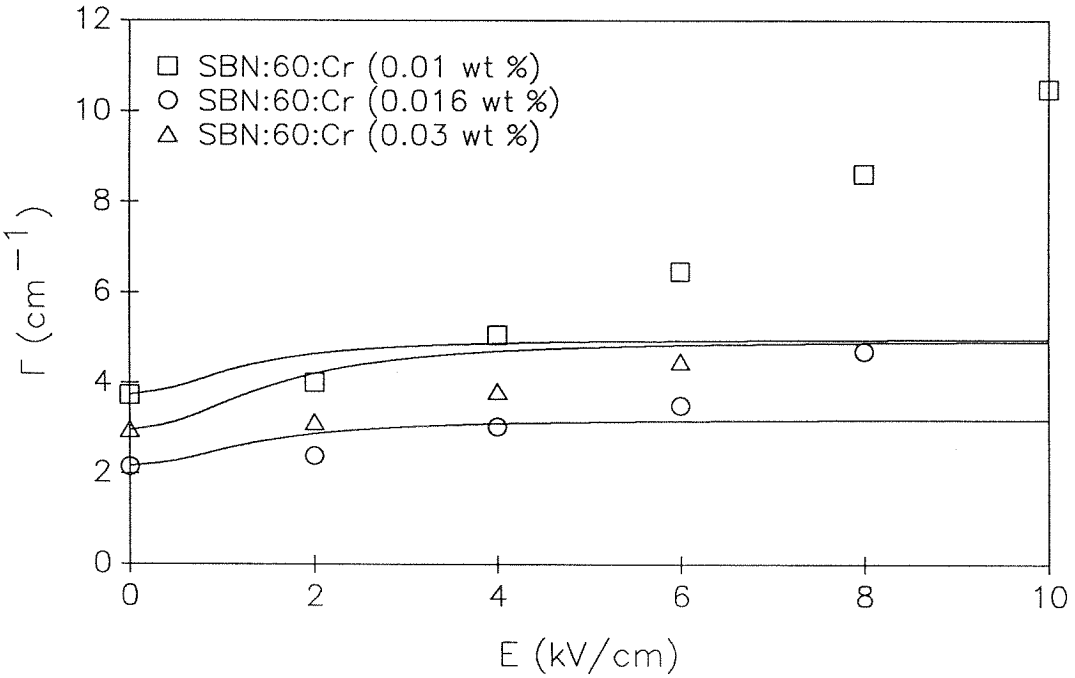

Fig. 6-10: Photorefractive two-beam coupling constant of the three Cr-doped SBN:60 samples as an external DC field from 0 to 10 kV/cm was applied. The increase in Γ beyond that predicted by theory may be the result of changes in some material parameters at high E_0 or the effects of beam intensity depletion due to fanning. The $E_0 = 0$ value of Γ was used as the initial operating point.

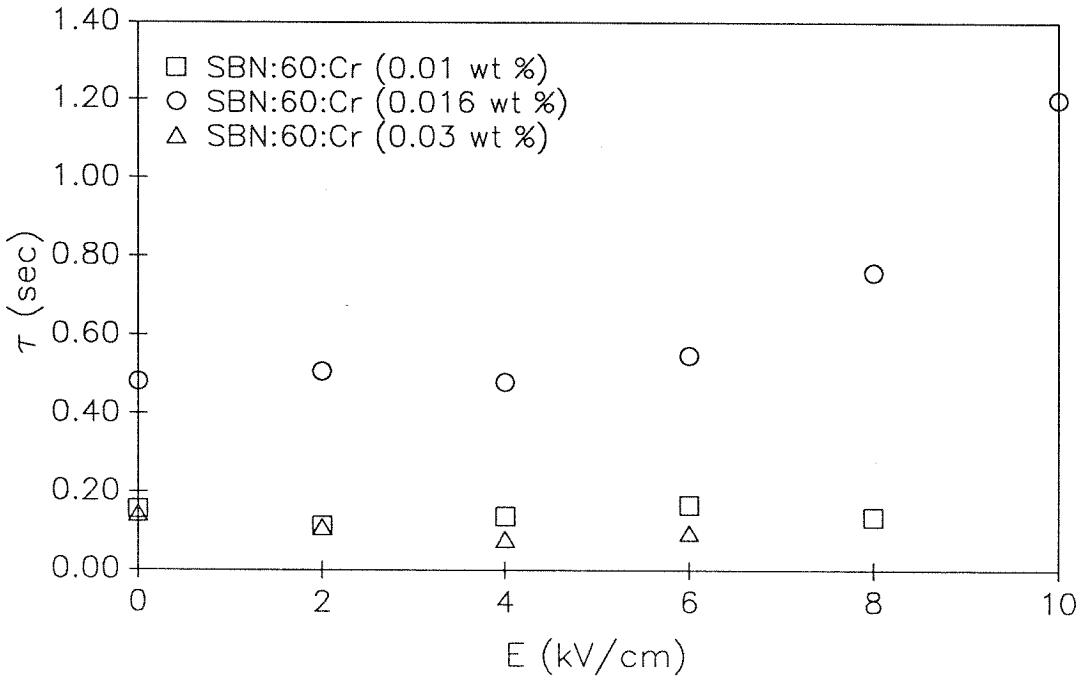

Fig. 6-11: Response time of the SBN:60:Cr crystals with an external DC field. The time constant remains within an order of magnitude of its value at $E_0 = 0$.

for higher fields up to 10 kV/cm, while with the 0.01 wt. % sample, the time constant was not noticably affected by the applied field and remained relatively constant at 0.2 sec for E_0 up to 8 kV/cm. In the case of the highly doped, 0.03 wt. % crystal, the response time was reduced for fields up to 6 kV/cm, except for the apparently anomalous point at $E_0 = 4$ kV/cm.

These experiments were carried out at room temperature, with λ_g fixed at either 1.73 or 2.41 μm, and total intensity $I_0 = 0.25$ W/cm^2. The ratio $I_2(0)/I_1(0)$ was set at less than 0.01 to avoid pump depletion. The field was applied in the direction of the c-axis since high reverse voltages would tend to reduce the polarization and ultimately depole the crystal, and it was turned on just before the crystal was illuminated with both beams simultaneously at $t = 0$. Fields significantly higher than 10 kV/cm were not attempted owing to considerable arcing across the surface of the crystal.

6.5.3. Response time reduction

As described in Sec. 6.5.1, the response time for photorefractive grating buildup and erasure decreases as a function of E_0, the applied electric field, for cases where $E_\mu < E_N$. Although one example with Cr-doped SBN in the previous section showed a longer response time, others such as the 0.03 wt. % Cr-doped and Rh-doped SBN:60 crystals showed significant reductions in their response time constants with an applied dc field.[3]

The experimental results of the gain and response time of Rh-doped SBN:60 with an applied electric field are shown in Figs. 6-12 and 6-13 for $\lambda_g = 1.51$ and 0.84 μm. The electric field, which varied from 0 to 10 kV/cm, was applied in the direction of the c axis. For both grating periods, the gain of the Rh-doped SBN:60 crystal dropped from $\Gamma = 10$ cm^{-1} at $E_0 = 0$ to near 8 cm^{-1} at $E_0 = 10$ kV/cm.

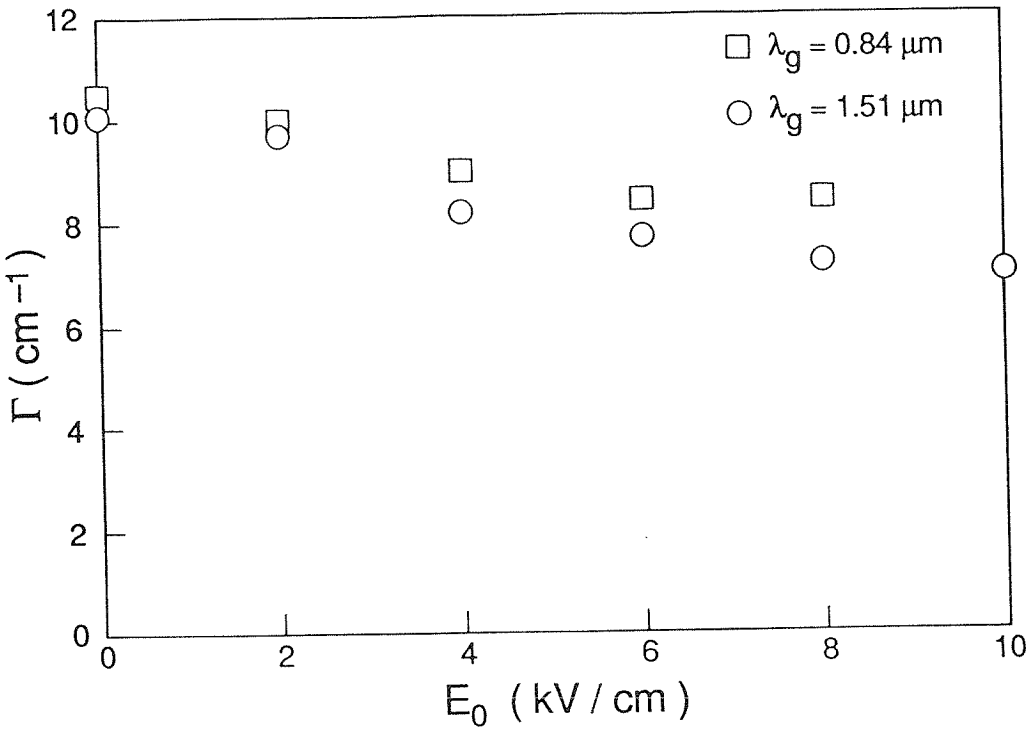

Fig. 6-12: Measured gain coefficient as a function of E_0 for $\lambda_g = 1.51$ and 0.84 μm.

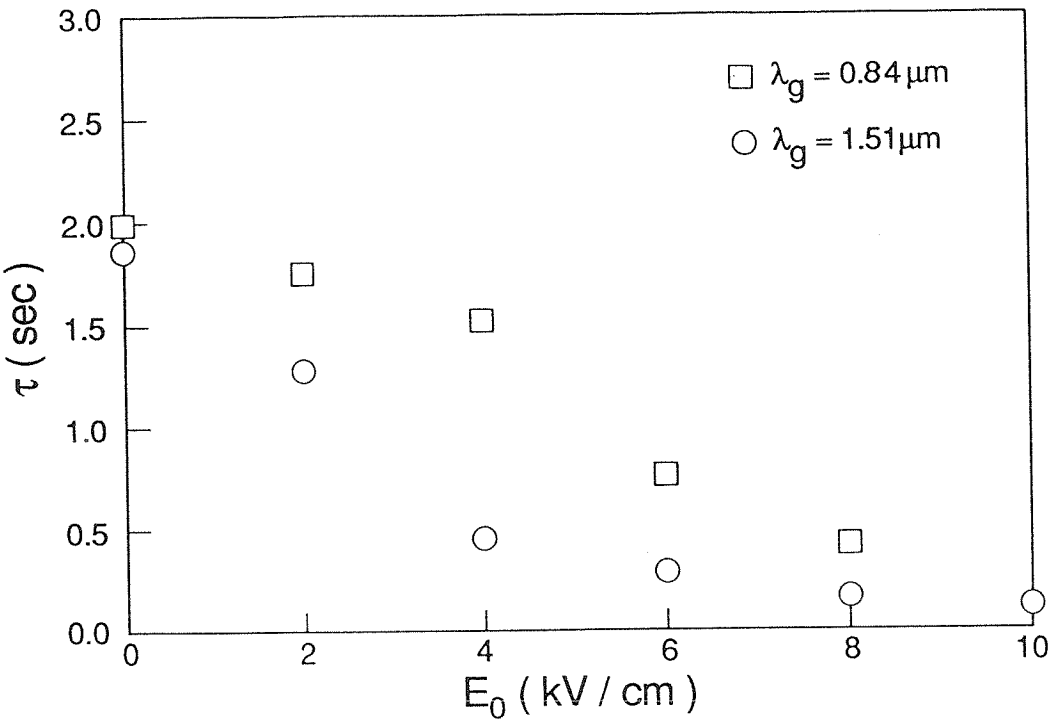

Fig. 6-13: Experimental response time of the SBN crystal for $\lambda_g = 1.51$ and 0.84 μm, which decreased from 2 sec at $E_0 = 0$ to approximately 0.1 sec for $E_0 =$ 10 kV/cm.

Although Eqn. (6.8) predicts that the gain increases with E_0, the small decline in this case can be attributed to such causes as fanning losses from the large gain and increased scattering.

The advantage of this procedure, however, is in the reduction in the response time by more than an order of magnitude, which was observed to decrease from 2.0 sec at $E_0 = 0$ to approximately 0.1 sec at $E_0 = 10$ kV/cm. Strong beam fanning was also observed to set in faster as the time constant was reduced through increased E_0, making this material especially suited for high-gain, fast-response applications such as field-enhanced optical limiters and real-time image processing. According to the theoretical model, the photoexcited charges are transported through drift and diffusion in the conduction band. The presence of the dc field in the background would tend to drive the free electrons into the traps, contributing to the faster grating formation that was observed.

6.6. Summary

Control of the grating period in two-beam coupling, trap and donor densities, temperature, and external dc fields were investigated as means to increase the photorefractive gain or reduce the response time of SBN. Heat treatments have succeeded in increasing the gain almost threefold in Cr-doped SBN:60. Higher temperature has resulted in increased speed of response in most SBN samples studied, but at the cost of lower gain. External fields have be successfully used to increase gain in SBN:60:Cr and reduce response time by over an order of magnitude in SBN:60:Rh. The equations for the space charge field also predict it to be limited by only the maximum space charge field E_N for large external fields, instead of the smaller of E_N and the diffusion field E_d in cases where $E_0 = 0$.

6.7. References for Chapter 6

1. K. Sayano, A. Yariv, and R.R. Neurgaonkar, "Photorefractive properties of Cr-doped single crystal strontium barium niobate," *Proc. SPIE* **1148**, 7-11 (1989).

2. K. Sayano, A. Yariv, and R.R. Neurgaonkar, "Photorefractive gain and response time of Cr-doped strontium barium niobate," *Appl. Phys. Lett.* **55**, 328-330 (1989).

3. K. Sayano, A. Yariv, and R.R. Neurgaonkar, "Order of magnitude reduction of the photorefractive response time in rhodium-doped $Sr_{0.6}Ba_{0.4}Nb_2O_6$ with a dc electric field," *Opt. Lett.* **15**, 9-11 (1990).

4. G.A. Rakuljic, A. Yariv, and R.R. Neurgaonkar, "Photorefractive properties of undoped, Ce-doped, and Fe-doped single crystal $Sr_{0.6}Ba_{0.4}Nb_2O_6$," *Opt. Eng.* **25**, 1212-1216 (1986).

5. D. Rytz, B.A. Wechsler, R.N. Schwartz, C.C. Nelson, C.D. Brandle, A.J. Valentino, and G.W. Berkstresser, "Temperature dependence of photorefractive properties of strontium-barium niobate ($Sr_{0.6}Ba_{0.4}Nb_2O_6$)," *J. Appl. Phys.* **66**, 1920-1924 (1989).

6. M. Cronin-Golomb, G.A. Rakuljic, and A. Yariv, "Effect of temperature variation in photorefractive devices," *Proc. SPIE* **613**, 106-109 (1986).

7. K. Sayano, A. Yariv, and R.R. Neurgaonkar, "Enhanced photorefractive gain in Cr-doped strontium barium niobate with an external dc electric field," *J. Appl. Phys.* **67**, 1594-1596 (1990).

8. N.V. Kukhtarev, V.B. Markov, and S.G. Odulov, "Transient energy transfer during hologram formation in $LiNbO_3$ in external electric field," *Opt. Commun.* **23**, 338-343 (1977).

9. N.V. Kukhtarev, V.B. Markov, S.G. Odulov, M.S. Soskin, and V.L. Vinetski, "Holographic storage in electro-optic crystals. I. Steady state," *Ferroelectrics* **22**, 949-960 (1979).

10. N.V. Kukhtarev, "Kinetics of hologram recording and erasure in electro-optic crystals," *Sov. Tech. Phys. Lett.* **2**, 438-440 (1976).

11. G.A. Rakuljic and A. Yariv, "Photorefractive materials for optical computing and image processing," *Proc. SPIE* **881**, 146-149 (1988).

12. P. Yeh, "Fundamental limit of the speed of photorefractive effect and its impact on device applications and materials research," *Appl. Opt.* **26**, 602-604 (1987).

CHAPTER SEVEN

Applications of Photorefractive Materials

7.1. Introduction

Photorefractive materials such as $BaTiO_3$ and SBN have made possible a wide variety of devices and systems in the areas of phase conjugation, image processing, distortion correction, and computing. Some of these applications that have been developed in the past include beam amplification and cleanup, tracking novelty filters, bistable devices, optical oscillators, phase conjugate mirrors, thresholding devices, distortion correction, and limiters. In the following sections, experimental results of some specific applications in the areas of phase conjugation, distortion correction, one-way image transmission, thresholding using photorefractive materials, and electrically controlled photorefractive optical limiting developed in the course of this work will be discussed.

7.2. Optical phase conjugation

Optical phase conjugation, as described in Sec. 1.3, is a process of time reversal of an optical signal by generating the phase conjugate of it. Photorefractive materials have made possible phase conjugation using low power and with continuous wave sources instead of relying on methods requiring high power and usually pulsed lasers. In this section, the application of SBN as the nonlinear medium for self-pumped phase conjugation will be presented.

7.2.1. Four-wave mixing

Four-wave mixing was first proposed by R.W. Hellwarth for optical phase conjugation in nonlinear media.[1] The experimental configuration for four-wave

mixing is shown in Fig. 1-5, where the four waves that interact inside the nonlinear medium are given by

$$E_j(\mathbf{r},t) = \frac{1}{2}A_j(\mathbf{r}_j)e^{i(\omega_j t - \mathbf{k}_j\cdot\mathbf{r})} + c.c. \tag{7.1}$$

The pump beams for the system, waves 1 and 2, are counter-propagating with the same frequency, so their corresponding wavevectors can be given by $\mathbf{k}_1 = -\mathbf{k}_2$. Wave 4 is oriented along the z axis, so $\mathbf{k}_4 = -k\hat{\mathbf{z}}$. Wave 3 will then be the desired phase conjugate output. The nonlinear medium has a third-order nonlinear polarization given by[2]

$$\begin{aligned}\mathbf{P}^{(NL)}(\omega_3 = \omega_1 + \omega_2 - \omega_4) &= \chi^{(3)}A_1^{(\omega_1)}A_2^{(\omega_2)}A_4^{*(-\omega_4)} \\ &= \frac{1}{2}\chi^{(3)}A_1A_2A_4^*e^{i(\omega t + kz)} + c.c.\end{aligned} \tag{7.2}$$

Substituting into the nonlinear wave equation

$$\nabla\times\nabla\times\mathbf{E} + \frac{1}{c^2}\frac{\partial^2}{\partial t^2}\mathbf{E} = \frac{1}{c^2\epsilon}\frac{\partial^2}{\partial t^2}\mathbf{P}^{(NL)} \tag{7.3}$$

and using the slowly varying field approximation results in the coupled equations describing waves 3 and 4:

$$\begin{aligned}\frac{dA_3}{dz} &= i\frac{\omega}{2cn}\chi^{(3)}A_1A_2A_4^* = i\kappa^*A_4^* \\ \frac{dA_4^*}{dz} &= i\kappa A_3\,,\end{aligned} \tag{7.4}$$

where the complex coupling constant $\kappa^* = (\omega/2cn)\chi^{(3)}A_1A_2$. The solution of the coupled differential equations in Eqn. (7.4) for the boundary conditions $A_4 = A_4(0)$ at $z = 0$ and $A_3 = 0$ at $z = L$ gives the phase conjugate of $A_4(0)$ as the output wave 3 at $z = 0$:

$$A_3(0) = -i\left[\frac{\kappa^*}{|\kappa|}\tan(|\kappa|L)\right]A_4^*(0)\,, \tag{7.5}$$

with $A_4(L) = A_4(0)/(\cos|\kappa|L)$ at the $z = L$ output.

7.2.2. Passive phase conjugation

Passive phase conjugate mirrors, where the external pumping beams in the four-wave mixing scheme are eliminated, have been demonstrated. Some of these, including the linear mirror, semilinear mirror, and total internal reflection phase conjugate mirror, are illustrated in Figs. 1-6(a) - (c).

The linear mirror of M. Cronin-Golomb et al. uses beam coupling from the incident beam to generate the pump beams, as shown in Fig. 1-6(a).[3] The light oscillating in the cavity bounded by the two mirrors is used in place of the two counterpropagating pump beams in the four-wave mixing scheme. More recently, it was discovered that if the gain of the nonlinear medium is higher, one of the mirrors can be eliminated and the other substituted with a converging mirror, and the result is the semilinear mirror shown in Fig. 1-6(b).[4] This particular phase conjugate mirror configuration will be discussed later in an optical thresholding application.

An important simplification results when the nonlinear gain is high enough for the total internal reflection phase conjugate mirror to operate. The fanning effect from the large beam coupling effect, and the light oscillating in the cavity formed from total internal reflection inside the crystal, is used as the pump beams in this phase conjugate mirror of Feinberg.[5] Since there are no external optics, the device is completely self-contained. An added advantage of this scheme is that it is self-aligning, accepting a wide range of incidence angles.

7.2.3. Self-pumped phase conjugation using SBN

In phase conjugation and similar experiments, $BaTiO_3$ has been the material of choice not only because of its large electro-optic coefficients and therefore large

nonlinear effects, but also because of its commercial availability at that time. Self-pumped phase conjugation requires materials with high two-beam coupling gain, especially the total internal reflection phase conjugate mirror just described, so $BaTiO_3$, with its large r_{42} electro-optic coefficient of over 1600 pm/V, was a natural choice. This type of phase conjugate mirror has been widely used with $BaTiO_3$ as the nonlinear wave mixing medium. Prior experiments using $BaTiO_3$ have also shown that this type of mirror is self-starting. However, other ferroelectric materials such as Ce-doped SBN:75 and SBN:60 were also found to be suitable materials for this type of phase conjugate mirror.[6,7]

The configuration of the experiment is shown in Fig. 7-1, where the incident light, an expanded 514.5 nm Ar-ion laser output, was passed through the beamsplitter and focused down into the SBN cube, with an incidence angle of approximately 45°, or an internal orientation of about 72° with respect to the *c* axis. The phase conjugate reflection was picked off by the beamsplitter and directed towards the screen or detector for reflectivity measurements. For the initial reflectivity measurement, the lenses and transparency were removed and the simple Gaussian output of the laser was used to approximate a plane wave. The phase conjugate reflection was picked off by the beamsplitter and directed towards the detector.

Figure 7-2 shows the phase conjugate reflectivities, without correcting for Fresnel losses, of the SBN:75 and SBN:60 phase conjugate mirrors as a function of time to show the reflectivity and its buildup time to the steady state. The intensity of the beam incident on the crystal was approximately 1.5 W/cm^2. The data also shows that the two devices are self-starting, with start-up time delays of 5 to 10 sec for the SBN:75 and 10 to 20 sec for the SBN:60. A steady state reflectivity of 25% was achieved with the SBN:75:Ce crystal, which was comparable

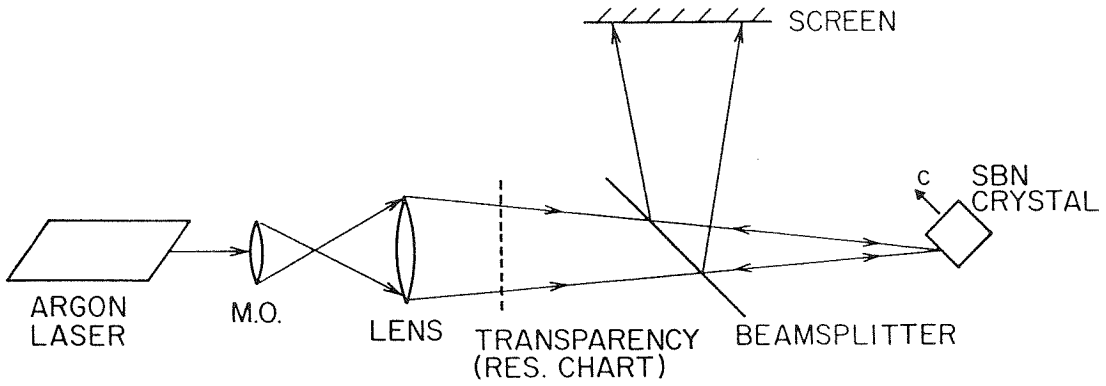

Fig. 7-1: Configuration of the self-pumped phase conjugate mirror using SBN used to study its reflectivity and distortion correcting properties.

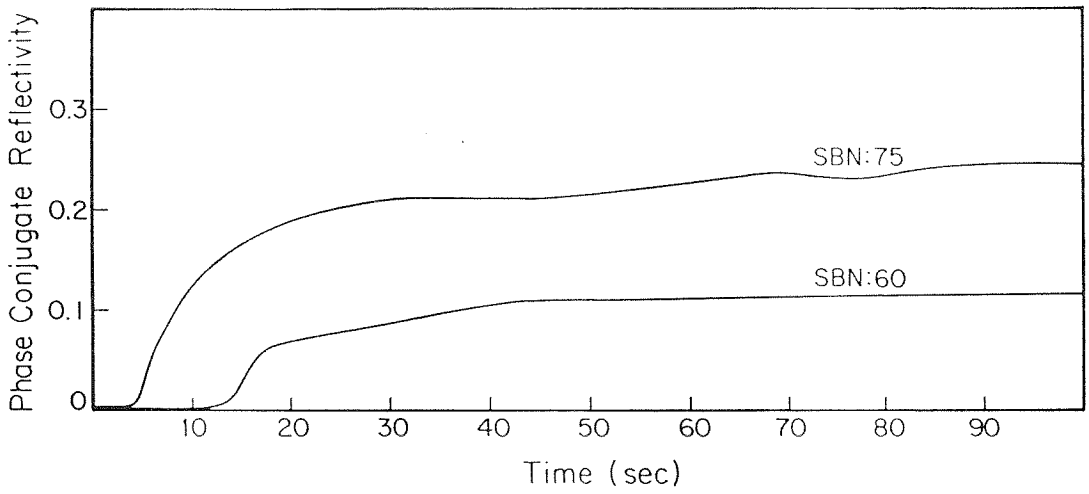

Fig. 7-2: Phase conjugate reflectivities as a function of time for the Ce-doped SBN:60 and SBN:75 phase conjugators. Pump beam power density was approximately 1.5 W/cm^2.

to the 30% reflectivity obtained previously with $BaTiO_3$ in this configuration.[5] A phase conjugate reflectivity of 12% was attained with the SBN:60:Ce sample under similar conditions. With both SBN crystals, once the steady state was attained, the phase conjugate output remained constant for periods up to 24 hours, the maximum duration of the experiment. A photograph of the SBN:75 phase conjugate mirror in operation is shown in Fig. 7-3, where the fanning off the incident beam that forms the pump beams is visible.

The distortion correction property of phase conjugate mirrors was demonstrated with the SBN phase conjugator by an imaging experiment where the SBN:75 crystal was used to phase conjugate a binary transparancy. An Air Force resolution chart was used as the transparancy, which was focused down into the SBN crystal by a converging lens. The phase conjugate reflection was projected onto a screen by the beamsplitter. Next, the experiment was repeated with a phase distorter, a randomly etched glass slide, placed between the beamsplitter and phase conjugate mirror as shown in Fig. 7-1. The results of this experiment are shown in Figs. 7-4(a) - (d). Fig. 7-4(a) shows the transparency illuminated by a plane wave from the laser. Its phase conjugate (without the distortion) is shown in Fig. 7-4(b). The image incident on the crystal is shown in Fig. 7-4(c), where the chart was distorted by the random phase modulator, rendering the image an unintelligible random illumination. However, since the phase conjugate image is the exact time-reversed wavefront reproduction of the resolution chart after passing through the distortion, the beam emerging from the distortion is the original undistorted image of the chart. This distortion correcting property of the SBN phase conjugate mirror is shown in Fig. 7-4(d). Also, as can be observed by comparing Figs. 7-4(c) and (d), the transparency was reproduced with good phase conjugate fidelity.

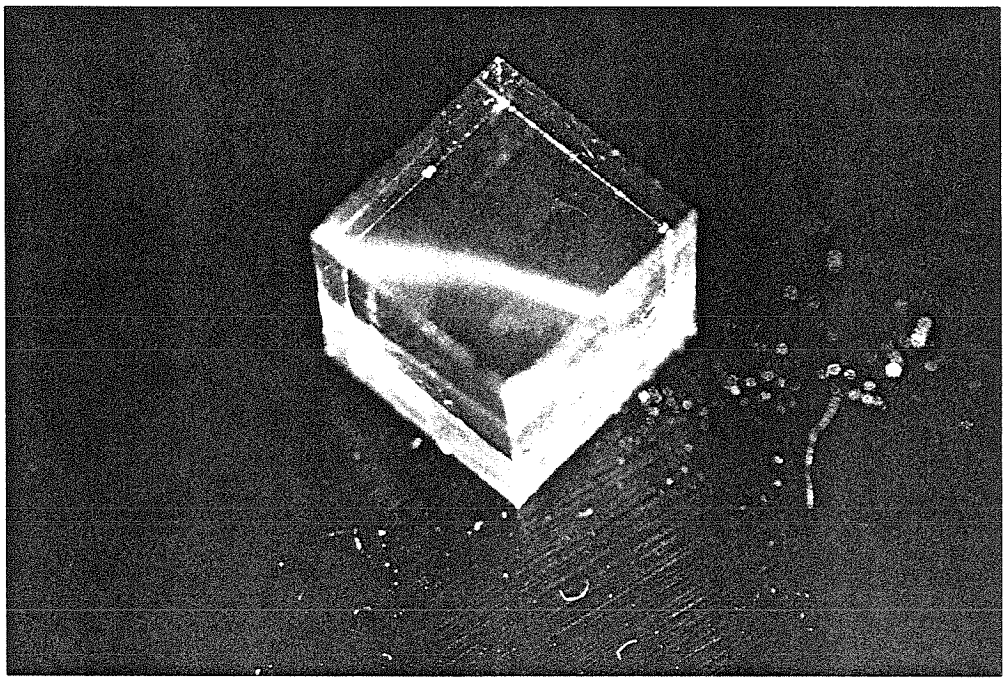

Fig. 7-3: Photograph of the self-pumped, total internal reflection phase conjugate mirror using Ce-doped SBN:75 in operation. The beam is incident on the lower right face of the crystal. Note that the fanning pattern off the incident beam which forms the pump beams is visible.

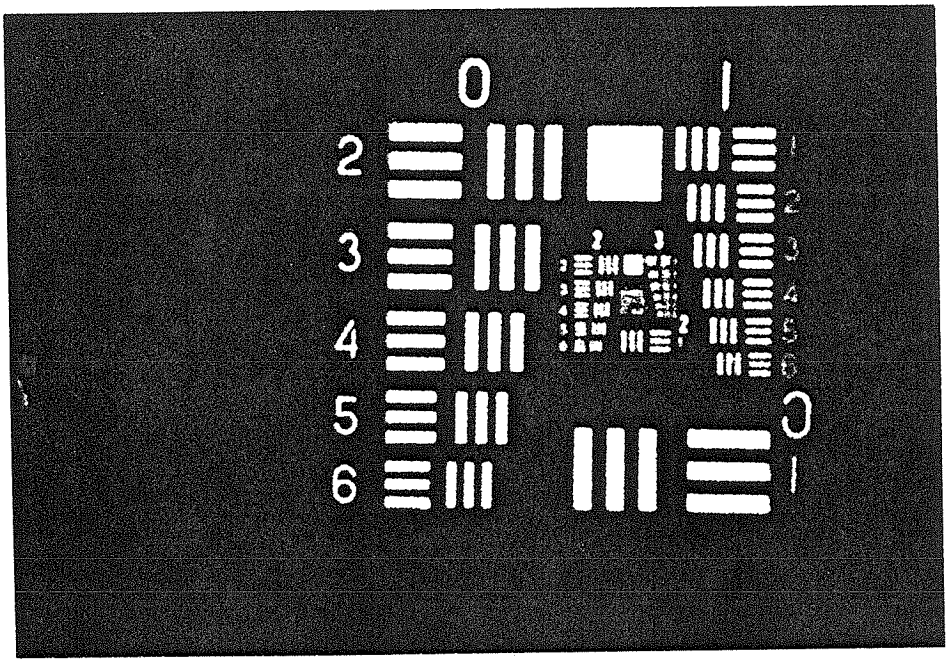

(a)

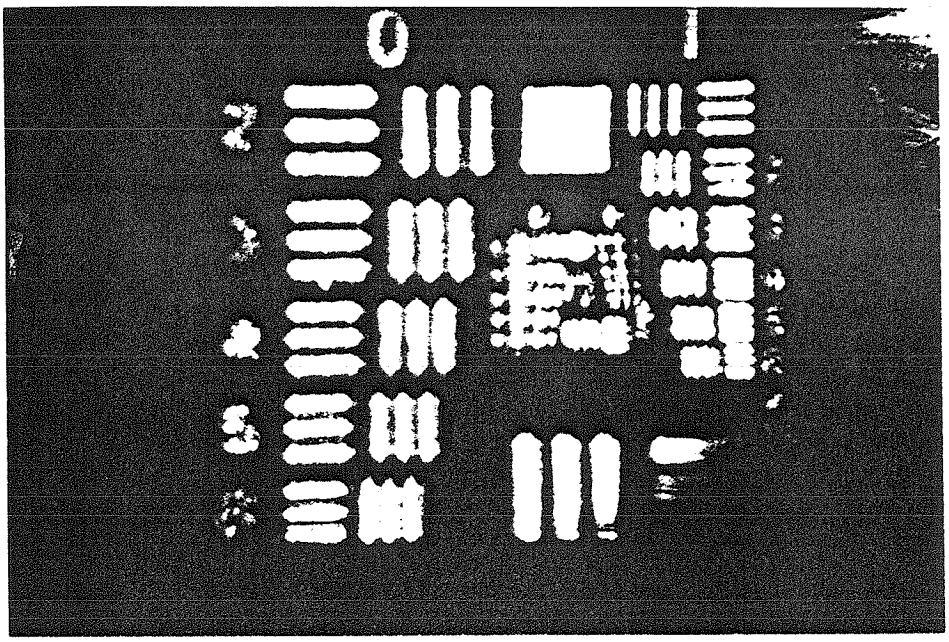

(b)

Fig. 7-4: Imaging experiment with the SBN self-pumped phase conjugate mirror: (a) Incident image of the Air Force resolution chart; (b) Phase conjugate image of the chart without the distortion.

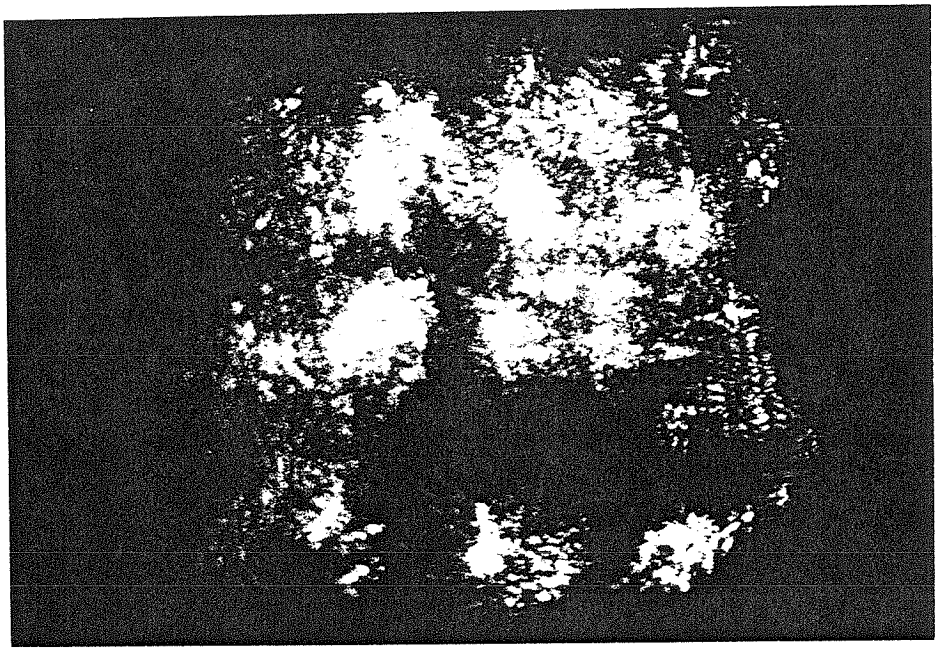

(c)

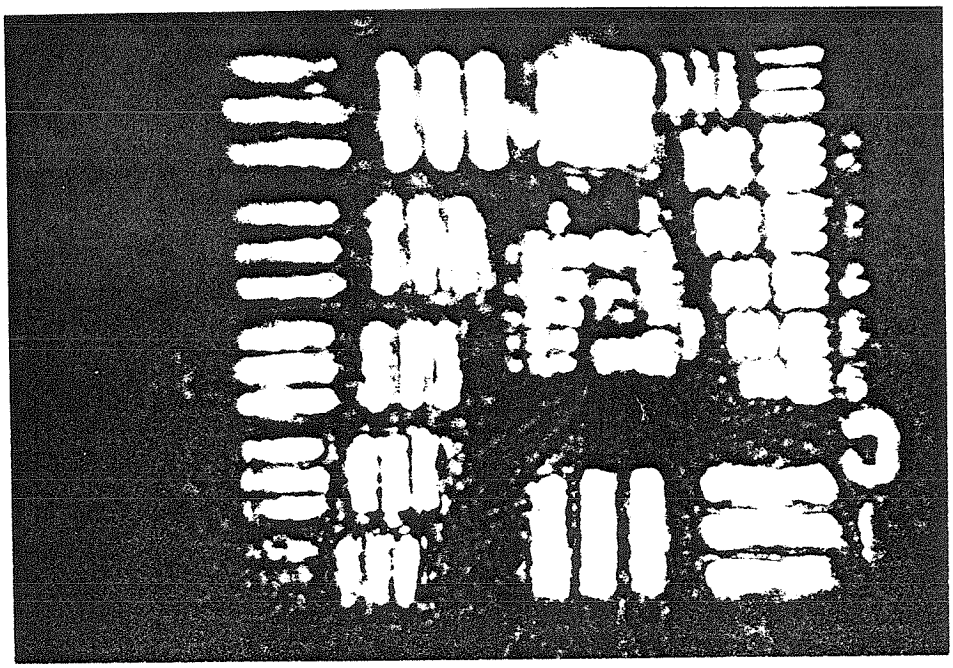

(d)

Fig. 7-4: Imaging experiment (continued): (c) Image of the chart with distortion; (d) Corrected image of the resolution chart, showing good phase conjugate fidelity.

The experiment was also repeated using other wavelengths, i.e., the 501.7, 496.5, 488, 476.5, and 457.9 nm lines of the Ar-ion laser, to demonstrate the ability of the SBN phase conjugate mirror to operate at a variety of wavelengths over its photorefractive range. Multicolor phase conjugation has also been successfully demonstrated by M. Cronin-Golomb et al. using the semilinear mirror with $BaTiO_3$ as the nonlinear medium.[8] In this experiment, some wavelength as well as angular dependence of the phase conjugate reflectivity was observed, which was not unexpected since the two-beam coupling constant is dependent on the grating period and hence the incidence angle. The wavelength dependence of the phase conjugate reflectivity arises from the explicit dependence of Γ on the wavelength as well as the wavelength dependence of linear absorption and donor and trap densities. The time response is affected through the characteristic response time t_0, photoionization cross section, recombination rate, and density of photoionizable donors being functions of wavelength.

In summary, a self-starting passive phase conjugate mirror using internal reflection has been successfully demonstrated using Ce-doped SBN as the nonlinear medium in place of $BaTiO_3$. The imaging and distortion correcting property of phase conjugation were shown as well with the SBN phase conjugate mirror. This configuration was also found to phase conjugate at higher Ar-ion laser wavelengths as well.

7.3. Distortion correction using phase conjugation

One of the first applications of optical phase conjugation was in correcting for phase distortions in optical signals. The time reversal property of phase conjugate mirrors enabled a distorted beam to have the superimposed wavefront distortions removed. There are two basic schemes to accomplish this. The simpler one is the

double pass system, where the source and detector are both in the same half plane separated by the distorter. The other is one-way imaging, which requires only a single pass through the distorter, where the source and detector are in opposite half planes separated by the distorter.

7.3.1. Double pass distortion correction

Removal of a distortion from an optical signal has been demonstrated using phase conjugation.[5,9] This has been done by retracing the distorted image bearing signal back through the distorter using a phase conjugate mirror in a double-pass configuration. This was the method used in the imaging experiment in Sec. 7.2.3, where the original image of the transparancy was retrieved after being distorted by the random phase modulator.

In the configuration of Fig. 7-1, the image of the transparancy $T(x,y)$ is passed through a phase distortion with a phase factor $e^{i\varphi(x,y)}$. The reflected signal off the phase conjugate mirror would then be $T^*(x,y)e^{-i\varphi(x,y)}$, neglecting Fresnel diffraction, so after passing through the distorter a second time in the reverse direction, the phase factor is cancelled.

7.3.2. One-way image transmission through a distortion

In cases where the source and receiver are separated by the distorting medium, a one-way image transmission system is necessary to image the signal through the distorter. Several single-pass schemes, where the signal passes through the distorter only once, have been suggested.[10–12] Recently, a further simplification of this method, where the receiver does not need access to the space beyond the distorter has been demonstrated by imparting nearly the same distortion onto both the signal beam and a separate reference beam, and then combining them in a degenerate four-wave mixing configuration.[13] In this method, however, only

a slowly spatially varying phase distortion can be corrected since the two beams are spatially separated at the distorter. The following one-way image transmission method solves this problem by using two orthogonally polarized beams traveling exactly the same path through the distorter.[14]

The method relies on the nonlinear polarization in a four-wave mixing setup to eliminate the distortion phase factor $e^{[i\varphi(x,y)]}$ at the nonlinear medium and therefore reconstruct the original information. Consider the photorefractive four-wave mixing process in the crystal as shown in Fig. 1-5. The index change of the crystal due to the optical fields is given by[15]

$$\Delta n \propto \frac{\mathbf{E}_1 \cdot \mathbf{E}_3^*}{|\mathbf{E}_1|^2 + |\mathbf{E}_3|^2} \tag{7.6}$$

where $\mathbf{E}_1$ is the reference beam and $\mathbf{E}_3$ is the signal beam possessing the "distorted" image information. Then, the nonlinear polarization $\mathbf{P}_{NL}$ arising from the four-wave mixing is proportional to

$$\begin{aligned} \mathbf{P}_{NL} &\propto \Delta n \mathbf{E}_2 \\ &\propto E_2 E_3^* \text{ if } |\mathbf{E}_1| \gg |\mathbf{E}_3| \\ &\propto \exp[i(\varphi + kz)][\mathbf{A}^*(x,y)] e^{[-i(\varphi+kz)]} \mathbf{E}_2 \end{aligned} \tag{7.7}$$

where $\mathbf{E}_2$ is the uniform readout beam propagating in the opposite direction to $\mathbf{E}_1$. Therefore, the phase distortion superimposed on the signal can be eliminated at the crystal if the reference beam has the same distorted phase factor $e^{[i\varphi(x,y)]}$ as that of the signal beam impressed at the distorter and that phase factor is preserved at the crystal.

The setup for the system is shown in Fig. 7-5. An argon ion laser operating at $\lambda = 514.5$ nm was used as a light source. One of the two beams leaving the beamsplitter BS_2 is converted to an orthogonal (vertical) polarization by the $\lambda/2$ plate. One becomes the signal beam and the other serves as the reference. The

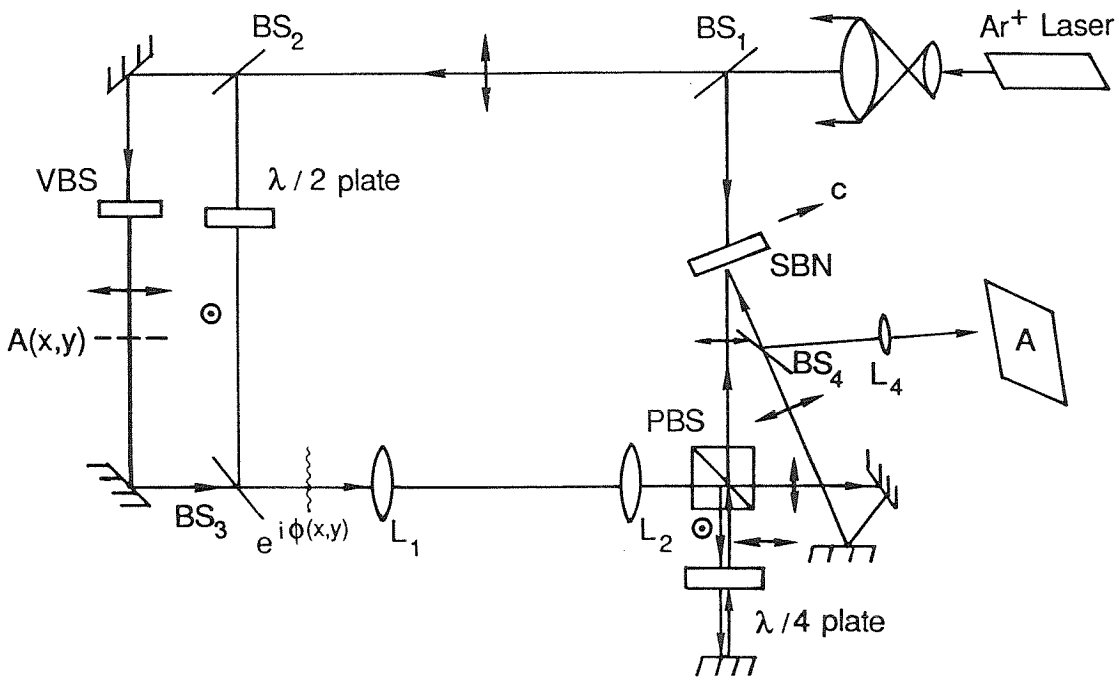

Fig. 7-5: Experimental setup for the passive one-way image transmission system using orthogonally polarized signal and reference beams. The variable beamsplitter (VBS) was used to vary the intensity ratio of the signal and reference. The $\lambda/2$ plate rotates the polarization of the reference to the vertical direction, and the two passes through the $\lambda/4$ plate restores it to horizontal polarization so the two beams can write the grating. The readout beam was picked off from the same argon-ion laser source, but can be from a different laser as well.

two are recombined at BS_3 and both pass through the phase distorter, which is an acid-etched glass. This way, both beams will undergo the same phase distortion, insuring that the distorted phase information carried by the two beams will be identical. When two spatially separate beams are used, as is the case in Ref. [13], it is more difficult to insure that this occurs.

As previously mentioned, it is necessary to avoid the phase mixing due to Fresnel diffraction during propagation and preserve the distorted phase factor, $e^{[i\varphi(x,y)]}$ at the nonlinear medium, in this case a 10 mm × 10 mm × 1 mm photorefractive strontium barium niobate (SBN) crystal. This necessitates the imaging of the distorter onto the crystal. In addition, the distorter must be thin enough to fall within the depth of focus of the imaging system. In this experiment, the telecentric imaging geometry was used to circumvent unwanted wavefront curvatures at the image plane.[16] Two lenses of focal length f = 40 cm were used, with the lenses spaced 80 cm apart. The distances from the distorter to lens L_1 and from lens L_2 to the crystal were both 40 cm.

After passing through the lenses, the two beams are separated by the polarizing beamsplitter (PBS) and the vertically polarized component is rotated again by 90° in a double-pass through the $\lambda/4$ plate so the two beams can write the "distortion-free" grating in the crystal by perfect cancellation of $e^{[i\varphi(x,y)]}$. The beam intensities were chosen as I_{ref}=16 mW/cm^2 and I_{sig}=4 mW/cm^2, so that the gratings (Δn), and also $\mathbf{P}_{NL}$, in the crystal are proportional to E_3^* (see Eqs. (1) and (2)). The second mirror is necessary in the leg that is transmitted through the PBS so that the image is properly oriented. After the grating is written, a plane wave directed from behind the crystal and Bragg-matched with the gratings is used for readout, and the reconstructed signal picked off by BS_4 is imaged onto the screen by lens L_3. Note that in order to create the photorefractive gratings,

the readout beam need not be coherent with the writing beams.

The results of the distortion correcting capability of this experiment are shown in Fig. 7-6. Fig. 7-6(a) is the original image, and 7-6(b) is the image after the distorter. Figs. 7-6(c) and 7-6(d) are the output images without and with the distorter, respectively. It can be seen from Fig. 7-6(d) that the system has reconstructed the original image from the given information, and that the image quality with Fig. 7-6(c) is roughly the same.

In summary, a new method for passive one-way image transmission through a distorting medium using two orthogonally polarized beams, one carrying the signal and the other probing the distortion, has been demonstrated. These were used to write the distortion-free grating in the crystal for the reconstruction of the original image by the independent readout beam. This procedure, although valid only for phase distortions in isotropic media, is useful in instances where it is not possible to retransmit the phase conjugate signal back through the distorter in a double-pass configuration. One final note is that a single, circularly (or elliptically) polarized beam can also be used as the signal and reference beams in the present system instead of preparing the beams separately. In this case, however, the transparency as an input is limited to a binary one.

7.4 Thresholding using photorefractive materials

Thresholding is a nonlinear operation that has the potential for widespread applications in optical computing and associative memories in selecting the strongest signal from a number of inputs by passing only those above a certain intensity. The ideal thresholding function is the step function, where

$$F(I) = \begin{cases} 0 & \text{for } I < I_{th}; \\ 1 & \text{for } I \geq I_{th}. \end{cases} \tag{7.8}$$

Moreover, a variable thresholding level I_{th} is desired, with some mechanism for

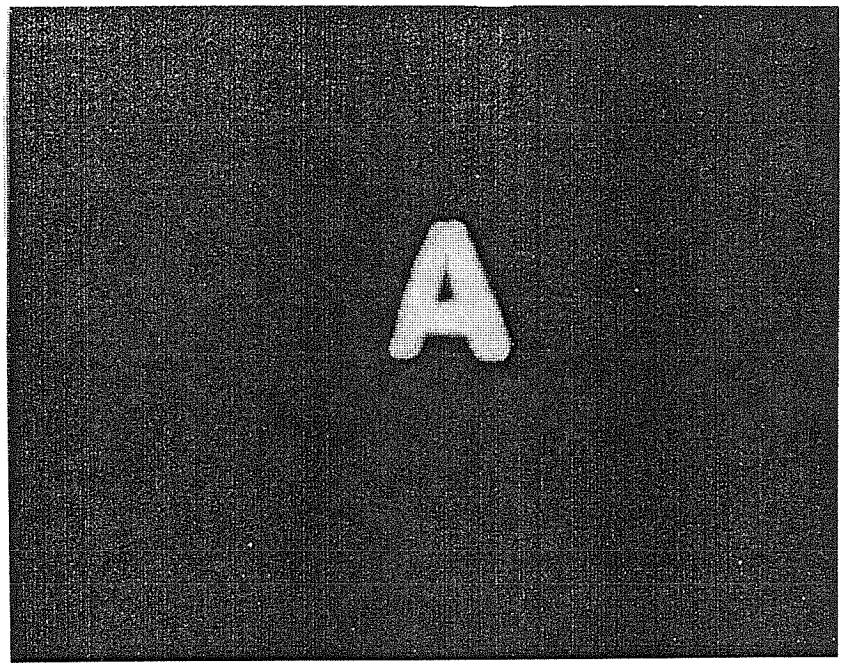

(a)

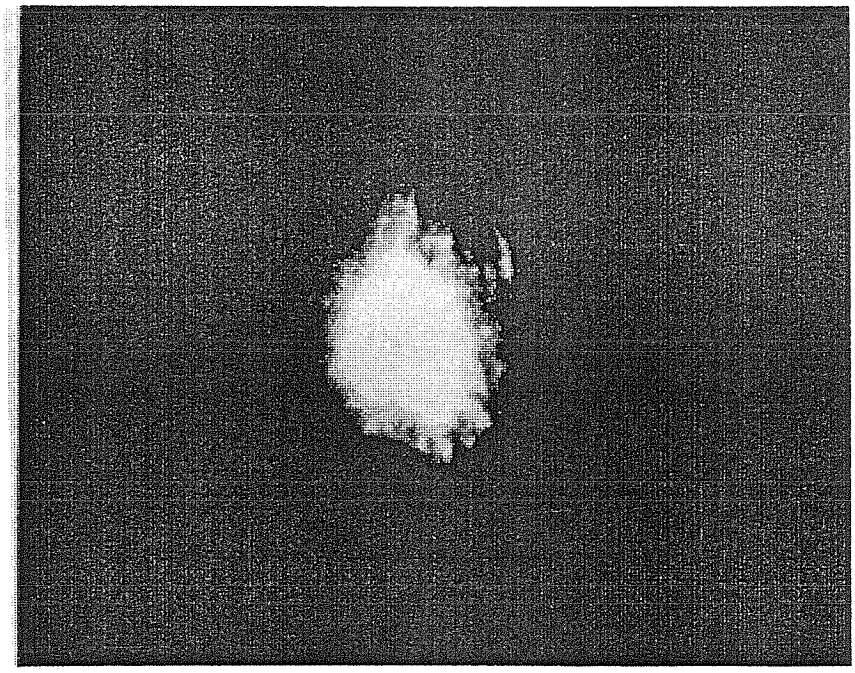

(b)

Fig. 7-6: One-way image transmission experiment: (a) Original image transparency; (b) Image after passing through the distorter.

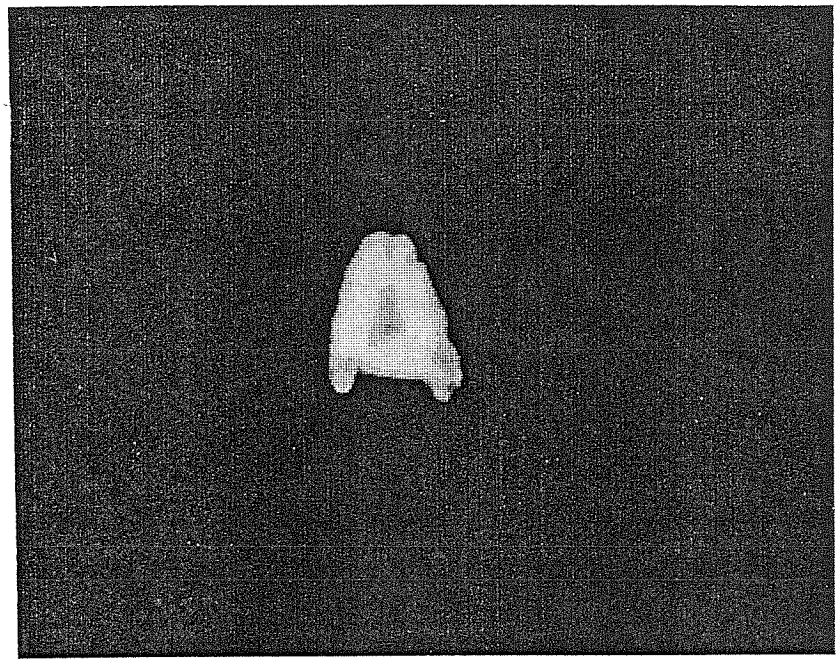

(c)

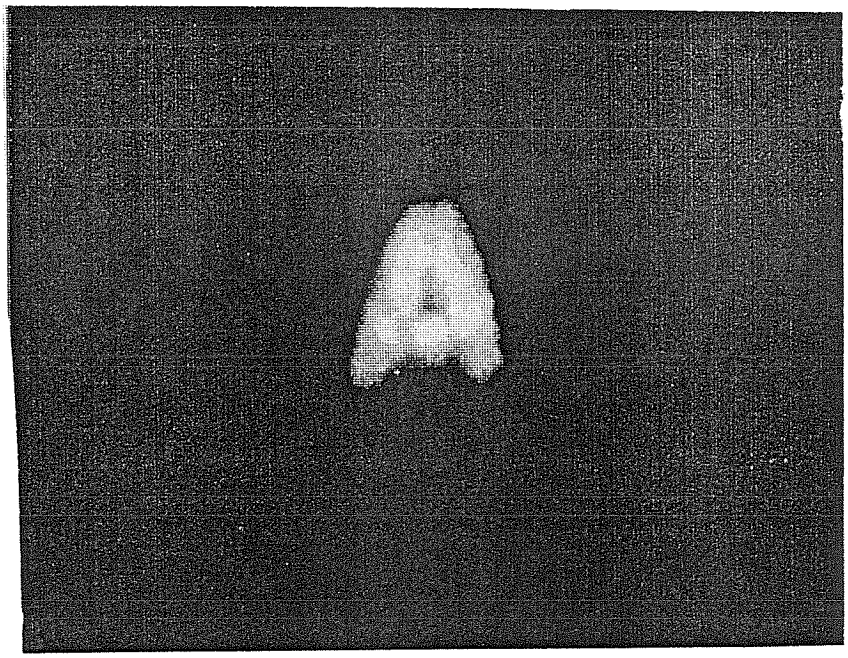

(d)

Fig. 7-6: Results showing the distortion correction capability of the system: (c) Phase conjugate image without the phase distorter; (d) Corrected image as viewed on the screen.

control of the thresholding level.

7.4.1. Thresholding methods

Photorefractive phase conjugate mirrors have been used as nonlinear thresholding devices by using background illumination, semi-self-pumped phase conjugation, and optical bistability.[17–20] The background illumination and semi-self-pumped phase conjugation schemes of M. Cronin-Golomb et al. and M.B. Klein et al. were self-pumped phase-conjugate mirrors which ideally generated the phase conjugate of the incident beam if the intensity of the beam was above a threshold I_{th} and produced no output if it was less than I_{th}. Both of these configurations rely on an external reference beam that determines the threshold intensity of the device through depression of the effective two-beam coupling constant by partial grating erasure.[17,18]

Another recently demonstrated method for obtaining phase-conjugate thresholding relies on a different method for depressing the coupling constant to set the thresholding level.[21] This method used a moving grating inside the photorefractive crystal by Doppler-shifting one of the beams writing the gratings in the semilinear passive phase conjugate mirror setup. The thresholding level was set by the dependence of the photorefractive response time on the incident beam intensity, which in turn varies the effective coupling constant γl.

7.4.2. The thresholding semilinear phase conjugate mirror

The basic semilinear phase-conjugate mirror configuration has been described in several previously reported works and is illustrated in Fig. 1-6(b) as used in this experiment. This is a passive, or self-pumped, device, relying only on the incident beam to generate the phase conjugate of that beam. Light scattered and amplified by the fanning effect is reflected back into the crystal by the external

converging mirror. The grating in the crystal is formed by the light interference pattern between this reflected fanning beam and the incident beam. This mirror is self-starting by itself, although there is a time delay of several seconds for the pump beam reflected off the mirror to write a grating and the phase conjugate output to build up to the steady state.

The phase of the light interference pattern is a direct function of the optical path difference of the two beams, so the grating can be translated by ramping the phase of the light reflected by the external mirror. In this experiment, this was done by varying continuously the optical path length traveled by the reflected fanning beam. The external mirror was mounted on a piezoelectric micrometer, and a high voltage ramp from a function generator amplified by a high voltage amplifier was applied to the device to translate it at a constant velocity. When the external mirror was moved, the reflected light was Doppler-shifted by $\delta\omega$, causing the interference pattern in the crystal to move with a velocity

$$v = \frac{c\delta\omega}{2\omega\sin(\theta/2)}\,, \tag{7.9}$$

where θ is the angle between the incident and fanning beams, so that the grating period is $\lambda_g = \lambda/[2\sin(\theta/2)]$.

In a photorefractive crystal, the light interference pattern creates a corresponding local change in index, whose transient behavior is characterized by an exponential time constant τ. As derived in Ch. 2, the response time, as a function of the experimentally controlled parameters for the case of no applied fields, is given by

$$\begin{aligned}\tau =& \frac{\hbar\omega N_{A,C}^{-}}{s_e I_0 N_D}\left(\frac{E_\mu + E_d}{E_N + E_d}\right) \\ =& \tau(\lambda_g, \lambda, T, I_0)\,,\end{aligned} \tag{7.10}$$

where T is the temperature, λ is the wavelength of the incident light, I_0 is the

total intensity,

$$E_\mu = \frac{\lambda_g \gamma N_{A,C}^-}{2\pi\mu},$$
$$E_N = \frac{eN_{A,C}^-}{\epsilon K} = \frac{\lambda_g e N_{A,C}^-}{2\pi\epsilon}, \text{ and}$$
$$E_d = \frac{2\pi k_B T}{\lambda_g e}.$$

The photorefractive coupling constant Γl, which for the stationary grating case is a constant, is also a function of the experimentally variable parameters, and is given by

$$\Gamma l = (\Gamma_0 l) F(I, \tau, v), \tag{7.11}$$

where Γ_0 is the coupling constant for stationary gratings, I is the total intensity of the incident beam plus any background erase beam, τ is the time constant of the crystal, and v is the velocity of the light interference pattern inside the crystal. Specifically, this dependence is given by[22]

$$\begin{aligned} \Gamma l \propto \Delta n_{\text{grating}} &\propto \left(\frac{\Delta n}{1+\alpha I}\right)\left(\frac{1}{1+i\frac{2\pi v\tau}{\lambda_g}}\right) \\ &\propto \frac{1}{1+i(\tau\delta\omega)} \end{aligned} \tag{7.12}$$

for the case of no external erase beam. For moving gratings when $\delta\omega \neq 0$, an increase in intensity I results in a decreased response time τ, therefore causing the coupling constant Γl to increase. The real part of γl is that which determines the thresholding level.[3]

The reflectivity of a semilinear phase conjugate mirror is given by[3]

$$R = \left\{ \frac{M^{1/2} + [a^2(1+M) - 1]^{1/2}}{M + 2 - M^{1/2}[a^2(1+M) - 1]^{1/2}} \right\}, \tag{7.13}$$

where M is the reflectivity of the external mirror, and a is related to the coupling constant γl by

$$\tanh\left(-\frac{1}{2}\gamma l a\right) = a. \tag{7.14}$$

There exists a threshold value $(\gamma l)_{th}$ of the coupling constant in Eqn. (7.13), which is defined by

$$a_{th}^2 = \tanh^2\left[-\frac{1}{2}(\gamma l)_{th} a_{th}\right] = \frac{1}{1+M} \tag{7.15}$$

for which $R_{th} = M/(M+2)^2 \approx 1/9$ for $M \approx 1$ but can be made significantly smaller by choosing $M < 1$. The result is that R will be high for γl above the threshold $(\gamma l)_{th}$, while R approaches zero for γl below the threshold, where γl is a function of τ, which iteself is a function of I, for a fixed $\delta\omega$. Therefore, R will be a nonlinear function of I, with $R = 0$ for $I < I_{th}$.

If the external mirror is stationary, the effective coupling constant will be above threshold, the grating will build up after some finite time interval, and the semilinear mirror will produce a phase conjugate output. As the grating velocity increases, the effective coupling constant will decrease until it falls below the threshold necessary for the semilinear mirror to maintain a phase conjugate reflection. For a fixed grating velocity, if the intensity is below I_{th}, the time response of the crystal will be too slow to keep up with the moving gratings. If the intensity is above I_{th}, then the response of the crystal is fast enough and the photorefractive effect can keep up with the gratings, resulting in $\gamma l > (\gamma l)_{th}$ and a phase conjugate signal being reflected from the semilinear mirror.

Figure 7-7 shows the reflectivity of the semilinear mirror as a function of the incident power of the unexpanded Gaussian beam from an Ar-ion laser. The piezoelectric micrometer was driven by the ramp generator over a distance of 4 μm at velocities ranging from 18.0 to 39.2 nm/sec. With no mirror motion, the threshold was at $I = 2$ mW. This nonzero value was observed previously and has been attributed to the decay of the gratings due to dark conductivity of the material.[23] As the mirror velocity was increased, the threshold level I_{th} necessary for a phase conjugate output shifted to higher intensities. With the threshold

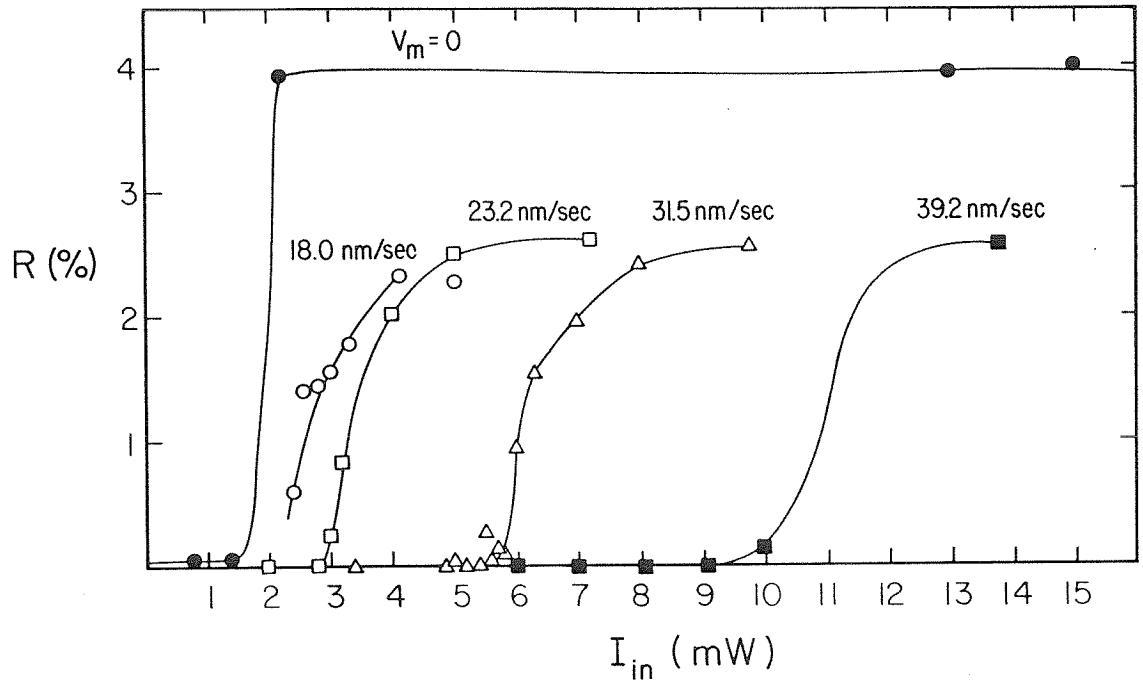

Fig. 7-7: Reflectivity as a function of beam intensity for the thresholding semilinear phase conjugate mirror.

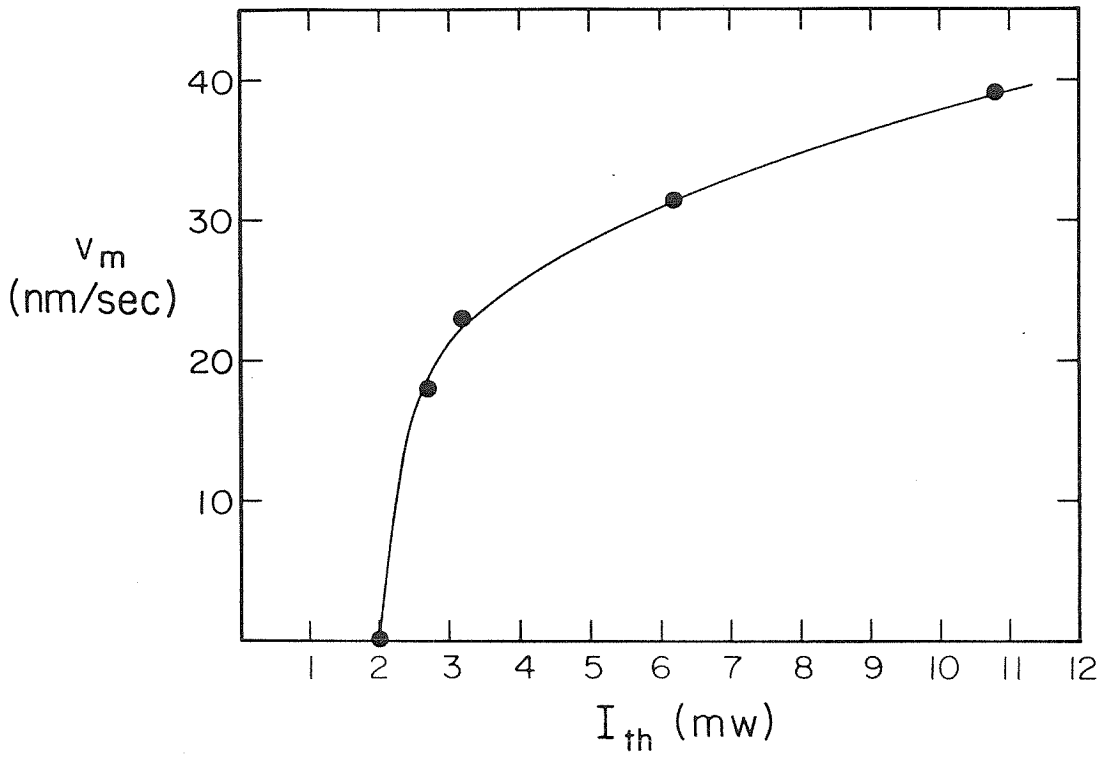

Fig. 7-8: Thresholding level as a function of grating velocity.

intensity defined somewhat arbitrarily as I_{th} such that $R(I_{th} = \frac{1}{2}R_{max})$, I_{th} as a function of mirror velocity v is shown plotted in Fig. 7-8, where the lines are guides to the eye.

This device has potential applications in optical associative memories in which it is necessary to phase conjugate selectively on the stronger modes among many in an optical resonator. It also has potential applications in optical signal processing and optical switching.

In summary, a new method of obtaining optical thresholding in a passive semilinear phase conjugate mirror has been demonstrated. This method relies on changing the effective coupling constant as a result of grating motion in the photorefractive medium introduced by the motion of the external mirror, which Doppler shifts the reflected beam, and on the dependence of the photorefractive response time on the incident beam intensity. The threshold intensity I_{th} can be selected by varying the Doppler shift, which in turn is a function of the translation velocity of the external mirror.

7.5. Optical limiting

Many of the previous examples relied on the amplification effect of two-beam coupling. However, there is another set of applications based on deamplification through two-beam coupling, which up until now has been treated as an undesired effect. The deamplification of the pump beam can be used in configuring coherent beam attenuators.

7.5.1. Objective of optical limiting

The primary objective of optical limiting is attenuating intense coherent radiation, while allowing incoherent, low intensity light to be transmitted. Such devices are useful in sensor protection from intense laser illumination. Protection

of eyesight may be another possible application; however, with current materials, the total energy transmitted is still orders of magnitude above the damage threshold. However, photorefractive materials provide an interesting starting point since they (1) respond only to coherent light, and (2) the response time of the device is inversely proportional to the intensity, so higher intensities would result in faster response and less energy allowed to be transmitted. The goal, therefore, is to have high gain materials with as fast a response time as possible. Unfortunately, most photorefractive materials, including those studied in Ch. 5 and 6, satisfy either of these criteria but not both.

7.5.2. Possible methods

Phase conjugate mirrors, photorefractive oscillators, and beam intensity depletion through the fanning effect in photorefractive crystals have been used to demonstrate optical limiting, as shown in Fig. 7-9(a) by M. Cronin-Golomb and A. Yariv.[24] The idea behind using the phase conjugate mirror is to reflect as much of the beam energy as the phase conjugate reflection as possible. The photorefractive oscillator can also be used, diverting much of the beam energy into the resonator mode. Each of these has the advantage of acting only on coherent radiation and having its response time decrease with intensity.

The fanning limiter is the simplest method, as shown in Fig. 7-9(b). This is simply a high gain photorefractive material oriented such that the fanning effect deflects the beam energy away from the axis of propagation. For incoherent light, the limiter acts simply as an optical element. For strong coherent light, self-induced beam fanning from scattered light inside the material builds up until the beam power is diverted into the fanning pattern, depleting energy from the transmitted beam. A limiter such as this can be simply built into an optical system

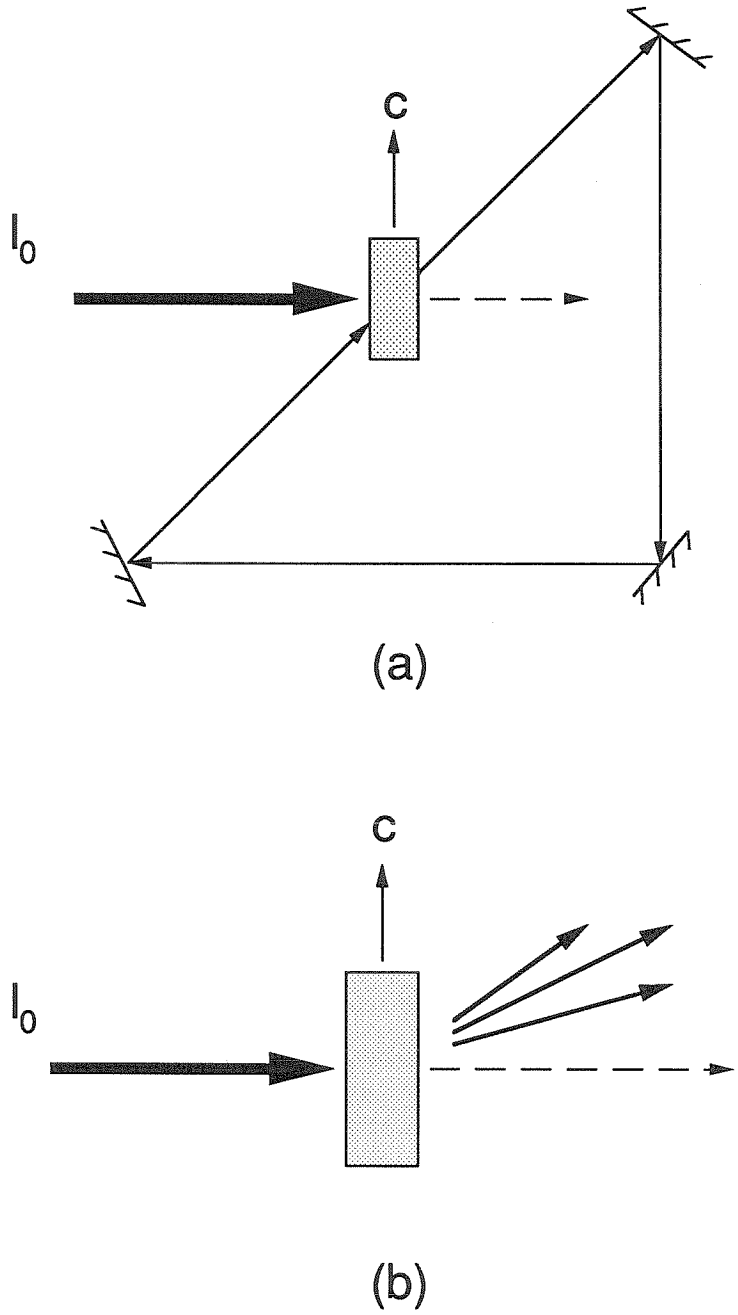

Fig. 7-9: Possible thresholding methods using photorefractive materials – (a) A photorefractive oscillator as a thresholding device; (b) The fanning optical limiter, where pump depletion due to the fanning effect is used to attenuate the beam.

as part of the front element, which remains inactive until illuminated by a strong, coherent beam that starts forming gratings in the material.

7.5.3. Enhanced optical limiters

An optical limiter ideally should have high gain and fast response time in order to cut down the amount of energy transmitted as much as possible. High gain should be the overriding consideration, however, since the attenuation goes as an exponential,

$$I(\ell) = I(0)e^{-\Gamma\ell}. \tag{7.16}$$

This makes gain enhancement an overriding consideration in order to get as much attenuation as possible.

One application of electric field enhancement of the photorefractive gain is in improving the effectiveness of optical limiters.[25] Since the exponential nature of beam coupling in photorefractive crystals makes a factor of two increase in Γ of major importance in such applications, this method is of particular interest since the goal of optical limiting is to have as large a coupling constant as possible. The enhancement of the photorefractive gain using an applied field has been achieved with minimal penalty in the response time of the crystal, which makes this technique useful for optical limiting applications.

To determine the effectiveness of optical limiters using an external field to increase its gain, the 0.016 wt. % Cr-doped SBN:60 crystal was used to attenuate a strong laser beam through the fanning effect. The transmitted beam intensity was measured in real time for applied fields of 0 to 10 kV/cm. As shown in Fig. 7-10(a), as the fanning gratings build up to their steady state, energy is coupled away from the incident beam. For higher coupling constants as the field was increased, this effect becomes much larger.

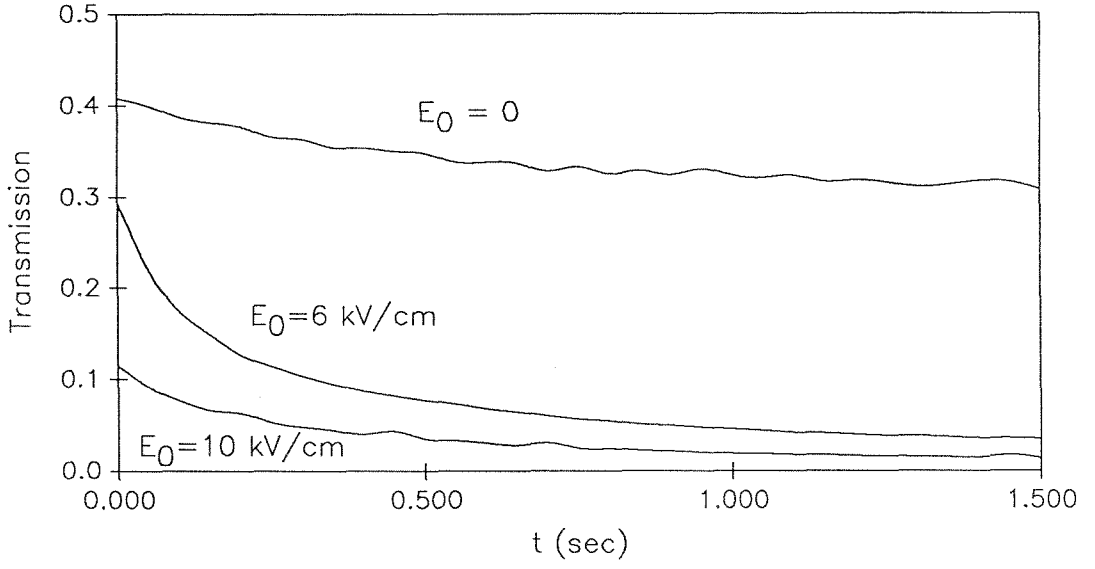

(a)

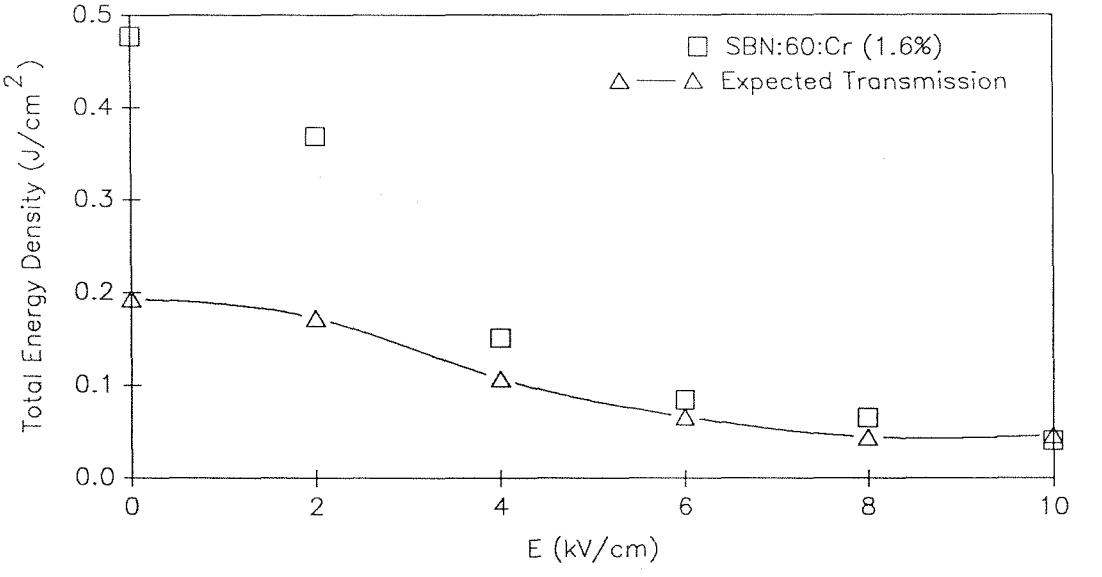

(b)

Fig. 7-10: Optical limiting using SBN:60:Cr – (a) Transmitted intensity for $E_0 = 0$ to $E_0 = 10$ kV/cm; (b) Total transmitted energy through the fanning optical limiter using SBN:60:Cr.

Figure 7-10(b) shows the total transmitted energy of a 0.5 W/cm^2, 514.5 nm Ar-ion laser beam through the Cr-doped SBN:60 crystal over a fixed period of 3 sec, or approximately six exponential time constants, which was obtained by numerically integrating the transmitted intensity over time. The model used to analyze the fanning limiter is given by

$$\text{Energy} = \int_0^T I(t)dt = I(0)\int_0^T e^{\Gamma(t)\ell}dt\,, \tag{7.17}$$

where $\Gamma = \Gamma_0(1 - e^{-t/\tau})$ and $T = 3$ sec for this particular case. Plotted with the experimental points in Fig. 7-10(b) are the theoretical values determined by substituting experimentally obtained values of Γ_0 and τ at each value of E_0 into the second integral of Eqn. (7.17) and numerically integrating from 0 to T.

The device configuration used here can also be considered as a field-controlled optical attenuator, since the attenuation is a function of E_0 through Γ and τ. Electrical control of gain and response time, in addition to reducing the total transmitted energy through gain enhancement or response time reduction, also introduces an element of control of this device.

To summarize, enhancement of the photorefractive two-beam coupling constant in Cr-doped SBN by applying an external dc field has been used to improve the performance of photorefractive "fanning" optical limiters. By increasing the gain of Cr-doped SBN:60, the increased attenuation of the incident beam due to beam energy depletion reduced the total transmitted energy by more than a factor of five.

7.6. References for Chapter 7

1. R.W. Hellwarth, "Generation of time reversal wavefronts by nonlinear refraction," *J. Opt. Soc. Am.* **67**, 1-3 (1977).

2. A. Yariv, "Phase conjugate optics and real-time holography," *IEEE J. Quantum Electron.* **QE-14**, 650-660 (1978).

3. M. Cronin-Golomb, B. Fischer, J.O. White, and A. Yariv, "Passive (self-pumped) phase conjugate mirror: Theoretical and experimental investigation," *Appl. Phys. Lett.* **41**, 689-691 (1982).

4. M. Cronin-Golomb, B. Fischer, J. Nilsen, J.O. White, and A. Yariv, "Laser with dynamic holographic intracavity distortion correction capability," *Appl. Phys. Lett.* **41**, 219-220 (1982).

5. J. Feinberg, "Self-pumped, continuous-wave phase conjugator using internal reflection," *Opt. Lett.* **7**, 486-488 (1982).

6. K. Sayano, G.A. Rakuljic, A. Yariv, and R.R. Neurgaonkar, "Self-starting, passive phase conjugation using internal reflection in Ce-doped strontium barium niobate," paper PD-11, Optical Society of America Annual Meeting, Seattle, WA (1986).

7. G.A. Rakuljic, K. Sayano, A. Yariv, and R.R. Neurgaonkar, "Self-starting, passive phase conjugate mirror with Ce-doped strontium barium niobate," *Appl. Phys. Lett.* **50**, 10-12 (1987).

8. M. Cronin-Golomb, S.K. Kwong, and A. Yariv, "Multicolor passive (self-pumped) phase conjugation," *Appl. Phys. Lett.* **44**, 727-729 (1984).

9. D.M. Pepper and A. Yariv, "Compensation for phase distortions in nonlinear media by phase conjugation," *Opt. Lett.* **5**, 59-60 (1980).

10. A. Yariv and T.L. Koch, "One-way coherent imaging through a distorting

medium using four-wave mixing," *Opt. Lett.* **7**, 113-115 (1982).

11. B. Fischer, M. Cronin-Golomb, J.O. White, and A. Yariv, "Real-time phase conjugate window for one-way optical field imaging through a distortion," *Appl. Phys. Lett.* **41**, 141-143 (1982).

12. J. Feinberg, "Imaging through a distorting medium with and without phase conjugation," *Appl. Phys. Lett.* **42**, 30-32 (1983).

13. K.R. MacDonald, W.R. Tompkin, and R.W. Boyd, "Passive one-way aberration correction using four-wave mixing," *Opt. Lett.* **13**, 485-487 (1988).

14. K. Sayano, Y. Tomita, and A. Yariv, "One-way image transmission through distorting media using orthogonally polarized beams and phase conjugation," unpublished.

15. S.K. Kwong, M. Cronin-Golomb, and A. Yariv, "Oscillation with photorefractive gain," *IEEE J. Quantum Electron.* **QE-22**, 1508-1523 (1986).

16. W.T. Welford, "Speckle in images," *J. Opt. Soc. Am.* **66**, 1172-1174 (1976).

17. M. Cronin-Golomb and A. Yariv, "Semi-self-pumped phase-conjugate mirrors," *Opt. Lett.* **12**, 714-716 (1987); M. Cronin-Golomb and A. Yariv, "Applications of a semi-self-pumped phase conjugate mirror," *J. Opt. Soc. Am. A* **3**, P16 (1986).

18. M.B. Klein, G.J. Dunning, G.C. Valley, R.C. Lind, and T.R. O'Meara, "Imaging threshold detector using a phase-conjugate resonator in $BaTiO_3$," *Opt. Lett.* **11**, 575-577 (1986).

19. S.K. Kwong, M. Cronin-Golomb, and A. Yariv, "Optical bistability and hysteresis with a photorefractive self-pumped phase conjugate mirror," *Appl. Phys. Lett.* **45**, 1016-1018 (1984).

20. S.K. Kwong and A. Yariv, "Bistable oscillators with a self-pumped phase-

conjugate mirror," *Opt. Lett.* **11**, 377-379 (1986).

21. K. Sayano, G.A. Rakuljic, and A. Yariv, "Thresholding semilinear phase-conjugate mirror," *Opt. Lett.* **13**, 143-145 (1988).

22. B. Fischer, "Theory of self-frequency detuning of oscillations by wave mixing in photorefractive crystals," *Opt. Lett.* **11**, 236-238 (1986).

23. S. Ducharme and J. Feinberg, "Speed of the photorefractive effect in a $BaTiO_3$ single crystal," *J. Appl. Phys.* **56**, 839-342 (1984).

24. M. Cronin-Golomb and A. Yariv, "Optical limiters using photorefractive nonlinearities," *J. Appl. Phys.* **57**, 4906-4910 (1985).

25. K. Sayano, A. Yariv, and R.R. Neurgaonkar, "Enhanced photorefractive gain in Cr-doped strontium barium niobate with an external dc electric field," *J. Appl. Phys.* **67**, 1594-1596 (1990).

CHAPTER EIGHT

Summary and Future Directions

8.1. Summary and conclusions

The photorefractive properties of new types of materials, potassium tantalate niobate and strontium barium niobate, have been investigated with the goal of improving the magnitude and speed of response of these materials. KTN crystals have been grown with significantly higher ferroelectric to cubic phase transitions, making them available for a larger variety of applications where cooling to cryogenic temperatures was impractical. SBN crystals were studied with new dopant types, temperature control, modification of material parameters, and external fields with the objective of controlling the photorefractive gain and response time.

KTN crystals doped with Cr and Fe were grown and characterized for optical holographic storage applications. Diffraction efficiency and dark decay time measurements were made in a number of crystals that varied in their dopant concentration, Nb/Ta ratio, or Cr/Fe ratio. The Nb concentration was increased to a point where large effects near the phase boundary can be measured at room temperature. The effects of the external bias voltage and temperature on the photorefractive properties were also investigated.

New types of SBN, which were Cr-doped or Rh-doped, were compared to previously grown Ce-doped or Ce,Ca double doped SBN by experimentally measuring their photorefractive gain and response time for two-beam coupling. Large coupling gain but slow response was obtained with the Ce and Rh doping, with corresponding large steady-state index changes but low photorefractive sensitivity

due to their long time constants. Cr-doped SBN:60 and SBN:75 showed much faster response time but with gain coefficients from 1/2 to 1/4 that of Ce-doped SBN. The result was that the photorefractive sensitivity of Cr-doped SBN was on the order of 10^{-3} cm^3/J, which was an order of magnitude better than that of Ce-doped SBN.

Experiments have shown that the photorefractive effect in SBN can be improved through a variety of methods. Heating resulted in modest increases in response speed, but with corresponding loss of gain. Annealing Cr-doped SBN:60 in a furnace resulted in improved gain and temperature stability of the gain. External electric fields also increased gain in Cr-doped SBN:60; similar experiments in Rh-doped SBN resulted in reduction of the response time by more than a factor of 20.

Some applications of photorefractive materials also were demonstrated. These include the self-starting, passive, total internal reflection phase conjugate mirror, thresholding semilinear phase conjugate mirror, a system for one-way image transmission through a distortion, and an electric field controlled and enhanced optical limiter.

8.2. Future directions

Photorefractive materials are currently of interest in a variety of optical storage, optical signal processing, and phase conjugation systems, and especially for future optical computing elements, opto-electronic neural networks, and interconnects. Optics may play a significant role in inputs, storage, and readout for optical computing. However, the slow speed of photorefractive materials poses a significant drawback for many applications.

Modification of as-grown crystals through annealing, oxidation, and reduction

holds potential for tailoring specific samples for fast response or high gain, depending on the particular application. Improvement in optical properties may also result from defect reduction, changes in oxidation states of dopants, and changes in donor and trap energies.

Electric field enhancement of the photorefractive properties has been investigated, but there is a practical limit of the catastrophic depoling point from limitations in the internal fields that can be supported. SBN:75 generated a large effect from a larger electro-optic coefficient even with smaller space charge fields. Other materials with large electro-optic figures of merit may be able to sustain larger photorefractive effects.

The ideal photorefractive material will be one with large gain, fast response, high sensitivity, and high optical quality. No one material currently satisfies all of these conditions, although SBN has been found to satisfy many of these desired properties. There are numerous applications currently awaiting the development of the next generation of materials that can meet these requirements. Other dopants than the ones studied here, and other tungsten bronze materials may possess significant advantages over the figures of merit of the SBN, and further research into these areas is certainly warranted.